Development and Characterization of a Table-Top Laser-Produced Plasma Source for *In-Situ* and Time-Resolved Soft X-Ray Absorption Spectroscopy

Thesis by
Danika Katherine Nimlos

In Partial Fulfillment of the Requirements for the
Degree of
Doctor of Philosophy

CALIFORNIA INSTITUTE OF TECHNOLOGY
Pasadena, California

2025
Defended November 25, 2024

Danika Katherine Nimlos
ORCID: 0000-0002-5414-0039

"Only when it's dark enough can you see the stars."
–Martin Luther King, Jr.

ACKNOWLEDGEMENTS

First and foremost, I would like to extend my deepest gratitude to the professors of my thesis committee, Professors Harry Atwater, Bill Goddard, and Geoff Blake, for their invaluable guidance and feedback throughout my graduate journey. I am especially thankful to my advisor, Professor Scott Cushing, whose unwavering positivity, even in challenging times, has been a source of inspiration. Scott, it has been an absolute pleasure working with you, and your mentorship has been instrumental in shaping both my research and personal growth.

I would also like to extend a thank-you to all the collaborators not on my committee who have provided invaluable samples, calculations, and expertise, in particular Dr. Walter Drisdell and Dr. Amy Cordones-Hahn - your mentorship has been critical to the completion of this work and I am deeply grateful.

A special thank-you goes to the Caltech facilities staff, in particular the CCE facilities manager Joe Drew, for their tremendous support. From responding to lab flooding, cutting through ceilings, drilling into bedrock, and moving thousand-pound optical tables, I can unequivocally say this work would not have been possible without you.

To the wonderful people at the Caltech Y, especially Courtney Reddix and Liz Jackman, you are a shinning light at Caltech. Thank you for your work bringing together the communities of our school and the broader Pasadena area.

I am profoundly appreciative of the entire Cushing Lab, past and present members. A heartfelt thanks to Alejandro Arellano for helping me build the instrument and for his relentless positivity, which made even the toughest days in the sub-basement more manageable. Also a special thanks to Kiara Lewis, who has been a hard working and patient mentee; I am so grateful to have gotten the chance to get to know you over the years. To the XUV subgroup, your insightful discussions and collaboration have been invaluable. A special shout-out to those I spent the COVID-19 pandemic with: Jonathan Michelsen, Bryce Hickam, Isabel Klein, Hanzhe Liu, and Manni He. The friendships we forged during those times were the light in an otherwise dark time. Also thank you to Jocelyn Mendes, for being an exceptional lab mate and an even better friend.

I am deeply thankful for the friendships I've built while at Caltech, specifically with Sadie Dutton, Hamilton Evans, Katie Luedecke, Jake Evans, Holly Barnhart, Anna Overholts, Kshitij Sadasivan, Natalie Hills, John Chapman, Ye-Jin Kim,

Emily De Jong, Max Saccone, and Griffin Mead. From climbing and hiking to camping, skiing, and countless Amigos trips, you've made this journey so much more enjoyable.

To the amazing women I play soccer with, you've kept me sane through it all. Each and every one of you is a huge source of inspiration and I can never thank you enough for reliably providing me with joy every single week.

To the incredible instructors from STEMulate Learning and SKILLZ summer programs, in particular Denise Peoples and Justin Bond, thank you for your inspiring dedication to the children of Pasadena. Working alongside you over the past three summers has been a privilege, and I will cherish every moment of it. The world is a better place with you in it.

To my friends from back home and across the country— Sydney Pimentel, Savannah Wiman, Emma Scher, Jordan Brudos-Nockels, Jake Higgins, Loqman Mohammad, and Michael Curtis—thank you for reminding me that life exists beyond the lab and for your friendship. I appreciate your love and support more than you could possibly know.

To parents and extended family, who have always taught me to be a critical thinker with a big heart, thank you for always being there for me. Thank you to my sister Claire, who has been the ultimate role model since day one. In particular, big thank you to my dog, Harlee, who has no idea what an X-ray is but is always stoked to see me when I get home, making even the worst days bearable.

Finally, to my partner, Dave: your unwavering support, love, and sense of adventure have made this journey so much richer. From our incredible trips and outdoor escapades—thank you for belaying me up big rocks, mobbing on bikes, shredding the gnar (both in its solid and liquid phases), and playing endless games of Catan with me. Through it all, I deeply appreciate you being there with me to take in the beauty of the world.

ABSTRACT

X-ray absorption spectroscopy (XAS) has emerged as an indispensable tool in the fields of carbon capture and conversion, providing element-specific insights into electronic structure, oxidation states, and chemical bonding. Of particular interest are soft X-rays (SXRs), which can probe the X-ray water window, enabling detailed studies of carbon, nitrogen, and transition metal L-edges in aqueous environments. Traditionally, access to this technique and this energy range has been limited to large-scale facilities like synchrotrons and XFELs, which can only serve a small population of users in a given year. Furthermore, more complex techniques such as time-resolved and *in-situ* XAS are practically inaccessible to the majority of users. This thesis explores the development of a table-top laser-produced plasma (LPP) source based on a gaseous target to extend the reach of XAS techniques into laboratory settings. Such sources offer significant advantages in accessibility, flexibility, and cost, while advances in X-ray optics and detection systems have further enhanced their utility. The research presented here focuses on the utilization of gaseous LPP sources for both *in-situ* and time-resolved XAS, pushing the boundaries of table-top soft X-ray absorption capabilities.

Key achievements include exploration of the lower temporal limit of LPP sources for SXR emission, and the first demonstration of liquid-phase XAS measurements using a gaseous LPP source. Gas-phase measurements were also achieved using the system built in this work. Additionally, a novel UV-pump/SXR-probe technique was developed, enabling future time-resolved studies of charge transfer dynamics in transition metal oxides. These advances pave the way for detailed investigations of photodriven processes, interfaces, and catalytic mechanisms critical to carbon capture and conversion. By improving temporal resolution and expanding the scope of *in-situ* XAS techniques, this work addresses fundamental challenges in the field, bringing the power of synchrotron-like spectroscopy into everyday laboratories. Ultimately, the results presented here aim to democratize XAS, fostering a broader adoption of this technique in catalysis and materials research.

PUBLISHED CONTENT AND CONTRIBUTIONS

(1) Nimlos, D.; Arellano, A.; Cushing, S. Approaching the Lower Temporal Limit of Laser-Produced Plasma Sources for Table-Top Soft X-ray NEXAFS Measurements. *ChemPhysChem* **2025**, e202400857.
https://onlinelibrary.wiley.com/doi/abs/10.1002/cphc.202400857
D.K.N. designed and constructed the instrument, collected and analyzed data, and wrote the manuscript.

TABLE OF CONTENTS

LIST OF ILLUSTRATIONS

LIST OF TABLES

NOMENCLATURE

CCD. Charged Coupled Device.

EXAFS. Extended X-ray Absorption Fine Structure.

HHG. High Harmonic Generation.

HXR. Hard X-ray.

LPP. Laser-Produced Plasma.

MOF. Metal Organic Framework.

NEXAFS. Near Edge X-ray Absorption Fine Structure.

SXR. Soft X-ray.

XAFS. X-ray Absorption Fine Structure.

XAS. X-ray Absorption Spectroscopy.

XFEL. X-ray Free Electron Laser.

XUV. Extreme Ultraviolet Radiation.

Chapter 1

INTRODUCTION

In 1895 Germany, William Röntgen discovered a new type of radiation emanating from an induction coil within a vacuum tube [1]. Unsure of what to call the newly discovered radiation, Röntgen referred to it as "X"-rays for brevity. The name stuck and over a hundred years later, X-rays have formed the backbone of understanding many complex systems from biological molecules to solid state materials. X-rays lie in the region of the electromagnetic spectrum between ultraviolet radiation and gamma rays and have wavelengths between 5 nm and 10 pm, with photon energies between 200 eV and 100 keV. Depending on the technique, X-rays have the ability to interrogate the atomic and electronic structure of a material, elucidating the physical basis for observed properties such as thermal and electrical conductivity, chemical reactivity, strength, and magnetism. The utility of X-rays in nearly all areas of research is underscored by the billions of dollars invested by governments around the world to build large-scale user facilities that generate X-ray light for numerous different techniques.

In the fields of carbon capture and conversion, X-ray absorption spectroscopy (XAS) has proven to be a particularly valuable tool. Its ability to access high-energy electronic transitions from core orbitals to unoccupied valence states has made it a powerful analytical tool. For example, it has been used to measure oxidation states, bonding, and structure in solid-state materials for carbon capture [2–5] as well as elucidate the fundamental processes of charge transfer and carrier mobility in photocatalysts [6–11]. XAS is increasingly becoming a necessity in the toolbox of scientists discovering and designing new materials and technologies that will one day be used to capture CO_2 and other pollutants and convert them into value-added fuels and chemicals. However, before XAS measurements can be utilized to their full potential, the limited accessibility to X-ray sources bright enough and broadband enough for spectroscopy creates a bottleneck to progress. More accessible X-ray sources would increase the total number of XAS measurements being conducted, and thus their influence on the carbon capture and conversion field as a whole, but it would also allow more complex, and potentially even higher impact, XAS techniques to be explored as well.

1.1 X-ray Sources for Spectroscopy

For those looking to conduct XAS measurements, there exists two types of X-ray user facilities: synchrotrons and X-ray free electron lasers (XFELs). Synchrotrons accelerate electrons moving at near the speed of light around a cyclical path such that X-rays are emitted tangent to this path and delivered to end stations, or user beamlines, where they can be used for a number of different techniques. XFELS accelerate electrons along one linear path of alternating magnetic fields to create an intense beam of coherent X-rays used by a single technique at any given moment in time. Although these large-scale user facilities have enabled many notable advances in numerous fields of science, access to synchrotrons and XFELs is limited to those who have the resources to submit a competitive beamline proposal, travel to the facility, and stay for a multiple-day period to conduct the experiment. This limited availability also makes it difficult to perform more complex experiments that may require special instrumentation or extensive troubleshooting. As a result, techniques such as *in-situ* X-ray measurements, which measure materials in gas or liquid phase environments, or time-resolved X-ray measurements, which measure the dynamics of a system following an external perturbation as a function of time, are typically only conducted by resident staff scientists.

The challenges and limited access to synchrotron measurements have motivated the growing demand for table-top X-ray sources, which offer greater accessibility and availability. Table-top sources also have the added benefit of being modular and more easily customizable for more complex experimental techniques. Instruments that rely on high harmonic generation (HHG) to generate extreme ultraviolet radiation (XUV, 10-120 eV) can produce high-intensity few femtosecond pulses, and have emerged as powerful tools for time-resolved XUV absorption measurements, measuring electron and hole dynamics [9, 12], or structural dynamics such as polaron formation in photoelectrocatalysts [8, 13]. Although they have made significant discoveries in the XUV regime, spectrometers based on HHG have not demonstrated absorption measurements in the soft X-ray regime. In addition, they are extremely complex and costly instruments to build, maintain, and operate. Laser-produced-plasma (LPP) sources have been demonstrated for their ability to generate radiation in a wider spectral range, from XUV [14, 15] to the soft X-ray (SXR, 120-1,200 eV) [16, 17] and hard X-ray (HXR, >1.2 keV) [18, 19] regimes, depending on the target and driving laser. Many LPP spectrometers are based on highly ubiquitous and relatively inexpensive Nd:YAG laser systems and have fairly simple optical setups. The trade-offs for LPP spectrometers are longer pulse duration and lower brilliance,

as compared to HHG spectrometers. The comparison of the X-ray table-top sources and user facilities is given in Table 1.1.

Source	Photon Energy	Brilliance	Pulse Duration	Instrumental Limitations
Synchrotron	10 eV - 100 keV[20]	10^{13}-10^{16} photons/s[21]	100 fs (time sliced)[22]	limited availability
Free-electron laser	<25 keV[23]	Up to 10^{33} photons/s[24]	1-100 fs[22]	single user, limited availability
High-harmonic generation	10-450 eV[25,26]	10^{8}-10^{12} photons/s[27,28]	43 as[29]	expensive, complex
Laser-produced plasma				
Gaseous target	200 - 1,000 eV[30]	10^{9} photons/s[16,31]	>23 ps[32]	low flux, high instability
Liquid target	2-20 keV[33,34]	10^{6}-10^{8} photons/s[33,35]	>70 fs[36]	low flux, debris
Solid target	50 eV - 57 keV[19]	10^{9} photons/s[18]	>100 fs[18]	low flux, debris

Table 1.1: Overview of available X-ray sources, their reported capabilities, and the limitations for each.

LPP sources have been used for a number of different techniques, including lithography [37, 38], microscopy [39, 40], and steady state and time-resolved diffraction [41–44] and absorption measurements [45–48]. From an instrumentation perspective, gaseous targets for LPP sources are the simplest because the lower density target results in a lower degree of debris produced during the plasma generation process. Ablation of the solid and liquid targets when irradiated with a high power laser beam results in sputtering of surrounding optics and components in the instrument [49, 50].

In particular, LPP sources based on gaseous targets have been gaining attention for their ability to take high quality synchrotron-like XAS measurements in the soft X-ray range, with successful applications in studying environmental organic samples [51], transition metal oxides [17], and polymers [52]. With improvements in X-ray gratings and focusing optics [15, 39, 40], X-ray detection [53–55], and gaseous targets in vacuum [30, 56, 57], these sources have the potential to extend

the accessibility of this technique, as well as allow more complex techniques such as time-resolved measurements and *in-situ* measurements.

1.2 Soft X-ray Absorption Spectroscopy

Generally, the probability that a photon is absorbed by a given material is determined by the available quantum states. Linear absorption of a photon is more likely to occur if the energy of that photon matches the energy difference between two quantum states that exist within the material. This forms the basis for many linear spectroscopic techniques, which allow spectroscopists to measure the states of a system by studying its interaction with different frequencies of light. Visible and infrared spectroscopies, for example, measure the structure of valence states and vibrational levels, as their respective energies match the energy gaps between these states. X-ray absorption spectroscopy can access the high-energy transitions from core orbitals to unoccupied valence states. Although core orbitals are generally shielded from the surrounding chemical environment, valence states are not. This means that X-ray accessible transitions, or edges, are element specific and can be sensitive to variations in both local and valence energy.

Within the X-ray regime, the XUV, SXR, and HXR regions can access increasingly higher-energy edges. Figure 1.1 illustrates how X-ray nomenclature is determined on the principle quantum number n of the initial state absorbing the photon, and how edges from each regime are sometimes present in multi-electron atoms. Although photons from each region can provide element-specific information, they are each best suited for different types of analysis. For example, the XUV, which has wavelengths between 10 - 100 nm, is well suited to probe dynamics of free carriers, electrons, and holes in photoexcited materials, as the wavelength overlaps with these wavefunctions well. The SXR and HXR regions can access higher energy transitions, making them more sensitive to changes in local electronic structure due to oxidation state, hybridization, and bond length. In practice, by virtue of the larger number of available transitions in the XUV and SXR regions, these photons have a high degree of absorption in all materials, necessitating that the absorption measurements must be conducted in vacuum environments. Hard X-rays have much longer attenuation lengths, in contrast, and absorbance measurements in this range can be conducted under ambient conditions.

Despite the requirement of vacuum environments, soft X-rays offer distinct advantages over XUV and HXR spectroscopy. First, soft X-rays can access the X-ray

water window, the region of the soft X-ray regime below the oxygen K-edge (532 eV). In this range, photons have a higher transmission through water, enabling *in-situ* measurements of materials in aqueous environments. This is particularly true for organic molecules, whose carbon and nitrogen atoms have K-edges in this region. In fact, because carbon, nitrogen, and oxygen do not have core orbitals beyond the K-shell (1s), their core states are only accessible by soft X-ray photons.

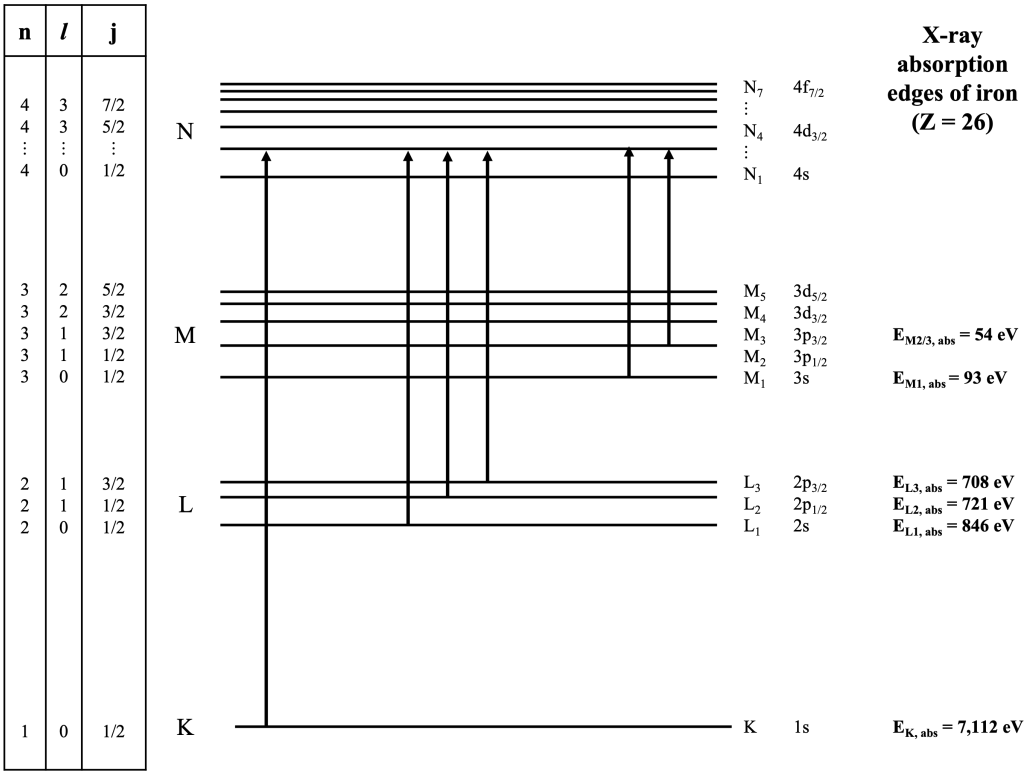

Figure 1.1: Energy level diagram for an iron atom, as an illustration of the transitions accessible by photons in the X-ray regime. Depicted are transitions from the K-shell (n = 1), L-shell (n = 2), and M-shell (n = 3), which in the case of iron are accessible by HXR, SXR, and XUV photons, respectively.

In the analysis of the SXR absorption spectrum, the two regions of interest are the near edge X-ray absorption fine structure (NEXAFS) and the extended X-ray absorption fine structure (EXAFS) region, as illustrated in Figure 1.2. Together, these two regions compose what is referred to as X-ray absorption fine structure (XAFS). NEXAFS, within ~50 eV of the X-ray absorption edge, can be used to measure the oxidation state, hybridization, and structure of the valence and conduction bands. *In-situ* NEXAFS has been instrumental in studying catalyst systems. For example, changes in oxidation state, measured by changes to peak energy at an element's absorption edge, have elucidated the changing oxide composition on Cu catalysts

[58], the reduction of cationic Au to electrocatalytic metallic Au during 2-propanol oxidation [59], and corrosion species in complex alloys [60]. In addition, changes to the edge-step height (shown as $\Delta\mu$in Figure 1.2) at a given element's absorption edge scale with how much of that element is present. Changes in the height of the edge-step have been used to indicate the detachment of particles from metallic catalysts [61, 62].

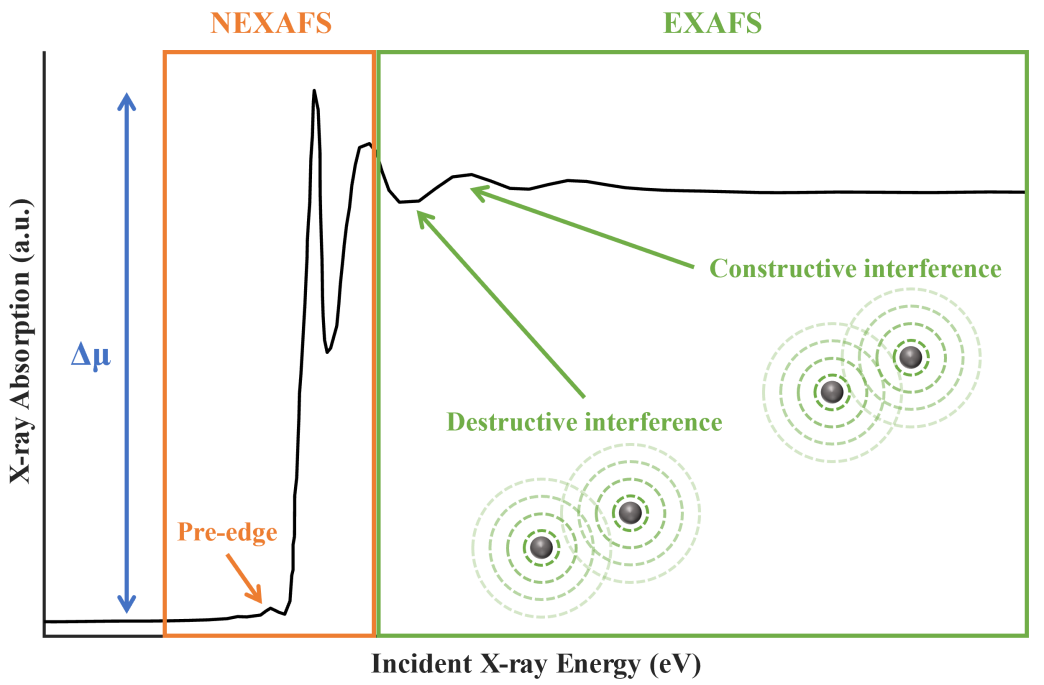

Figure 1.2: X-ray absorption fine structure (XAFS), composed of both the X-ray near-edge structure (NEXAFS) and the extended X-ray absorption fine structure (EXAFS). NEXAFS is most sensative to local electronic structure such as oxidation state and hybridization. The constructive and destructive interference pattern due to backscattered photoelectrons interfering with nearby oscillating electric fields can be fourier transformed to provide bond length information in the EXAFS region of the spectrum.

EXAFS, 50-1000 eV above the absorption edge, consists of oscillations due to constructive and destructive interference of an outgoing photoelectron with those refracted off neighboring atoms (Figure 1.2). The oscillations in this region of the X-ray absorption spectrum can be Fourier transformed to give bond lengths of nearest neighbors, which can be used to indicate oxide layer formation, faceting, and particle migration. *In-situ* EXAFS has been used to measure the phase evolution of iron oxides under different reaction conditions [63], alloying of Cu with Zn in

bimetallic catalysts during electrocatalysis [64], and the removal of lattice oxygen in an IrO_2 catalyst during the oxygen evolution reaction [65].

With respect to the photocatalysts used for CO_2 reduction, two implementations of X-ray absorption measurements in the soft X-ray regime are particularly powerful: *in-situ* measurements and time-resolved or transient measurements. *In-situ* X-ray absorption measurements have allowed the elucidation of oxide formation, particle corrosion, and interfacial dynamics in working electrochemical systems and metal-organic frameworks for carbon capture [61, 66–68]. Most of these discoveries, however, have been conducted using hard X-rays because of their longer attenuation lengths in matter and consequently ability to conduct hard X-ray absorption measurements in ambient conditions. *In-situ* soft X-ray absorption measurements are far rarer, due to the necessity of vacuum environments. Although more logistically challenging, *in-situ* SXR absorption measurements have the potential to measure intermediates in the catalytic reactions of greenhouse gases due to their ability to access the X-ray water window and the K-edges of C, N, and O. Time-resolved X-ray absorption measurements have been used to measure carrier dynamics, charge transfer, and reaction intermediates in electrochemical systems [69–71]. As mentioned above, SXRs are particularly sensitive to oxidation state, hybridization, and bond length. These characteristics could be tracked following the generation of a charge carrier in a photocatalyst to better understand charge transfer, diffusion, and product formation. Additionally, reaction intermediates could be measured and tracked similar to the *in-situ* measurements.

1.3 Thesis Overview

Although significant discoveries have been made at large-scale user facilities, there remains an opportunity to advance table-top X-ray spectrometers based on LPP generation to more complex techniques that compete with the capabilities of synchrotrons. Recent advances to X-ray optics and detectors, as well as plasma targets, make this a particularly opportune time to accomplish this goal. The work described in this thesis presents an effort to advance this technology to the more complex techniques of *in-situ* and time-resolved XAS in the soft X-ray regime on the table-top.

Chapter 2 provides a description of the LPP spectrometer's key specifications, fundamental principles of operation, and presents work on exploring the lower temporal limit of X-ray pulses from plasmas generated in gaseous plasmas. Chapter

3 details the *in-situ* X-ray techniques employed at synchrotron facilities, how they have been translated to LPP sources, and the first liquid- and gas-phase measurements of CO_2, ambient air, and liquid water, measured with the LPP source described in Chapter 2. Chapter 4 describes the efforts to measure the photoexcited response of TiO_2 thin films using UV-pump/SXR-probe transient absorption spectroscopy and the future steps to fully realize this technique with the existing system. Together, these techniques are explored within the context of broadening the applicability of soft X-ray absorption measurements to better understand the key processes that determine the ultimate device efficacy of carbon capture and conversion systems.

References

(1) Röntgen, W. *Nature* **1896**, *53*, 274–276.

(2) Bordiga, S.; Bonino, F.; Petter Lillerud, K.; Lamberti, C. *Chemical Society Reviews* **2010**, *39*, 4885–4927.

(3) Le Toquin, R.; Paulus, W.; Cousson, A.; Prestipino, C.; Lamberti, C. *Journal of the American Chemical Society* **2006**, *128*, 13161–13174.

(4) Valenzano, L.; Civalleri, B.; Chavan, S.; Bordiga, S.; Nilsen, M. H.; Jakobsen, S.; Lillerud, K. P.; Lamberti, C. *Chemistry of Materials* **2011**, *23*, 1700–1718.

(5) Lamberti, C.; van Bokhoven, J. A. In *X-Ray Absorption and X-Ray Emission Spectroscopy*; John Wiley & Sons, Ltd: 2016, pp 351–383.

(6) Timoshenko, J.; Roldan Cuenya, B. *Chemical Reviews* **2021**, *121*, 882–961.

(7) Yoon, W.-S.; Balasubramanian, M.; Chung, K. Y.; Yang, X.-Q.; McBreen, J.; Grey, C. P.; Fischer, D. A. *Journal of the American Chemical Society* **2005**, *127*, 17479–17487.

(8) Carneiro, L. M.; Cushing, S. K.; Liu, C.; Su, Y.; Yang, P.; Alivisatos, A. P.; Leone, S. R. *Nature Materials* **2017**, *16*, 819–825.

(9) Liu, H.; Michelsen, J. M.; Mendes, J. L.; Klein, I. M.; Bauers, S. R.; Evans, J. M.; Zakutayev, A.; Cushing, S. K. *The Journal of Physical Chemistry Letters* **2023**, *14*, 2106–2111.

(10) Jiang, C.-M.; Baker, L. R.; Lucas, J. M.; Vura-Weis, J.; Alivisatos, A. P.; Leone, S. R. *The Journal of Physical Chemistry C* **2014**, *118*, 22774–22784.

(11) Su, X.; Wang, Y.; Zhou, J.; Gu, S.; Li, J.; Zhang, S. *Journal of the American Chemical Society* **2018**, *140*, 11286–11292.

(12) Cushing, S. K.; Porter, I. J.; de Roulet, B. R.; Lee, A.; Marsh, B. M.; Szoke, S.; Vaida, M. E.; Leone, S. R. *Science Advances* **2020**, *6*, eaay6650.

(13) Kim, Y.-J.; Mendes, J. L.; Michelsen, J. M.; Shin, H. J.; Lee, N.; Choi, Y. J.; Cushing, S. K. *Science Advances* **2024**, *10*, 4282.

(14) Bayer, A.; Barkusky, F.; Döring, Stefan; Großmann, P.; Mann, K. *X-Ray Optics and Instrumentation* **2010**, *2010*, 1–9.

(15) Mann, K.; Holburg, J.; Lange, S.; Müller, M.; Schäfer, B. In *Extreme Ultraviolet (EUV) Lithography X*, Extreme Ultraviolet (EUV) Lithography X, SPIE: 2019; Vol. 10957, pp 305–310.

(16) Müller, M.; Kühl, F.-C.; Großmann, P.; Vrba, P.; Mann, K. *Optics Express* **2013**, *21*, 12831.

(17) Fok, T.; Wachulak, P. W.; Janulewicz, K. A.; Węgrzyński, Ł.; Bartnik, A.; Szlachetko, J.; Zając, M.; Fiedorowicz, H. *Journal of Instrumentation* **2020**, *15*, C05026–C05026.

(18) Weisshaupt, J.; Juvé, V.; Holtz, M.; Ku, S.; Woerner, M.; Elsaesser, T.; Ališauskas, S.; Pugžlys, A.; Baltuška, A. *Nature Photonics* **2014**, *8*, 927–930.

(19) Schnürer, M.; Nickles, P. V.; Kalachnikov, M. P.; Sandner, W.; Nolte, R.; Ambrosi, P.; Miquel, J. L.; Dulieu, A.; Jolas, A. *Journal of Applied Physics* **1996**, *80*, 5604–5609.

(20) Energie, H.-Z. B. f. M. und BESSY II Light Source HZB Website, `https://www-intern.helmholtz-berlin.de/forschung/quellen/bessy/index_en.html` (accessed 11/12/2024).

(21) Willmott, P., *An Introduction to Synchrotron Radiation: Techniques and Applications*; John Wiley & Sons: 2019; 501 pp.

(22) Stepanov, A. G.; Hauri, C. P. *Journal of Synchrotron Radiation* **2016**, *23*, 141–151.

(23) Huang, N.; Deng, H.; Liu, B.; Wang, D.; Zhao, Z. *The Innovation* **2021**, *2*, 100097.

(24) Altarelli, M.; Brinkmann, R.; Chergui, M. **2007**.

(25) Pertot, Y.; Schmidt, C.; Matthews, M.; Chauvet, A.; Huppert, M.; Svoboda, V.; von Conta, A.; Tehlar, A.; Baykusheva, D.; Wolf, J.-P.; Wörner, H. J. *Science* **2017**, *355*, 264–267.

(26) Attar, A. R.; Bhattacherjee, A.; Pemmaraju, C. D.; Schnorr, K.; Closser, K. D.; Prendergast, D.; Leone, S. R. *Science* **2017**, *356*, 54–59.

(27) Labaye, F.; Gaponenko, M.; Modsching, N.; Brochard, P.; Paradis, C.; Schilt, S.; Wittwer, V. J.; Südmeyer, T. *IEEE Journal of Selected Topics in Quantum Electronics* **2019**, *25*, 1–19.

(28) Rothhardt, J.; Hädrich, S.; Demmler, S.; Krebs, M.; Winters, D. F. A.; Kühl, T.; Stöhlker, T.; Limpert, J.; Tünnermann, A. *Physica Scripta* **2015**, *2015*, 014030.

(29) Gaumnitz, T.; Jain, A.; Pertot, Y.; Huppert, M.; Jordan, I.; Ardana-Lamas, F.; Wörner, H. J. *Optics Express* **2017**, *25*, 27506–27518.

(30) Wachulak, P.; Fok, T.; Węgrzyński, Ł.; Bartnik, A.; Nyga, P.; Janulewicz, K.; Fiedorowicz, H. *Optics Express* **2021**, *29*, 20514.

(31) Vrba, P.; Vrbová, M.; Brůža, P.; Pánek, D.; Krejčí, F.; Kroupa, M.; Jakůbek, J. *Journal of Physics: Conference Series* **2012**, *370*, 012049.

(32) Nimlos, D.; Arellano, A.; Cushing, S. *ChemPhysChem* **2025**, *n/a*, e202400857.

(33) Miaja-Avila, L.; O'Neil, G. C.; Uhlig, J.; Cromer, C. L.; Dowell, M. L.; Jimenez, R.; Hoover, A. S.; Silverman, K. L.; Ullom, J. N. *Structural Dynamics* **2015**, *2*, 024301.

(34) Tompkins, R. J.; Mercer, I. P.; Fettweis, M.; Barnett, C. J.; Klug, D. R.; Porter, L. G.; Clark, I.; Jackson, S.; Matousek, P.; Parker, A. W.; Towrie, M. *Review of Scientific Instruments* **1998**, *69*, 3113–3117.

(35) Korn, G.; Thoss, A.; Stiel, H.; Vogt, U.; Richardson, M.; Elsaesser, T.; Faubel, M. *Optics Letters* **2002**, *27*, 866–868.

(36) Wieland, M.; Faubel, M.; Schmidt, M.; Vogt, U.; Wilhein, T. In *Applications of X Rays Generated from Lasers and Other Bright Sources II*, Applications of X Rays Generated from Lasers and Other Bright Sources II, SPIE: 2001; Vol. 4504, pp 62–68.

(37) Purvis, M. et al. In *Extreme Ultraviolet (EUV) Lithography IX*, Extreme Ultraviolet (EUV) Lithography IX, SPIE: 2018; Vol. 10583, pp 476–485.

(38) Bakshi, V., *EUV Sources for Lithography*; SPIE Press: 2006; 1104 pp.

(39) Müller, M.; Mey, T.; Niemeyer, J.; Mann, K. *Optics Express* **2014**, *22*, 23489.

(40) Wachulak, P. W.; Torrisi, A.; Bartnik, A.; Węgrzyński, Ł.; Fok, T.; Fiedorowicz, H. *Applied Physics B* **2017**, *123*, 25.

(41) Sokolowski-Tinten, K.; Blome, C.; Blums, J.; Cavalleri, A.; Dietrich, C.; Tarasevitch, A.; Uschmann, I.; Förster, E.; Kammler, M.; Horn-von-Hoegen, M.; von der Linde, D. *Nature* **2003**, *422*, 287–289.

(42) Juvé, V.; Holtz, M.; Zamponi, F.; Woerner, M.; Elsaesser, T.; Borgschulte, A. *Physical Review Letters* **2013**, *111*, 217401.

(43) Quevedo, W.; Peth, C.; Busse, G.; Scholz, M.; Mann, K.; Techert, S. *International Journal of Molecular Sciences* **2009**, *10*, 4754–4771.

(44) Pudell, J.; Maznev, A. A.; Herzog, M.; Kronseder, M.; Back, C. H.; Malinowski, G.; von Reppert, A.; Bargheer, M. *Nature Communications* **2018**, *9*, 3335.

(45) Dorchies, F.; Lévy, A.; Goyon, C.; Combis, P.; Descamps, D.; Fourment, C.; Harmand, M.; Hulin, S.; Leguay, P. M.; Petit, S.; Peyrusse, O.; Santos, J. J. *Physical Review Letters* **2011**, *107*, 245006.

(46) Mantouvalou, I.; Witte, K.; Martyanov, W.; Jonas, A.; Grötzsch, D.; Streeck, C.; Löchel, H.; Rudolph, I.; Erko, A.; Stiel, H.; Kanngießer, B. *Applied Physics Letters* **2016**, *108*, 201106.

(47) Anwar, M. I.; Iqbal, M.; Hwang, B. J.; Faiyaz, M.; Mun, B. S.; Janulewicz, K. A.; Noh, D. Y. *Optics Express* **2019**, *27*, 6030–6036.

(48) Jonas, A.; Dammer, K.; Stiel, H.; Kanngiesser, B.; Sánchez-de-Armas, R.; Mantouvalou, I. *Analytical Chemistry* **2020**, *92*, 15611–15615.

(49) Brandstätter, M.; Gambino, N.; Abhari, R. S. *Journal of Applied Physics* **2018**, *123*, 043308.

(50) Rollinger, B.; Abhari, R. S. *Physics of Fluids* **2016**, *28*, 074105.

(51) Sedlmair, J.; Gleber, S.-C.; Peth, C.; Mann, K.; Niemeyer, J.; Thieme, J. *Journal of Soils and Sediments* **2012**, *12*, 24–34.

(52) Müller, M.; Schellhorn, M.; Mann, K. *Journal of Analytical Atomic Spectrometry* **2019**, *34*, 1779–1785.

(53) Iniewski, K. (, *Advanced X-ray Detector Technologies: Design and Applications*; Springer Nature: 2022; 297 pp.

(54) Nagarkar, V. V.; Shestakova, I.; Gaysinskiy, V.; Singh, B.; Miller, B. W.; Bradford Barber, H. *Nuclear Instruments and Methods in Physics Research Section A: Accelerators, Spectrometers, Detectors and Associated Equipment* **2006**, *563*, 45–48.

(55) Soman, M. R.; Hall, D. J.; Tutt, J. H.; Murray, N. J.; Holland, A. D.; Schmitt, T.; Raabe, J.; Schmitt, B. *Journal of Instrumentation* **2013**, *8*, C01046.

(56) Holburg, J.; Müller, M.; Mann, K. *Optics Express* **2021**, *29*, 6620.

(57) Wachulak, P. W.; Torrisi, A.; Bartnik, A.; Adjei, D.; Kostecki, J.; Wegrzynski, L.; Jarocki, R.; Szczurek, M.; Fiedorowicz, H. *Applied Physics B* **2015**, *118*, 573–578.

(58) Lee, S. H.; Lin, J. C.; Farmand, M.; Landers, A. T.; Feaster, J. T.; Avilés Acosta, J. E.; Beeman, J. W.; Ye, Y.; Yano, J.; Mehta, A.; Davis, R. C.; Jaramillo, T. F.; Hahn, C.; Drisdell, W. S. *Journal of the American Chemical Society* **2021**, *143*, 588–592.

(59) Choi, Y.; Sinev, I.; Mistry, H.; Zegkinoglou, I.; Roldan Cuenya, B. *ACS Catalysis* **2016**, *6*, 3396–3403.

(60) Cakir, C. T.; Piotrowiak, T.; Reinholz, U.; Ludwig, A.; Emmerling, F.; Streli, C.; Guilherme Buzanich, A.; Radtke, M. *Analytical Chemistry* **2023**, *95*, 4810–4818.

(61) Drisdell, W.; Lee, S. H.; Acosta, J. A.; Lee, D.; Larson, D.; Li, H.; Chen, J.; Blair, S.; Gallo, A.; Zheng, H.; Tassone, C.; Jaramillo, T. Structural Transformation and Degradation of Cu Nanocatalysts during Electrochemical CO2 Reduction Reaction `https://www.researchsquare.com/article/rs-3204416/v1` (accessed 08/20/2024), pre-published.

(62) Pasquini, C. et al. *Analytical and Bioanalytical Chemistry* **2021**, *413*, 5395–5408.

(63) Monnier, J.; Réguer, S.; Foy, E.; Testemale, D.; Mirambet, F.; Saheb, M.; Dillmann, P.; Guillot, I. *Corrosion Science* **2014**, *78*, 293–303.

(64) Jeon, H. S.; Timoshenko, J.; Scholten, F.; Sinev, I.; Herzog, A.; Haase, F. T.; Roldan Cuenya, B. *Journal of the American Chemical Society* **2019**, *141*, 19879–19887.

(65) Czioska, S.; Boubnov, A.; Escalera-López, D.; Geppert, J.; Zagalskaya, A.; Röse, P.; Saraçi, E.; Alexandrov, V.; Krewer, U.; Cherevko, S.; Grunwaldt, J.-D. *ACS Catalysis* **2021**, *11*, 10043–10057.

(66) Dutta, A.; Rahaman, M.; Hecker, B.; Drnec, J.; Kiran, K.; Zelocualtecatl Montiel, I.; Jochen Weber, D.; Zanetti, A.; Cedeño López, A.; Martens, I.; Broekmann, P.; Oezaslan, M. *Journal of Catalysis* **2020**, *389*, 592–603.

(67) Cheng, W.; Su, H.; Liu, Q. *Accounts of Chemical Research* **2022**, *55*, 1949–1959.

(68) Tofoni, A.; Tavani, F.; Braglia, L.; Colombo, V.; Torelli, P.; D'Angelo, P. *Radiation Physics and Chemistry* **2023**, *213*, 111243.

(69) Cushing, S. K.; Carneiro, L. M.; Zuerch, M.; Chang, H.-T.; Leone, S. R. *ECS Meeting Abstracts* **2017**, *MA2017-02*, 1876.

(70) Baran, T.; Fracchia, M.; Vertova, A.; Achilli, E.; Naldoni, A.; Malara, F.; Rossi, G.; Rondinini, S.; Ghigna, P.; Minguzzi, A.; D'Acapito, F. *Electrochimica Acta* **2016**, *207*, 16–21.

(71) Saes, M.; Bressler, C.; Abela, R.; Grolimund, D.; Johnson, S. L.; Heimann, P. A.; Chergui, M. *Physical Review Letters* **2003**, *90*, 047403.

Chapter 2

APPROACHING THE LOWER LIMIT OF PULSE DURATION FOR LASER-PRODUCED PLASMA SOURCES

Most of this chapter has been reproduced with permission from:

(1) Nimlos, D.; Arellano, A.; Cushing, S. *ChemPhysChem* **2025**, *n/a*, e202400857.

2.1 Abstract

The increasing popularity of time-resolved X-ray absorption measurements for understanding dynamics in molecular and material systems has led to many advances in table-top sources for pulsed X-rays. We report on a table top laser-produced plasma (LPP) source that can perform soft X-ray (SXR), near edge X-ray absorption fine structure (NEXAFS) measurements using a laser source with 23 ps pulse duration. The spectrometer's key specifications, such as brilliance, resolution, and stability, are characterized against the more commonly used longer-pulse-duration LPP sources. The 23 ps laser produced approximately an order of magnitude weaker SXR flux than the 8 ns laser for a higher power density due to the smaller total energy absorbed by the plasma. The increased repetition rate, as well as the use of a high line-density X-grating, and a self-referencing scheme still allowed for NEXAFS measurements of Si_3N_4 and TiO_2 thin films with 2.5 minute acquisition times, a resolving power of $E/\Delta E = 424$, and a signal-to-noise ratio of 100. It was observed that degradation of the gas jet nozzle led to long-term instability of the source, which can be remediated using alternative nozzle designs. This work demonstrates the feasibility of achieving higher temporal resolution in future time-resolved X-ray absorption measurements using table-top LPP sources.

2.2 Introduction

X-ray absorption spectroscopy (XAS) is an invaluable tool in material and chemical sciences, used for a wide range of applications from photocatalysis to solid-state batteries [1–4]. X-rays excite element-specific core-level transitions, with the near-edge X-ray absorption fine structure (NEXAFS) providing information on oxidation state, coordination, hybridization, and bonding [5]. NEXAFS measurements are predominantly conducted at large-scale user facilities such as synchrotrons or free electron lasers because they require tunable, high-photon-energy sources. While

advances in table-top sources for X-ray measurements have made them an increasingly viable alternative, reported setups still face limitations in the trade-off between energy range, flux, and temporal resolution.

The increasing demand for XAS measurements underscores the need for continued advances in table-top approaches, particularly for time-resolved studies. High harmonic generation (HHG) and laser-produced plasma (LPP) generation are the most common methods explored for table-top X-ray sources. HHG is used to generate coherent X-rays through a three-step process of ionization and recombination [6]. HHG sources can generate extreme ultraviolet radiation below 300 eV with photon fluxes up to 10^{13} photons/s [7], and are commonly used for transient absorption measurements with temporal resolutions of attoseconds and spectral resolutions on the order of tens to hundreds of meV [8–10]. While HHG sources have proven to be powerful instruments, they require high power fs laser systems and complex specialty laboratories to extend their energy range past the extreme ultraviolet regime. LPP sources generate incoherent soft or hard X-rays by ionization of a gas, liquid, or solid target [11–15]. Gaseous LPPs have been the most studied because they produce minimal debris, utilize the widely available and cost-effective Nd:YAG laser system, and generate broadband radiation in the soft X-ray (SXR) regime, striking a balance between cost, brilliance, energy range, and feasibility. Gas-based LPPs have been reported to generate SXRs between 250 eV and 1 keV, with photon fluxes up to 10^{14} photons/s/sr [16], and spectral resolutions on the order of hundreds of meV [17]. However, the temporal resolution of gaseous LPP sources has been typically limited to nanoseconds or in some cases hundreds of picoseconds [16, 18]. Improving the temporal resolution of LPP sources could enable the measurement of faster dynamics, such as carrier recombination [19], polaron formation [20], or charge transfer [21].

This work explores the lower limits of pulse duration in an LPP for use as a tabletop SXR spectrometer. LPPs in gaseous targets have not been generated using laser pulses below a 170 ps pulse width. In this study, we report SXR emission from an LPP source generated with 23 ps pulses. We benchmark our source against an 8 ns Nd:YAG, commonly used in LPP setups [22–24]. Although per-pulse-flux of the ps source is nearly an order of magnitude less than that of the ns source, the increased laser repetition rate and a self-referencing scheme still allow high-resolution NEXAFS spectra with measurement times of 2.5 minutes, a resolving power of $E/\Delta E = 424$, and a signal-to-noise ratio (SNR) of 100. This is demonstrated

with Si_3N_4 and TiO_2 thin films. The findings of this paper are important for pushing table-top SXR spectroscopy into the tens of picoseconds regime, which is critical for measuring liquid-phase and solid-state dynamics. Furthermore, the use of an Nd:YAG laser and electronic delay lines can extend measurement timescales from the nanosecond to second regime in future transient measurements. This approach offers a more space and cost-effective alternative to most HHG based setups.

2.3 Background

In order to generate a plasma consisting of free electrons and positively charged ions, the ionization potential of a given target I_p must be overcome. This can be achieved by the absorption of a photon with energy greater than that of the ionization potential of the target such that $\hbar\omega > I_p$, however the ionization potentials of most atoms are >20 eV [25]. Lower photon energies can be used to ionize targets using high power lasers whose field strengths are comparable to the Coulombic attraction between electrons and protons in a given target [26]. In this regime, many nonlinear ionization processes can take place and the dominant mechanism can be identified by the Keldysh parameter γ, given by Equation 2.1,

$$\gamma = \sqrt{\frac{I_p}{2U_p}} \tag{2.1}$$

where U_p describes the ponderomotitve energy, or the average kinetic energy of a free electron oscillating in a laser field, and can be calculated by Equation 2.2,

$$U_p = \frac{e^2\epsilon_0^2}{4m_e\omega_0^2} = \frac{I_0 e^2 \lambda_0^2}{8\pi^2 m_e \epsilon_0 c^3} = 9.337 \times 10^{-20} I_0 \lambda_0^2 \frac{\text{eV}}{\text{W cm}^{-2}\,\text{nm}^2} \tag{2.2}$$

where m_e and e are the mass and charge of an electron, respectively, ϵ_0 is the permittivity of free space, c is the speed of light, and ω_0, I_0, and λ_0 are the central frequency, intensity, and wavelength of the laser [27]. Using the parameters of the Nd:YAG laser used in this study, and most LPP SXR spectrometers based on gaseous targets, it can be shown that for most atomic targets, $\gamma < 1$ [26]. In this regime, tunnel ionization is the dominant mechanism, wherein the external electric field of the laser contorts the potential energy surface of the target such that bound electrons can quantum tunnel through energy barriers to free themselves of the atom. In the other regime, where $\gamma > 1$, the dominant ionization mechanism is multiphoton

ionization, in which multiple photons of lower energy are absorbed to overcome the potential barrier and free an electron from a parent atom.

Once the plasma has been generated, the oscillations in electron density due to the competing forces of ionized electrons accelerating away from nuclei and the Coulombic attraction with positive nuclei are described by the electron plasma frequency, ω_p [28], given in Equation 2.3:

$$\omega_p \equiv \left(\frac{e^2 n_e}{\epsilon_0 m_e}\right)^{1/2} \tag{2.3}$$

where n_e is the electron density of the target. Given this definition, and rewriting Maxwell's equations, one can derive the following dispersion relation:

$$\omega^2 = \omega_p^2 + k^2 c^2 \tag{2.4}$$

which describes the dispersion of external waves, with frequency ω, propagating in a plasma [25, 29]. The frequency for which $\omega = \omega_p$ is defined as the *critical frequency* and the corresponding electron density is defined as the *critical electron density*. If the plasma frequency is larger than that of the incident electromagnetic field, the plasma is characterized as *overdense* and incoming radiation will be shielded out, or reflected. If the plasma frequency is smaller than that of the incoming radiation, the plasma is characterized as *underdense*, and the laser field can propagate in the plasma. For a plasma generated in a gaseous target, the typical electron densities lie between n_e = 10^{18}-10^{19} e^-/cm^3 [16, 30–32]. For the 1064 nm fundamental beams of Nd:YAGs, the most commonly used for these sources, the critical electron density is 9.86×10^{20} electrons/cm^3. Therefore, the plasma generated in LPP SXR spectrometers are defined as underdense. In the underdense limit, collective effects become important if $\omega_p \tau_{int} > 1$, where τ_{int} describes the interaction time of the plasma with the laser (the duration of the laser pulse, in this case) [25, 33]. Collective effects include heating of the plasma by the incoming electromagnetic field, accelerating relativistic electrons in the plasma, transferring energy to the electron by a process known as *inverse bremsstrahlung*, from the German word for "braking radiation". The plasma is also heated by the propagating electric field, causing electrons to undergo collisional heating by electron-ion collisions.

The energy transferred to the plasma is converted to X-rays by two dominant processes. First, collisions of high-kinetic-energy electrons with bound electrons result

in fluorescent *characteristic line emission*, where electrons in higher-lying orbitals radiatively decay to fill the vacancies created by ejected electrons at discrete energies. Second, electrons with high kinetic energy are deflected by positively charged nuclei at a wide variety of distances, resulting in continuum X-ray emission in a process known as *bremsstrahlung*, the radiative version of *inverse bremsstrahlung* mentioned before [34]. The Fourier transform of the time-dependent electron acceleration in the plasma is what results in the continuum spectrum from bremsstrahlung deflections.

The lower limit of pulse duration of the SXR pulse can be constrained by the thermalization time of free electrons in the plasma. Using the root mean square thermal electron velocity v_e, determined by the electron temperature T_e, the thermal expansion time t_D can be related to the electron plasma frequency by Equation 2.5:

$$t_D \approx \frac{\lambda_D}{v_e} = \left(\frac{\epsilon_0 k_B T_e}{e^2 n_e} \cdot \frac{m_e}{k_B T_e} \right)^{\frac{1}{2}} = \omega_p^{-1} \tag{2.5}$$

where λ_D is the Debye length, which measures the length of a charge's electrostatic effect. Using average electron densities of LPPs in gaseous targets, the expansion time is on the order of tens of femtoseconds [25]. For effective bremsstrahlung emission of X-rays, and therefore a usable X-ray continuum for measurement, the driving laser pulse must have a duration longer than the thermal expansion time of the electrons [28].

When considering LPP spectrometers for spectroscopy, one looks to balance three key characteristics: broadband emission for effective XAS measurements, maximum X-ray flux for shorter acquisition times, and higher signal-to-noise ratio, and, in the case of time-resolved measurements, pulse duration. Broadband emission can be achieved by the selection of gas, in this case Kr as it is most broadband and dominated by bremsstrahlung radiation. Note that spectra from low atomic number (Z) gases, such as N_2, O_2, SF_6, and Ne, consist mostly of sharp peaks corresponding to the characteristic line emission of those atomic nuclei. These sources tend to serve techniques such as diffraction and microscopy better, as they require a monochromatic source. Higher atomic number gases such as Ar, Kr and Xe are quasi-continuous, due to the larger number of electronic transitions coming from multiply ionized atoms (characteristic line emission) and the stronger electric field due to more positively charged nucleus (bremsstrahlung radiation) [16, 28, 31, 35]. A comparison of the emission spectra from laser produced plasmas in various gasses

is given in Figure 2.1. To maximize X-ray emission from a LPP in a gaseous target, both the driving laser pulse energy and the pulse duration must be considered. A shorter pulse duration results in more efficient absorption of energy by the gaseous plasma, likely due to the rapid adiabatic expansion of gas in vacuum [16, 36, 37], but the interaction time must be sufficient for the maximum amount of energy to be transferred from the laser pulse to heat the plasma. Thus the total energy absorbed by the plasma will result in higher electron temperature and increased X-ray emission.

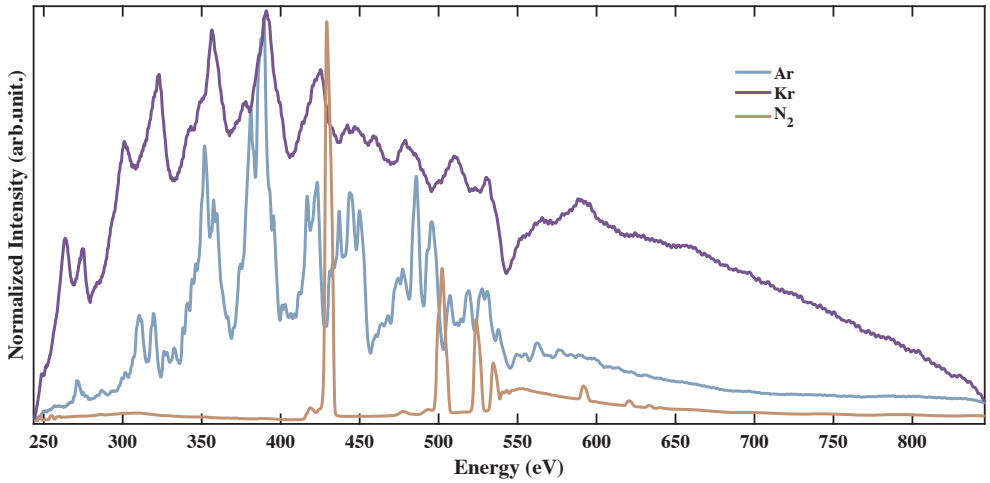

Figure 2.1: Comparison of the SXR emission spectra from laser produced plasmas generated in Ar, Kr, and N_2 gases.

2.4 Experimental Section

Figure 2.2 is a photograph and schematic diagram of the table-top SXR spectrometer. The spectrometer is built in three cubic vacuum chambers, each with a side length of 23 cm, that can be evacuated to base pressures of 10^{-5} Torr. The plasma generation is driven by the 1064 nm fundamental beam of an Nd:YAG laser, either an EKSPLA PL2251B-20 (20 Hz repetition rate, 23 ps FWHM pulse duration, 80 mJ pulse energy) or a Spectra-Physics Quanta-Ray PRO (10 Hz repetition rate, 8 ns FWHM pulse duration, 800 mJ pulse energy). The 1064 nm beam from the Nd:YAG laser is focused with a 150 mm focal length lens onto a gas jet inside the vacuum chamber. Due to the losses by the mirrors, lens, window, and other optical elements in the beam path, the pulse energy of the ns laser at the gas jet is 640 mJ/pulse, giving a power density of 2.98×10^{11} W/cm^2. The pulse energy of the ps laser is 67 mJ/pulse at the gas jet, with a power density of 3.42×10^{13} W/cm^2.

Focal spot size was experimentally measured using a knife edge scan in which the

intensity of the laser beam at the focus was measured as a function of a knife edge's position in the beam. The energies of the ps laser were measured with a thermopile sensor (Newport 919P-050-26), and those of the ns laser were measured with a Scientech 37-2002 power meter with a 380101 (400-1200 nm) detector head. Using a previously documented procedure [38], the intensity as a function of position was differentiated to give the beam profile, which was then used to calculate the beam full width at half maximum (FWHM). The energies of each laser source were measured before (E_{in}) and after (E_{out}) the gas jet to calculate the amount of energy absorbed by the plasma and coupling efficiency at each input energy.

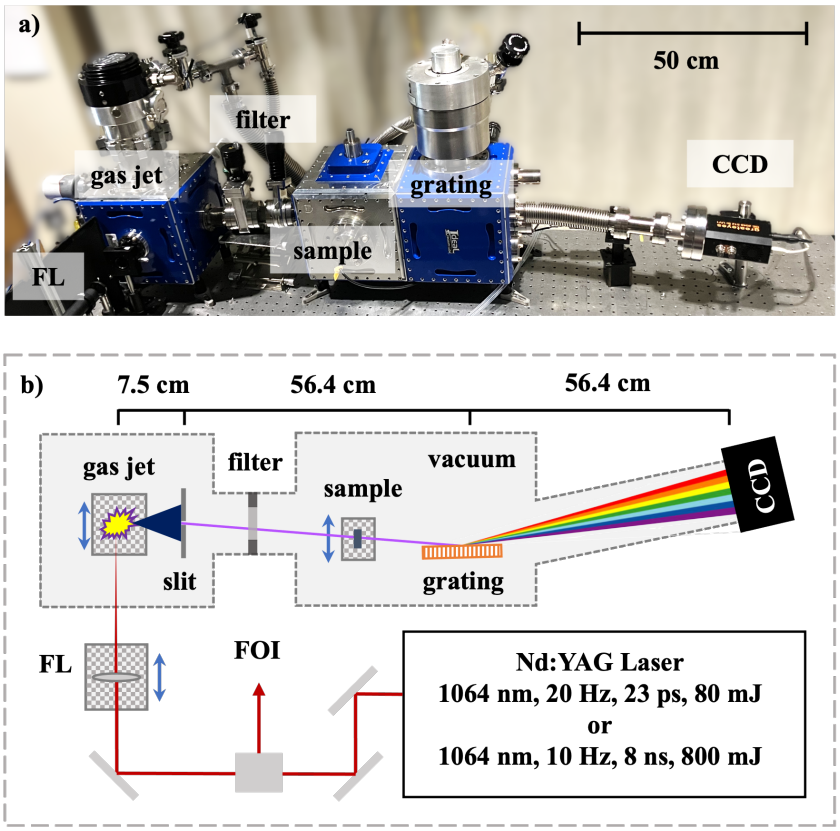

Figure 2.2: a) Instrument photograph and b) schematic of the table-top soft X-ray spectrometer with the Nd:YAG laser beam path passing through a faraday optical isolator (FOI), where any backscatter reflected off the plasma is rejected, before passing through a focusing lens (FL) where it is focused onto a pulsed gas jet inside a vacuum chamber. Generated X-rays emitted 90° to the incoming laser are then measured by the SXR spectrometer.

Ar, Kr, or N_2 gas with a backing pressure of 175 psi is delivered by a high-speed pulsed solenoid valve (Parker 009-0347-900) using a stainless-steel nozzle with a 0.02" diameter opening. The gas jet is electronically delayed from the main pulse

generator in the Nd:YAG laser. The solenoid delivers gas pulses with a duration of t_{open} = 350 µs or 900 µs for the ps and ns lasers, respectively. A filter gate valve (VAT, 01032-CE01-AAV2) separates the plasma generation chamber from the rest of the setup to optimize vacuum pressures and minimize debris from the plasma generation process. During operation of the gas jet, the plasma generation chamber is held at 10^{-3} Torr and the rest of the setup remains at 10^{-5} Torr.

The X-rays emitted from the plasma pass through either a 50 or 100 µm slit and a 100 nm Al filter enclosed in the filter gate valve, which blocks any out-of-band emission and scattered 1064 nm light from the plasma. Soft X-rays interact with the sample in transmission geometry before being diffracted by an aberration-corrected concave grating (3,600 grooves per mm, 564 mm focal length, Shimadzu, L3600-1-6) and measured by a charged coupled device (CCD, Greateyes, GE 2048 512 BI UV1, 13.5 × 13.5 µm pixel size, 512 × 2048 pixels) . The grating used in this study was previously shown to take high resolution, E/ΔE = 1500, NEXAFS spectra [17]. For the spectral comparisons of the ns and ps lasers, the CCD was operated at room temperature. Visible images of the plasma were taken using a CMOS (Complementary Metal Oxide Semiconductor) sensor (Zelux, CS165CU, Thorlabs) at a distance of approximately 150 mm and averaging over ~1 minute integration time. It should be noted that the pulse duration of the SXR pulse was not measured directly due to the temporal resolution of available X-ray photodiodes; however, it is constrained to be no shorter than 23 ps.

Energy calibration is performed by creating a calibration curve using the Ar IX emission lines at photon energies of E = 254.4 eV and 252.1 eV (with wavelengths of λ = 4.873 nm and 4.918 nm, respectively) and the N VI emission lines at photon energies of E = 430.8 eV, 498.1 eV, 521.6 eV, and 538.6 eV (with wavelengths of λ = 2.878 nm, 2.489 nm, 2.377 nm, and 2.302 nm, respectively) as documented in the NIST atomic spectra database [39]. The pixel positions for each of these energies were then fit to a quadratic polynomial. After calibration, energy resolution was experimentally measured by fitting the N VI emission line at 430.8 eV to a single-term Gaussian function, such that,

$$f(x) = a_1 \times e^{-\left(\frac{x-b_1}{c_1}\right)^2} \tag{2.6}$$

where the coefficient c_1 can be used to calculate the FWHM by,

$$FWHM = 2\sqrt{\ln 2}\, c_1 \tag{2.7}$$

For the NEXAFS measurements, Kr gas was used due to its quasi-continuous emission spectrum and a 100 µm slit was used to reduce measurement times. The CCD was cooled to -50 °C to reduce background noise, and dark counts were subtracted from all spectra. A self-referencing scheme, demonstrated previously [40], utilizes the 4π emission from the plasma to measure SXR transmission of the sample and a reference simultaneously. A schematic of the self-referencing scheme and representative data at the Ti $L_{2,3}$ edge is given in Figure 2.3. Self-referencing was employed to reduce the effects of shot-to-shot noise and long-term instabilities of the plasma source. Absorption (Abs) was calculated from the transmitted intensity through the sample (I) and reference (I_0) using Equation 3.1,

$$A = -\ln\left(\frac{I}{I_0}\right) \tag{2.8}$$

The TiO_2 thin film sample was prepared by atomic layer deposition (ALD) on 50 nm thick diamond membranes with 2 mm diameter apertures. Silicon nitride (Si_3N_4) membranes were obtained commercially (Norcada Inc., NX10300A). Full experimental details of the thin film preparation process are given in Appendix A.

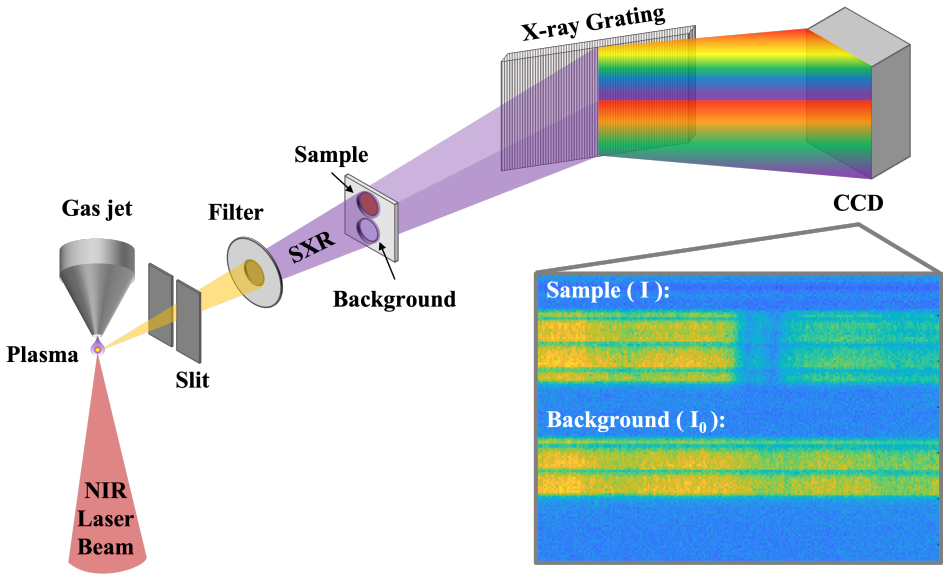

Figure 2.3: Self-referencing scheme which utilizes the 4π emission of the plasma to image the transmission from the sample and a reference simultaneously. The example data pictured is the raw CCD image of the Ti $L_{2,3}$ absorption edge measured from the amorphous TiO_2 thin films.

2.5 Results and Discussion

Nanosecond vs. Picosecond X-ray Emission

Figure 2.4 compares the Ar emission spectra of plasmas generated with 8 ns and 23 ps lasers. Spectra were collected over 1 s integration times (20 and 10 pulses for the ps and ns lasers, respectively) using a 50 µm slit. When integrated over all energies, the ns laser has 4.6 times greater total flux per integration period, which is 9.2 times greater flux per pulse. This difference could be explained by the total absorbed energies of the plasmas for the two laser sources. For the spectra in Figure 2.4, the energies absorbed by the plasma are 60 mJ and 235 mJ for the ps and ns lasers, respectively.

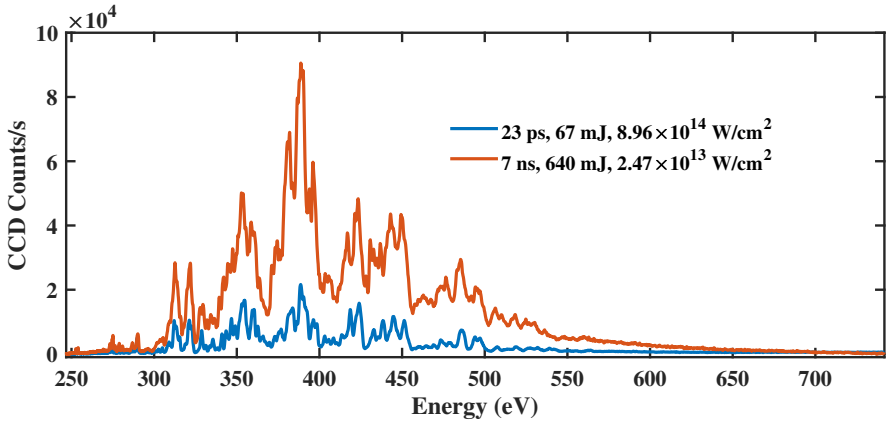

Figure 2.4: Comparison of Ar emission spectra for the ns and ps lasers, accumulated over 1 s integration time (20 pulses for the ps laser and 10 pulses for the ns laser).

The coupling efficiency, defined as the fraction of the laser energy absorbed by the plasma, is compared for both the ps and ns sources in Figure 2.5. The ps source is coupled into the gaseous target at higher efficiencies, even at much lower input energies. This improved coupling efficiency has been observed in previous studies [16], which reported similar trends when comparing plasmas in gaseous targets generated with 7 ns and 170 ps lasers. Full tabulated data is given in Appendix A.

Additionally, earlier work documented an increase in overall flux and a blue shift in the spectra from plasmas generated with ps lasers when the absorbed energy exceeded 200 mJ [16]. In this study, there does not appear to be a spectral shift towards higher energies with the ps plasma as it absorbs less energy. Comparison of the Ar emission spectra measured using the ps and ns sources here to those reported previously show a similar flux for our 23 ps source compared to the much higher pulse energy 170 ps source (Figure 2.6). This suggests that the over 8-fold increase

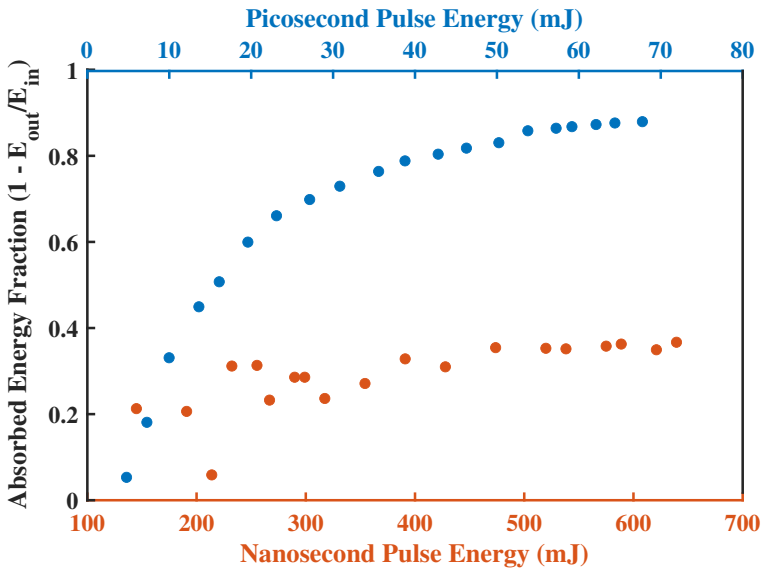

Figure 2.5: Coupling efficiencies for the ns and ps sources for plasmas generated in Ar gas at varying input energies. Pulse energies were measured before the plasma (E_{in}) and after the plasma (E_{out}) to calculate the absorbed energy fraction of the plasma.

in power density is compensated by the ~1/4 reduction in absorbed energy of the 23 ps source here compared to the 170 ps source in the resulting X-ray emission spectrum. It should be noted that the authors in this previous work used a 100 μm slit and 200 nm Al filter [16] (compared to the 50 μm slit and 100 nm Al filter used here).

Alternatively, the increased energy density at the focal point of the ps laser could be resulting in a more strongly ionized plasma, but reabsorption by the surrounding gas plume could attenuate the signal that makes it to the detector. This is supported by the observation that the X-ray emission from the ps plasma drops off sharply when the pulse duration of the gas jet is increased beyond 550 μs. This suggests a strong degree of reabsorption of emitted X-rays by the surrounding gas plume. Previous reports have shown that ps sources produce smaller plasmas [16, 41], suggesting that the smaller size of the plasma could also play a role in the reabsorption of X-rays. A tungsten nozzle with a smaller diameter orifice that does not rapidly degrade in the plasma could address this issue and increase flux. Previous work on the gas delivery system has reported higher stability and increased X-ray flux [32, 42–44].

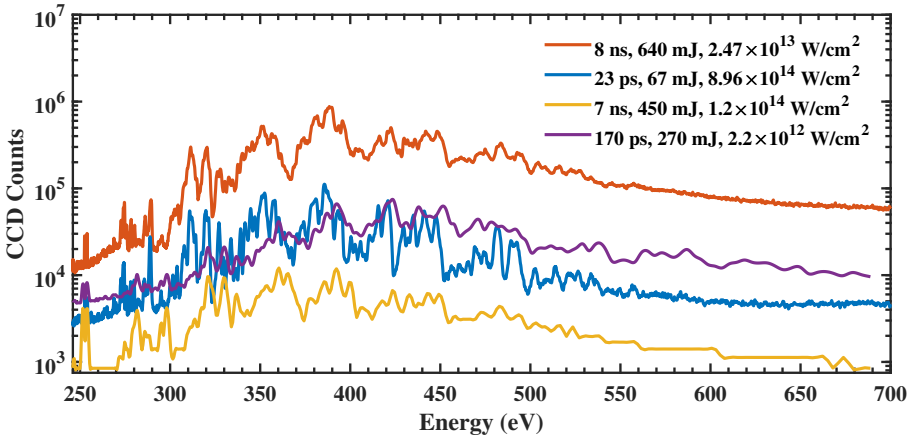

Figure 2.6: Comparison of the Ar emission spectra using the 8 ns and 23 ps sources presented in this study (red and blue, respectively) and the 170 ps and 7 ns sources presented in previous work (purple and yellow, respectively) [16]. Data is presented as a sum over 100 pulses.

Spectrometer Resolution and Sensitivity

To quantify the spectral resolution of the instrument using the ps laser, the N_2 emission spectrum was collected with a 50 µm slit. The N^{5+} emission peak at 430.8 eV from the N_2 plasma emission spectrum was fit to a Gaussian with a FWHM of 1.02 eV, which gives a resolving power of E/ΔE = 424. The results of this fitting and the N_2 emission spectrum from the ps plasma integrated for 1 s are given in Figure 2.7. For comparison, high-resolution XAS measurements at synchrotron can achieve resolving powers up to tens of thousands [45]. The photon flux of the N^{5+} emission peak at 430.8 eV from the N_2 plasma emission was measured to be 3.7 × 10^7 photons/s/cm^2.

LPP sources have been shown to have high pulse-to-pulse instabilities and non-uniformity [14, 15]. In the sources developed in this work, long-term degradation of the gas jet nozzle is observed due to the plasma generation process. In Figure 2.8, this degradation can be seen directly in loss of flux within the first few minutes of measurement. Over the course of 15 minutes (18,000 SXR pulses) intensity drops by 2.41% with a standard deviation over the mean of 1.02%. This measurement shows that, despite the nozzle degradation, the instrument has a SNR on the order of 100. For comparison, high-precision synchrotron measurements report SNRs on the order of 1000 [46].

This is further evidenced by the relative size and intensities of the plasmas generated

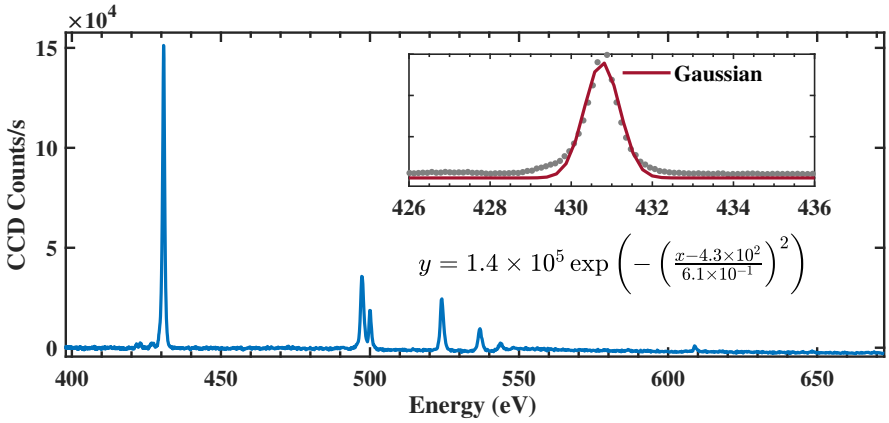

Figure 2.7: N_2 emission spectrum from ps SXR source and gaussian fit to the N^{5+} emission peak at 430.8 eV (λ = 2.878 nm).

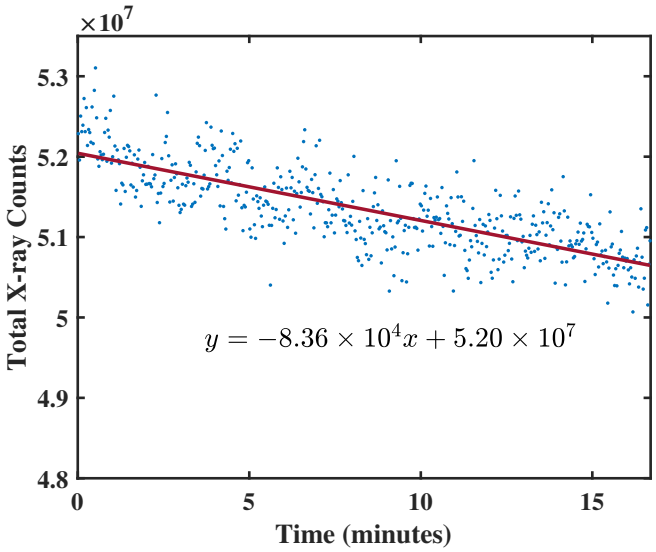

Figure 2.8: Total integrated X-ray intensity from a Kr plasma where each data point is 40 summed SXR shots as a function of time, fit to a linear regression.

in Ar, Kr, and N_2, as illustrated in Figure 2.9, which compares the visible emission of plasmas generated in each gas.

NEXAFS Spectra

To quantify the system's key specifications for measuring X-ray absorption data, the absorption spectra were measured for a commercially available 50 nm thick Si_3N_4 membrane and an as-deposited 40 nm TiO_2 thin film, prepared by ALD. For the NEXAFS spectrum of Si_3N_4 and as-deposited TiO_2, a 100 µm slit is used. Figure 2.10 shows the raw transmission and smoothed absorption spectra from the

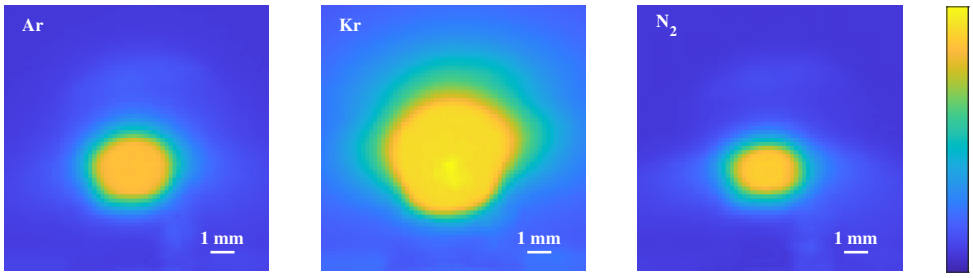

Figure 2.9: Visible image of the plasmas generated in Ar, Kr, and N_2 gases.

as-deposited TiO_2 thin film at the Ti $L_{2,3}$-edges and the O K-edge, compared to as-deposited TiO2 absorption spectra taken at a synchrotron. Figure 2.11 shows the raw transmission and smoothed N K-edge absorption spectra of a 50 nm Si_3N_4 membrane taken with the LPP spectrometer presented here, as compared to those taken with an earlier reported LPP spectrometer. All spectra were accumulated over 3,000 SXR pulses, to give a total measurement time of 2.5 minutes, similar to or shorter than total acquisition times reported by similar LPP sources [17, 23, 48]. Raw data of the O K-edge using different integration times and comparing averaging methods is detailed in Appendix A.

The X-ray absorption spectra of the as-deposited TiO_2 thin film show decent agreement when compared to synchrotron data. The reference synchrotron data in Figure 2.10 were taken of an as-deposited TiO_2 thin film deposited by sputtering with oxygen partial pressure of 0.04. At the Ti $L_{2,3}$-edges, the instrument can resolve two transitions at 462 eV (L_2) and 456 eV (L_3), which arise from the splitting of the 2p orbitals of the Ti atom due to spin-orbit coupling. However, the as-deposited TiO_2 film does not exhibit the distinct crystal field splitting of the 3d orbitals in octahedral crystalline complexes observed in the XAS spectra of the anatase and rutile phases of TiO_2 [47]. Shoulder structures are present at the Ti L_2- and L_3-edges, and subtle splitting appears near the prominent peak near 532 eV in the O K-edge spectra, but these are less pronounced compared to crystalline phases. This minimal splitting could be explained by the amorphous nature of as-deposited TiO_2, the limited resolution of the spectrometer, or some combination of the two.

Compared to the Ti $L_2, 3$-edge, the O K-edge spectrum is noisier and shows less agreement with the synchrotron data, likely due to a lower signal-to-noise ratio in this region of the Kr emission spectrum, as shown in the raw transmission data

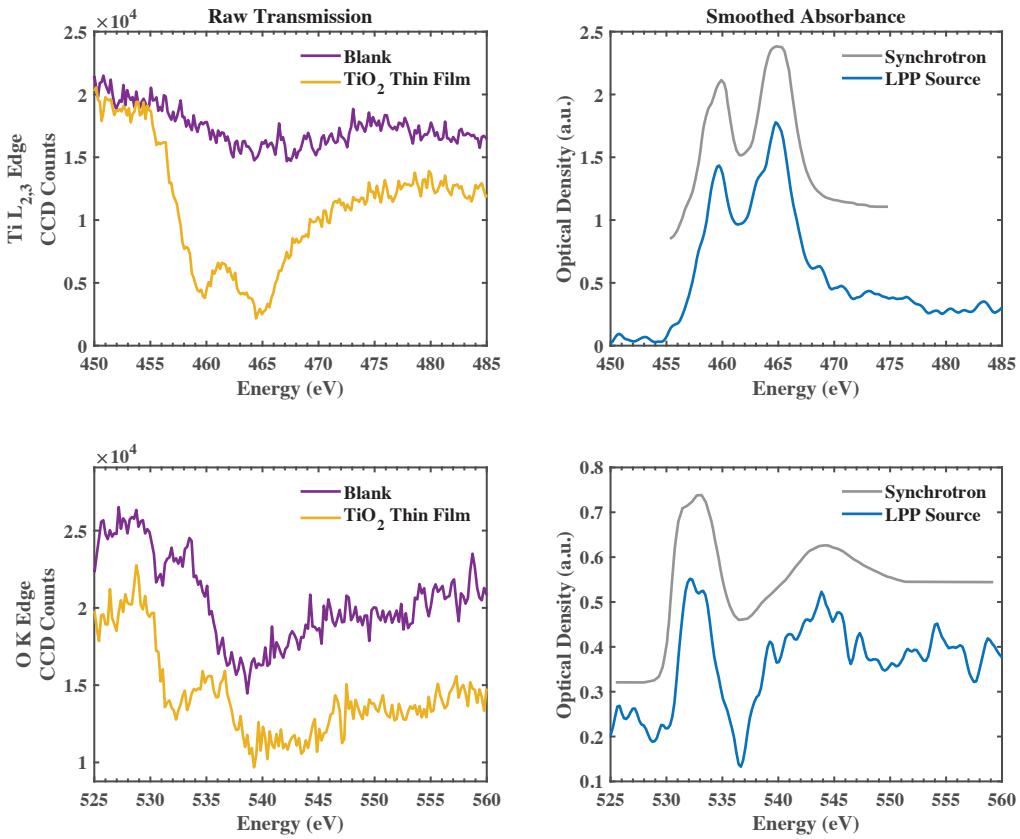

Figure 2.10: X-ray absorption spectra of the 40 nm TiO_2 thin film using the ps LPP source. In the left-hand column, the raw transmission spectra of both the blank diamond membrane (purple trace, I_0) and the diamond membrane with the as-deposited TiO_2 thin film (yellow trace, I) is presented. In the right-hand column, the smoothed absorbance spectra acquired with the LPP source (blue trace) are compared to synchrotron spectra (grey trace). The data collected at the Ti $L_{2,3}$-edge is presented in the first row while that of the O K-edge is presented in the second. The synchrotron data presented here were scaled and shifted along the y-axis for comparison. Synchrotron data are from ref [47] of an as-deposited, amorphous TiO_2 thin film deposited by sputtering with 0.04 partial pressure of oxygen.

in Figure 2.10. The N K-edge spectrum of the Si_3N_4 thin film in Figure 2.11 is compared to a previously reported LPP source, and is less noisy, benefiting from the higher signal-to-noise ratio of the Kr emission in that energy range.

2.6 Conclusion

The key characteristics of X-ray emission from a LPP source with a 23 ps driving laser were explored and benchmarked against an 8 ns system. A comparison with a much higher pulse energy ns source and similar sources in previously published

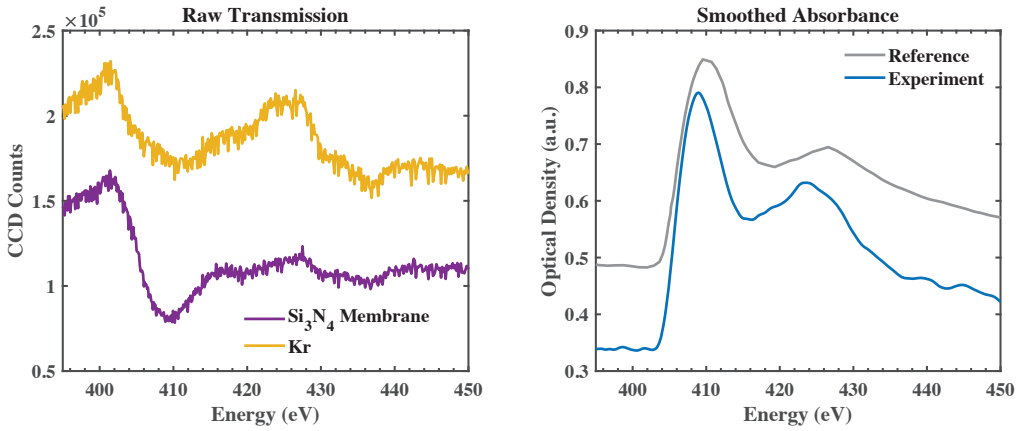

Figure 2.11: X-ray absorption spectra of the Si_3N_4 membranes using the ps LPP source. On the left is the raw transmission through the 50 nm Si_3N_4 membrane (purple trace, I) and the Kr emission spectrum (yellow trace, I_0). On the right is the absorption spectrum of the 50 nm Si_3N_4 membrane collected with the ps LPP source (blue trace) compared to that of a 75 nm Si_3N_4 membrane from a LPP source in ref [23] (grey trace). Reference data was shifted along the y-axis for comparison.

reports shows the effect of shorter pulse duration and pulse energy on resulting X-ray spectra. The shorter pulses and resulting order of magnitude higher energy density at the target are not found to compensate for the lower total absorbed energy by the plasma in the resulting X-ray spectrum. However, the higher repetition rate still allows for the collection of similar NEXAFS spectra to other systems over similar measurement times. Furthermore, an X-ray grating with 3600 l/mm line density allowed for E/ΔE = 424 resolution. Although the stability of the X-ray emission is not high enough to collect long-term averages for time-resolved measurements due to gas jet nozzle degradation, improvements to the gas delivery system can be made to improve long-term stability [32, 42, 43, 49].

The advancements demonstrated here, along with extensive prior work accomplished in this field, position the LPP source as a promising tool for more complex X-ray absorption techniques, such as time-resolved and *in-situ* measurements. Specifically, time-resolved X-ray absorption measurements with picosecond resolution could elucidate dynamics in photocatalysts such as carrier dynamics, hole-polaron formation, product formation, and corrosion mechanisms.

References

(1) Zoric, M. R.; Basera, P.; Palmer, L. D.; Aitbekova, A.; Powers-Riggs, N.; Lim, H.; Hu, W.; Garcia-Esparza, A. T.; Sarker, H.; Abild-Pedersen, F.; Atwater,

H. A.; Cushing, S. K.; Bajdich, M.; Cordones, A. A. *ACS Nano* **2024**, *18*, 19538–19548.

(2) Bokarev, S. I.; Khan, M.; Abdel-Latif, M. K.; Xiao, J.; Hilal, R.; Aziz, S. G.; Aziz, E. F.; Kühn, O. *The Journal of Physical Chemistry C* **2015**, *119*, 19192–19200.

(3) Lapteva, L. L.; Fedoseeva, Yu. V.; Shlyakhova, E. V.; Makarova, A. A.; Bulusheva, L. G.; Okotrub, A. V. *Journal of Materials Science* **2019**, *54*, 11168–11178.

(4) Swallow, J. E. N.; Fraser, M. W.; Kneusels, N.-J. H.; Charlton, J. F.; Sole, C. G.; Phelan, C. M. E.; Björklund, E.; Bencok, P.; Escudero, C.; Pérez-Dieste, V.; Grey, C. P.; Nicholls, R. J.; Weatherup, R. S. *Nature Communications* **2022**, *13*, 6070.

(5) Stöhr, J., *NEXAFS Spectroscopy*; Springer Science & Business Media: 2013; 415 pp.

(6) Lewenstein, M.; Balcou, Ph.; Ivanov, M. Yu.; L'Huillier, A.; Corkum, P. B. *Physical Review A* **1994**, *49*, 2117–2132.

(7) Rothhardt, J.; Hädrich, S.; Demmler, S.; Krebs, M.; Winters, D. F. A.; Kühl, T.; Stöhlker, T.; Limpert, J.; Tünnermann, A. *Physica Scripta* **2015**, *2015*, 014030.

(8) Zürch, M.; Chang, H.-T.; Borja, L. J.; Kraus, P. M.; Cushing, S. K.; Gandman, A.; Kaplan, C. J.; Oh, M. H.; Prell, J. S.; Prendergast, D.; Pemmaraju, C. D.; Neumark, D. M.; Leone, S. R. *Nature Communications* **2017**, *8*, 15734.

(9) Cushing, S. K.; Porter, I. J.; de Roulet, B. R.; Lee, A.; Marsh, B. M.; Szoke, S.; Vaida, M. E.; Leone, S. R. *Science Advances* **2020**, *6*, eaay6650.

(10) Liu, H.; Michelsen, J. M.; Mendes, J. L.; Klein, I. M.; Bauers, S. R.; Evans, J. M.; Zakutayev, A.; Cushing, S. K. *The Journal of Physical Chemistry Letters* **2023**, *14*, 2106–2111.

(11) Mantouvalou, I.; Jonas, A.; Witte, K.; Jung, R.; Stiel, H.; Kanngießer, B. In *X-Ray Lasers and Coherent X-ray Sources: Development and Applications*, X-Ray Lasers and Coherent X-ray Sources: Development and Applications, SPIE: 2017; Vol. 10243, pp 15–22.

(12) Peth, C.; Kalinin, A.; Barkusky, F.; Mann, K.; Toennies, J. P.; Rusin, L. Y. *Review of Scientific Instruments* **2007**, *78*, 103509.

(13) Hansson, B. A. M.; Hemberg, O.; Hertz, H. M.; Berglund, M.; Choi, H.-J.; Jacobsson, B.; Janin, E.; Mosesson, S.; Rymell, L.; Thoresen, J.; Wilner, M. *Review of Scientific Instruments* **2004**, *75*, 2122–2129.

(14) Vrba, P.; Vrbová, M.; Brůža, P.; Pánek, D.; Krejčí, F.; Kroupa, M.; Jakůbek, J. *Journal of Physics: Conference Series* **2012**, *370*, 012049.

(15) Bayer, A.; Barkusky, F.; Döring, Stefan; Großmann, P.; Mann, K. *X-Ray Optics and Instrumentation* **2010**, *2010*, 1–9.

(16) Müller, M.; Kühl, F.-C.; Großmann, P.; Vrba, P.; Mann, K. *Optics Express* **2013**, *21*, 12831.

(17) Holburg, J.; Müller, M.; Mann, K.; Wild, P.; Eusterhues, K.; Thieme, J. *Analytical Chemistry* **2022**, *94*, 3510–3516.

(18) Grossmann, P.; Rajkovic, I.; Moré, R.; Norpoth, J.; Techert, S.; Jooss, C.; Mann, K. *Review of Scientific Instruments* **2012**, *83*, 053110.

(19) Qian, R.; Zong, H.; Schneider, J.; Zhou, G.; Zhao, T.; Li, Y.; Yang, J.; Bahnemann, D. W.; Pan, J. H. *Catalysis Today* **2019**, *335*, 78–90.

(20) Carneiro, L. M.; Cushing, S. K.; Liu, C.; Su, Y.; Yang, P.; Alivisatos, A. P.; Leone, S. R. *Nature Materials* **2017**, *16*, 819–825.

(21) Zhang, L.; Mohamed, H. H.; Dillert, R.; Bahnemann, D. *Journal of Photochemistry and Photobiology C: Photochemistry Reviews* **2012**, *13*, 263–276.

(22) Fok, T.; Wachulak, P.; Węgrzyński, Ł.; Bartnik, A.; Nowak, M.; Nyga, P.; Kostecki, J.; Nasiłowska, B.; Skrzeczanowski, W.; Pietruszka, R.; Janulewicz, K.; Fiedorowicz, H. *Materials* **2021**, *14*, 7337.

(23) Wachulak, P.; Duda, M.; Bartnik, A.; Węgrzyński, Ł.; Fok, T.; Fiedorowicz, H. *APL Photonics* **2019**, *4*, 030807.

(24) Mann, K.; Holburg, J.; Lange, S.; Müller, M.; Schäfer, B. In *Extreme Ultraviolet (EUV) Lithography X*, Extreme Ultraviolet (EUV) Lithography X, SPIE: 2019; Vol. 10957, pp 305–310.

(25) Attwood, D., *Soft X-Rays and Extreme Ultraviolet Radiation: Principles and Applications*, 1st ed.; Cambridge University Press: 1999.

(26) *Strong Field Laser Physics*; Brabec, T., Ed.; Springer Series in Optical Sciences, Vol. 134; Springer New York: New York, NY, 2009.

(27) Keldysh, L. V. *SOVIET PHYSICS JETP* **1965**, *20*, 1307–1314.

(28) Colombant, D.; Tonon, G. F. *Journal of Applied Physics* **1973**, *44*, 3524–3537.

(29) Chen, F. F., *Introduction to Plasma Physics and Controlled Fusion*; Springer International Publishing: Cham, 2016.

(30) Rakowski, R.; Bartnik, A.; Fiedorowicz, H.; de Gaufridy de Dortan, F.; Jarocki, R.; Kostecki, J.; Mikołajczyk, J.; Ryć, L.; Szczurek, M.; Wachulak, P. *Applied Physics B* **2010**, *101*, 773–789.

(31) Fiedorowicz, H.; Bartnik, A.; Szczurek, M.; Daido, H.; Sakaya, N.; Kmetik, V.; Kato, Y.; Suzuki, M.; Matsumura, M.; Tajima, J.; Nakayama, T.; Wilhein, T. *Optics Communications* **1999**, *163*, 103–114.

(32) Holburg, J.; Müller, M.; Mann, K. *Optics Express* **2021**, *29*, 6620.

(33) Murnane, M. M.; Kapteyn, H. C.; Rosen, M. D.; Falcone, R. W. *Science* **1991**, *251*, 531–536.

(34) Als-Nielsen, J.; McMorrow, D., *Elements of Modern X-ray Physics*, 1st ed.; Wiley: 2011.

(35) Giulietti, D.; Gizzi, L. A. *La Rivista del Nuovo Cimento (1978-1999)* **1998**, *21*, 1–93.

(36) Hagena, O. F. *Surface Science* **1981**, *106*, 101–116.

(37) Ditmire, T.; Smith, R. A.; Marjoribanks, R. S.; Kulcsár, G.; Hutchinson, M. H. R. *Applied Physics Letters* **1997**, *71*, 166–168.

(38) Khosrofian, J. M.; Garetz, B. A. *Applied Optics* **1983**, *22*, 3406–3410.

(39) Kramida, A.; Ralchenko, Y. NIST Atomic Spectra Database, NIST Standard Reference Database 78, National Institute of Standards and Technology: 1999.

(40) Wachulak, P.; Duda, M.; Bartnik, A.; Sarzyński, A.; Węgrzyński, Ł.; Nowak, M.; Jancarek, A.; Fiedorowicz, H. *Optics Express* **2018**, *26*, 8260.

(41) Vrba, P.; Vrbova, M.; Zakharov, S. V.; Zakharov, V. S. *Physics of Plasmas* **2014**, *21*, 073301.

(42) Holburg, J.; Müller, M.; Mann, K.; Wieneke, S. *Journal of Vacuum Science & Technology A: Vacuum, Surfaces, and Films* **2019**, *37*, 031303.

(43) Bartnik, A. *Opto-Electronics Review* **2015**, *23*, 172–186.

(44) Bruijn, R. de; Bartnik, A.; Fledderus, H. F.; Fiedorowicz, H.; Hegeman, P.; Constantinescu, R. C.; Bijkerk, F. In *Emerging Lithographic Technologies IV*, Emerging Lithographic Technologies IV, SPIE: 2000; Vol. 3997, pp 157–161.

(45) Strocov, V. N.; Schmitt, T.; Flechsig, U.; Schmidt, T.; Imhof, A.; Chen, Q.; Raabe, J.; Betemps, R.; Zimoch, D.; Krempasky, J.; Wang, X.; Grioni, M.; Piazzalunga, A.; Patthey, L. *Journal of Synchrotron Radiation* **2010**, *17*, 631–643.

(46) Le Guyader, L. et al. *Journal of Synchrotron Radiation* **2023**, *30*, 284–300.

(47) Singh, R.; Gupta, M.; Phase, D. M.; Mukherjee, S. K. *Materials Research Express* **2019**, *6*, 116449.

(48) Peth, C.; Barkusky, F.; Mann, K. *Journal of Physics D: Applied Physics* **2008**, *41*, 105202.

(49) Fiedorowicz, H.; Bartnik, A.; Jarocki, R.; Rakowski, R.; Szczurek, M. *Applied Physics B* **2000**, *70*, 305–308.

(50) Wachulak, P.; Fok, T.; Węgrzyński, Ł.; Bartnik, A.; Nyga, P.; Janulewicz, K.; Fiedorowicz, H. *Optics Express* **2021**, *29*, 20514.

(51) Sedlmair, J.; Gleber, S.-C.; Peth, C.; Mann, K.; Niemeyer, J.; Thieme, J. *Journal of Soils and Sediments* **2012**, *12*, 24–34.

(52) Fok, T.; Wachulak, P. W.; Janulewicz, K. A.; Węgrzyński, Ł.; Bartnik, A.; Szlachetko, J.; Zając, M.; Fiedorowicz, H. *Journal of Instrumentation* **2020**, *15*, C05026–C05026.

(53) Müller, M.; Schellhorn, M.; Mann, K. *Journal of Analytical Atomic Spectrometry* **2019**, *34*, 1779–1785.

(54) Wachulak, P.; Fok, T.; Bartnik, A.; Janulewicz, K. A.; Fiedorowicz, H. *Applied Physics B* **2019**, *126*, 11.

(55) Kühl, F.-C.; Müller, M.; Schellhorn, M.; Mann, K.; Wieneke, S.; Eusterhues, K. *Journal of Vacuum Science & Technology A: Vacuum, Surfaces, and Films* **2016**, *34*, 041302.

(56) Gnewkow, R.; Stiel, H.; Jonas, A.; Schönfelder, S.; Probst, J.; Krist, T.; Kanngiesser, B.; Mantouvalou, I. *Optica* **2024**, *11*, 744–752.

(57) Henke, B. L.; Gullikson, E. M.; Davis, J. C. X-Ray Interactions: Photoabsorption, Scattering, Transmission, and Reflection at E=50-30000 eV, Z=1-92, Atomic Data and Nuclear Data Tables Vol. 54 (no.2): 181-342, 1993.

(58) Shari'ati, Y.; Vura-Weis, J. *Journal of Synchrotron Radiation* **2021**, *28*, 1850–1857.

(59) Henke, B. L.; Gullikson, E. M.; Davis, J. C. *Atomic Data and Nuclear Data Tables* **1993**, *54*, 181–342.

Chapter 3

GAS- AND LIQUID-PHASE *IN-SITU* SOFT X-RAY ABSORPTION FOR CARBON CAPTURE AND CONVERSION

3.1 Abstract

Understanding and optimizing the processes of carbon capture and conversion requires *in-situ* techniques that can probe materials and reactions under realistic working conditions in both liquid and gaseous environments. Among the advanced *in-situ* analytical techniques that can probe these materials under actual working conditions, soft X-ray absorption spectroscopy (XAS) has proven particularly high-impact for its ability to access the X-ray water window, the C, O, and N K-edges of organic molecules, and the L-edges of relevant transition metals, providing an element-specific molecular-level probe. This chapter describes the development of a table-top soft X-ray *in-situ* beamline, designed to perform XAS measurements in both gaseous and liquid environments. Gas-phase measurements allow XAS studies on metal organic frameworks, used in direct air capture of CO_2 and H_2O. Liquid-phase *in-situ* capabilities aim to focus on electrocatalytic systems, providing insights into the fundamental processes that govern the selectivity and activity of CO_2 reduction observed in devices and guiding the discovery of new catalysts. To the best of authors' knowledge, this is the first demonstration of liquid-phase *in-situ* soft X-ray absorption measurements using a gaseous-based LPP source. By leveraging rapid advancements in table-top X-ray sources, this beamline brings *in-situ* XAS to the laboratory bench, addressing the accessibility challenges posed by synchrotron facilities. This work aims to establish a modular platform for *in-situ* XAS, facilitating the development of a co-design pipeline that integrates soft X-ray measurements into the catalyst discovery and optimization process.

3.2 Introduction

X-ray absorption spectroscopy (XAS) is a powerful technique to investigate the electronic, structural, and chemical properties of materials. In recent years, *in-situ* XAS has revolutionized the study of electrocatalysts under operational conditions, particularly at synchrotron facilities. These measurements have advanced our understanding of interfacial dynamics, including oxide formation [1–3], carrier dynamics [4, 5], reaction intermediates [6, 7], and facet restructuring [8, 9].

Beyond liquid environments, *in-situ* XAS has been instrumental in studying gas-phase systems, particularly for understanding CO_2 and H_2O adsorption in metal-organic frameworks (MOFs). These studies have illuminated gas adsorption mechanisms [10], defect site reactivity [11], and changes in oxidation state during gas-solid reactions [12]. However, most *in-situ* XAS experiments in MOFs are conducted in the hard X-ray regime, leaving the soft X-ray regime, critical for studying organic molecules and reaction intermediates, largely unexplored.

Soft X-ray (SXR) absorption, which probes the C, N, and O K-edges, offers unique insight into the electronic structure of organic frameworks and catalytic intermediates. However, conducting *in-situ* soft XAS is challenging due to the small mean free path of soft X-rays in matter, illustrated by the calculated attenuation lengths of Cu, Si_3N_4, and H_2O in Figure 3.1. The high degree of absorption in matter requires that SXR measurements be conducted in vacuum environments and *in-situ* cells have micron-scale path-lengths for liquids and gases. These technical constraints require specialized, leak-proof cells capable of maintaining high pressure differentials while preserving the sample environment. *In-situ* SXR experiments have employed a range of techniques from microns-thick liquid jets [13, 14], to microfluidic devices [15, 16]. Furthermore, micrometer thick gas or liquid environments pose a challenge in replicating realistic mass flow conditions, which is often very influential on a given reaction and the actual performance of the device [17, 18].

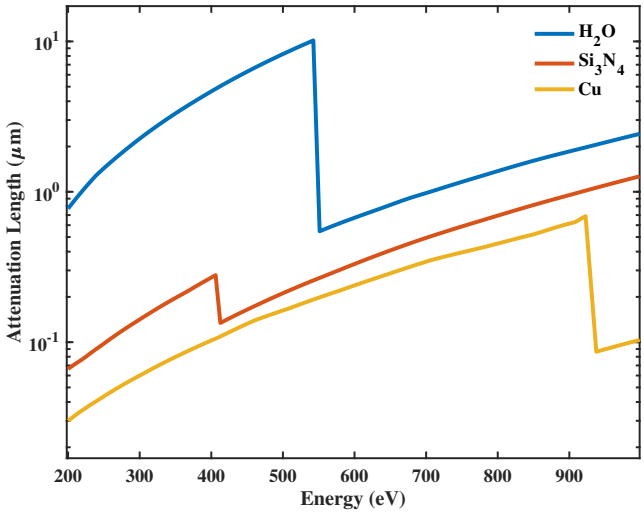

Figure 3.1: Attenuation depth measured into liquid H_2O (blue) solid Cu (yellow) and silicon nitride (Si_3N_4, orange) when the intensity of X-rays is 1/e of its value at the surface over the soft X-ray energy range [19].

Despite their scientific value, *in-situ* synchrotron XAS measurements remain inaccessible to many researchers due to limited beamtime and the complex setup required for soft X-ray experiments. Table-top X-ray sources, such as those based on high harmonic generation (HHG) and laser-produced plasmas (LPP), offer a promising alternative by enabling more accessibility and customization. HHG sources have advanced ultrafast spectroscopy in the extreme ultraviolet (XUV) range [5, 20, 21], the attenuation length of radiation in this energy range is on the order of 10 - 500 nm for liquid water and 10 - 50 nm for gaseous CO_2 [22]. Furthermore, very few HHG sources have demonstrated emission reaching the soft X-ray regime with sufficient flux to measure an absorption edge, let alone conduct *in-situ* measurements [23–25]. In contrast, LPP sources have been utilized for their ability to generate radiation in the soft X-ray regime to perform synchrotron-like absorption measurements in the laboratory [26–29]. Although some reports have shown gas-phase measurements with LPP sources [30], fully liquid *in-situ* measurements have not been demonstrated. Such measurements are particularly challenging with LPP sources due to their significantly lower X-ray intensity compared to synchrotrons. Furthermore, most LPP XAS spectrometers are designed in transmission geometry, necessitating overall sample thicknesses on the order of hundreds of nanometers to several microns, depending on the material.

Although most LPP XAS studies focus on solid samples in vacuum, significant improvements in X-ray optics and gas jet targets have improved the intensity and sensitivity of the LPP source [29, 31–33], increasing its potential to take *in-situ* measurements. This work aims to bridge the gap by developing an *in-situ* cell capable of handling both liquid and gas environments for soft X-ray measurements. The cell features a 3.6 μm-thick channel, enabling transmission through liquid water and gaseous CO_2, crucial for studying electrocatalytic CO_2 reduction and direct air capture processes.

This chapter presents the design and characterization of the *in-situ* cell, highlighting its versatility for studying electrochemical systems and gas-phase reactions. Preliminary measurements demonstrate its capability to use the cell in liquid water and gaseous CO_2 environments, allowing future investigations into catalytic systems and carbon capture materials.

3.3 Experimental Section

The LPP source used in these experiments was described in Chapter 2. In order to maximize X-ray flux for *in-situ* measurements, the higher pulse-energy nanosecond Nd:YAG laser was used (Spectra-Physics Quanta-Ray PRO, 10 Hz repetition rate, 8 ns FWHM pulse duration, 800 mJ pulse energy). All measurements were taken with a plasma generated in Kr gas with backing pressure of 175 psi, delivered by a pulsed gas jet with opening time t_{open} = 900 µs. Visible light and scattered 1064 nm laser light were filtered with a 100 nm Al foil sealed in a gate valve. Gas-phase measurements were taken with a 100 µm slit placed 75 mm after the plasma. Liquid-phase measurements were taken without a slit to maximize X-ray flux at the sample.

The custom built *in-situ* cell used in this work is shown in Figure 3.2. The cell is sealed for vacuum environments by compressing two Si_3N_4 windows against ethylene propylene o-rings at both the entrance and the exit. The Si_3N_4 chip is fabricated on a 5 mm × 5 mm, 200 µm thick silicon square frame with a aperture of 0.5 mm × 0.5 mm. A 50 nm thick Si_3N_4 membrane is deposited on one side of the silicon frame and two 1.8 µm thick SU-8 spacers are fabricated on the Si_3N_4 membrane to create a channel over the free-standing Si_3N_4 window.

The entrance and exit Si_3N_4 chips are placed such that the Si_3N_4 and spacer sides are facing each other, and the channel is aligned so that the other side of the chip is compressed against the ethylene propylene o-ring. A small channel was drilled into the side of the stainless steel frame to serve as a reservoir for excess liquid/gas.

Absorption measurements were calculated using Equation 3.1:

$$A = -\ln\left(\frac{I}{I_0}\right) \tag{3.1}$$

For gas-phase measurements, research-grade CO_2 and atmospheric air at atmospheric pressure (~14 psi) were loaded into the *in-situ* cell, and the corresponding transmitted intensity (I) was measured. Additionally, the transmitted intensity under vacuum (I_0) was recorded for reference. Liquid-phase measurements were performed by loading the *in-situ* cell with distilled water before placing it in the vacuum chamber and measuring the transmitted intensity (I). The transmitted intensity of the cell under vacuum was again used as (I_0). All absorption spectra were normalized using Athena software [34].

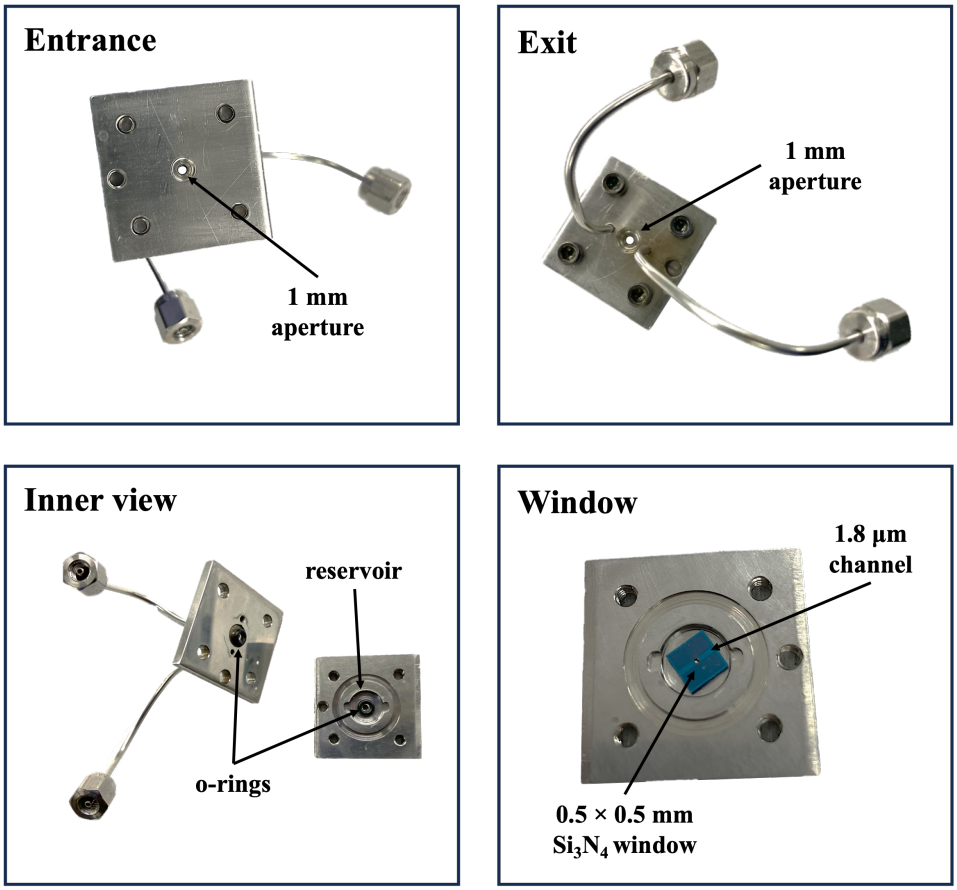

Figure 3.2: *In-situ* cell for in-vacuum soft X-ray absorption measurements. The cell is designed for transmission geometry and can be used with static or flowing media. A vacuum-compatible seal is formed by compression of two Si_3N_4 windows against o-rings, such that a 3.6 µm thick channel is formed for gas or liquid.

The procedures for introducing gas or liquid into the *in-situ* cell during the operation of the vacuum chamber are given in Appendix B. In the measurements presented here, the *in-situ* cell was operated in static mode, however, it can be used with flowing media in future experiments.

All spectra were taken by cooling the camera to -50 °C and subtracting dark counts from the transmission measurement. A liquid nitrogen cold trap was used in the same chamber as the *in-situ* cell to ensure that any leaks from the cell did not result in icing of the camera surface. Due to the size of the *in-situ* cell holder, self-referencing was not used and a separate reference measurement was taken measuring transmission through two Si_3N_4 windows in vacuum.

3.4 Results and Discussion

Gas-phase measurements

Given the short path length of the *in-situ* cell used in this experiment, the calculated decrease in transmission due to the C and O K-edges using gaseous CO_2 is ~1%, while that of O in ambient air (combining the decrease in transmission for CO_2, H_2O, and O_2 at each partial pressure) would be <1% and for the N K-edge, the decrease in transmission would be ~1% [22]. The raw data of X-ray transmission of the *in-situ* cell under vacuum, CO_2, and ambient air is given in Figure B.2.

The measured absorption curve for both CO_2 and air are given in Figure 3.3. X-ray spectra were accumulated for 50 minutes, and absorption curves were smoothed using a locally weighted scatterplot smoothing (LOWESS) with a span of 0.08. The N K-edge is seen in both the CO_2 and ambient air transmission curve, likely due to the interference of the Si_3N_4 windows, however the edge is more pronounced in the air spectrum, due to the higher concentration of N_2 in atmosphere.

Liquid-phase measurements

For liquid water, the calculated transmittance in the liquid cell is ~60% before the O K-edge, and near 0% at the edge and through the higher energies accessible by this spectrometer. However, the observed transmittance was closer to 10% before the edge, suggesting that the path length through the cell increased >10 μm in the high vacuum environment [22]. Bulging of the cell is directly observable in the raw liquid-phase data. The raw data of the transmission of X-rays through the cell with liquid water, and the reference are given in Appendix B. Similar *in-situ* cells for soft X-ray measurements have addressed window deformation by using intermediate chambers filled with helium (highly transmissive to SXRs) to minimize the effects of high pressure differentials [16, 30].

Oxygen K-edge X-ray absorption spectra of water have been widely studied under a variety of conditions, from temperature [35, 36], ion concentration [37, 38], and pH [39, 40] to transient XAS studies [41, 42] and isotope substitution experiments [43, 44]. In this study, the normalized measurements at the O K-edge, shown in Figure 3.4, show agreement with the well-documented structure of liquid H_2O. Specifically, the XAS spectrum matches the approximate positions of the pre-edge peak located at 535 eV, the main-edge peak near 540 eV, and the post-edge peak near 545 eV. The pre-edge peak has been attributed to broken or weakened hydrogen bonds, the main-edge peak attributed to coordinated, interstitial water molecules,

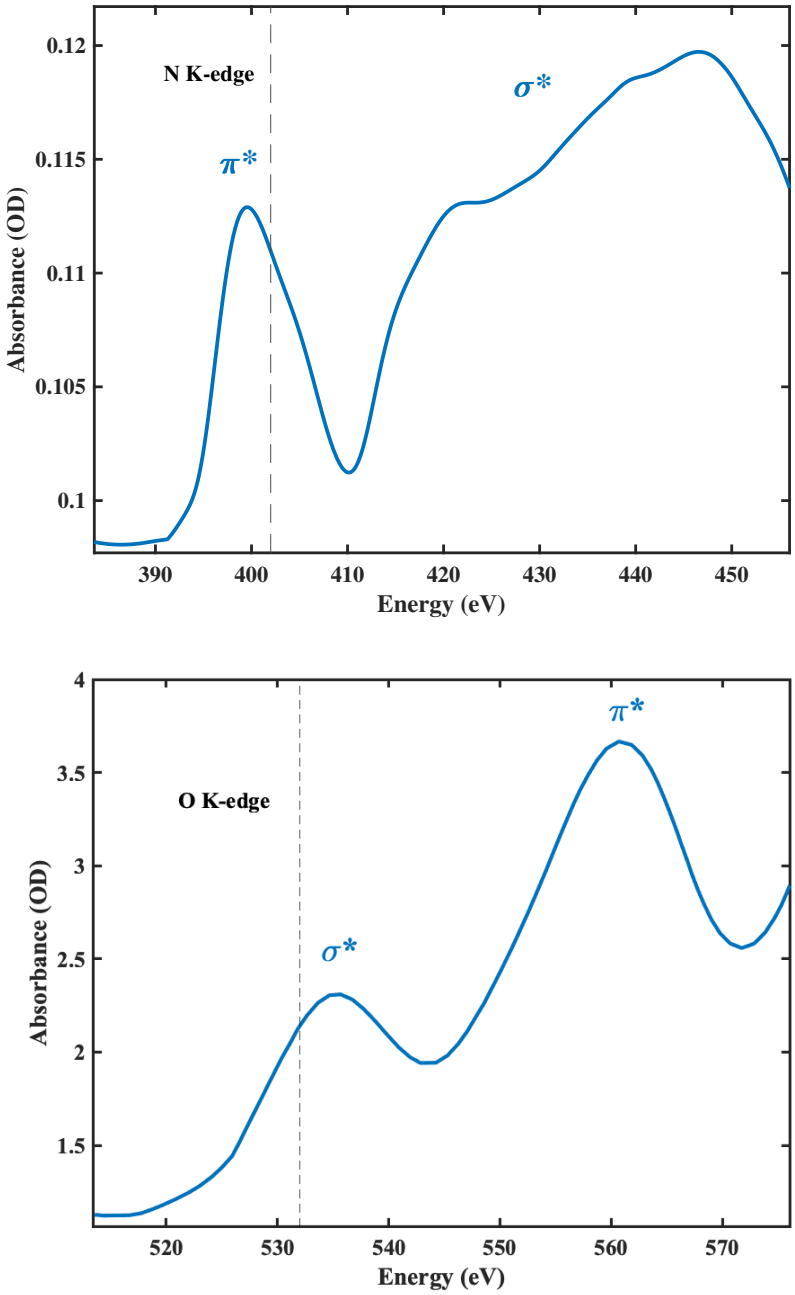

Figure 3.3: N K-edge absorption spectrum for ambient air (top) and C K-edge absorption spectrum of atmospheric pressure CO_2 (bottom). The features corresponding to transitions to the $\sigma*$ and $\pi*$ are annotated. Both spectra were normalized using Athena XAS processing software [34], smoothed with LOWESS smoothing (span size 0.08), and collected over a 50-minute integration time.

and the post-edge peak attributed to stronger hydrogen bonds that tend to increase in intensity for spectra of ice [35, 45, 46].

Figure 3.4 compares the XAS data taken with the LPP spectrometer with synchrotron measurements of the liquid and gas-phase H_2O. The relative intensities of the pre-edge peak and the main-edge peak do not exactly match those of the liquid water measured with the synchrotron; however, the stronger intensity of the pre-edge peak may signify a larger concentration of broken or weakened hydrogen bonds occupying a larger volume, due to the cell bulging in the vacuum environment. In previous work that used DFT calculations to assign peaks in the water O K-edge spectra, the pre-edge peak at 535 eV is attributed to the unoccupied O-H antibonding $4a_1$ orbital of water [46], which would be filled, and thus less intense in stronger H-bonding networks. The increased intensity observed at the pre-edge peak, relative to the main peak, suggests a weaker H-bonding network.

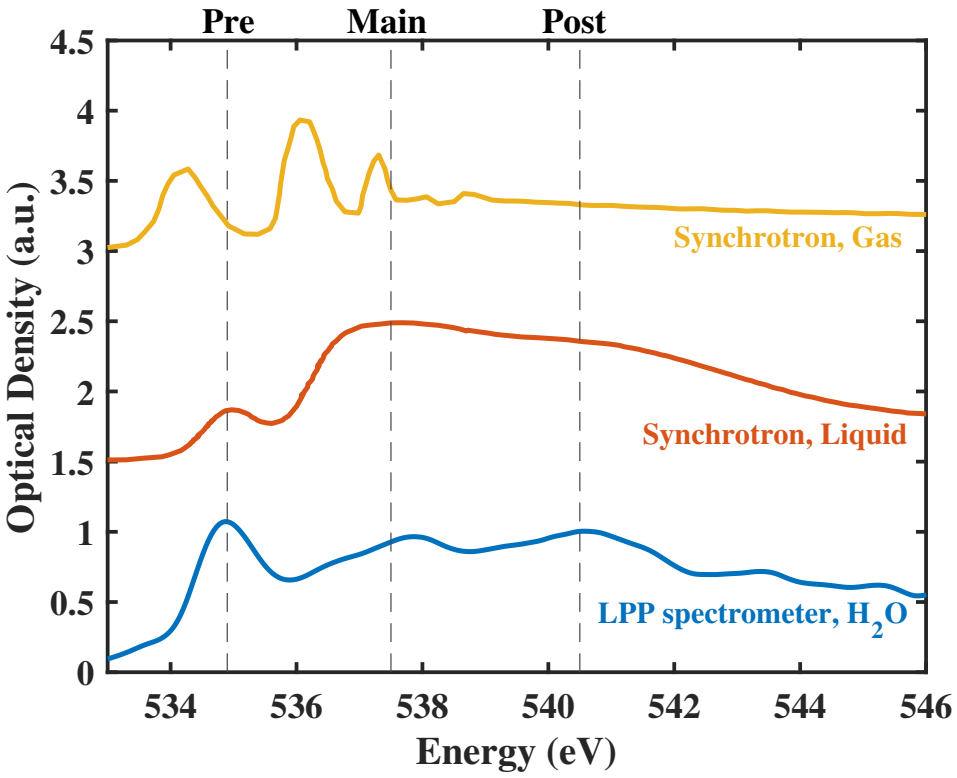

Figure 3.4: Oxygen K-edge absorption spectrum obtained using distilled water in the *in-situ* cell. Comparison of the O K-edge absorption spectrum from liquid and gaseous H_2O, taken at a synchrotron is given as comparison, from ref [47]. The absorbance measurement was taken with an integration time of 16.5 minutes and smoothed using lowess smoothing, with span 0.05.

3.5 Conclusion

A table-top soft X-ray absorption spectrometer based on a LPP in a gaseous target was used to conduct gas- and liquid-phase measurements. A custom built *in-situ* cell with a 3.6 µm thick liquid channel, sealed by two 50 nm thick Si_3N_4 windows, and capable of withstanding vacuum environments, was used for both measurements. Gas-phase measurements of CO_2 and ambient air were performed at the nitrogen and oxygen K-edges, demonstrating that the instrument has a high enough sensitivity to measure low concentration gases relevant to materials used in carbon capture and conversion devices. Liquid-phase measurements of H_2O were also performed and the oxygen K-edge absorption spectrum was compared to synchrotron sources and reported DFT calculations. The relatively high intensity of the pre-edge feature suggests that the bulging of the cell may have led to a lower pressure inside the *in-situ* cell, resulting in weaker hydrogen bonding networks.

Together, these measurements demonstrate the feasibility of studying a wide variety of samples *in-situ*, from electrocatalysts in realistic aqueous electrolyte for CO_2 reduction, to metal organic frameworks, in low concentration gas-phase environments for direct air capture. Demonstrating these capabilities on the table-top provides greater access to *in-situ* XAS techniques that are typically only conducted by a select few beamline and residential staff scientists at large user facilities, increasing the reach of a powerful technique to more users and a wider variety of experiments.

References

(1) Ishiguro, N.; Tada, M. *Catalysis Letters* **2018**, *148*, 1597–1609.

(2) Choi, Y.; Sinev, I.; Mistry, H.; Zegkinoglou, I.; Roldan Cuenya, B. *ACS Catalysis* **2016**, *6*, 3396–3403.

(3) Yang, Y.; Wang, Y.; Xiong, Y.; Huang, X.; Shen, L.; Huang, R.; Wang, H.; Pastore, J. P.; Yu, S.-H.; Xiao, L.; Brock, J. D.; Zhuang, L.; Abruña, H. D. *Journal of the American Chemical Society* **2019**, *141*, 1463–1466.

(4) Zoric, M. R.; Basera, P.; Palmer, L. D.; Aitbekova, A.; Powers-Riggs, N.; Lim, H.; Hu, W.; Garcia-Esparza, A. T.; Sarker, H.; Abild-Pedersen, F.; Atwater, H. A.; Cushing, S. K.; Bajdich, M.; Cordones, A. A. *ACS Nano* **2024**, *18*, 19538–19548.

(5) Liu, H.; Michelsen, J. M.; Mendes, J. L.; Klein, I. M.; Bauers, S. R.; Evans, J. M.; Zakutayev, A.; Cushing, S. K. *The Journal of Physical Chemistry Letters* **2023**, *14*, 2106–2111.

(6) Mohtadi, R.; Mizuno, F. *Beilstein Journal of Nanotechnology* **2014**, *5*, 1291–1311.

(7) Bordiga, S.; Groppo, E.; Agostini, G.; van Bokhoven, J. A.; Lamberti, C. *Chemical Reviews* **2013**, *113*, 1736–1850.

(8) Lee, S. H.; Lin, J. C.; Farmand, M.; Landers, A. T.; Feaster, J. T.; Avilés Acosta, J. E.; Beeman, J. W.; Ye, Y.; Yano, J.; Mehta, A.; Davis, R. C.; Jaramillo, T. F.; Hahn, C.; Drisdell, W. S. *Journal of the American Chemical Society* **2021**, *143*, 588–592.

(9) Wang, M.; Wa, Q.; Bai, X.; He, Z.; Samarakoon, W. S.; Ma, Q.; Du, Y.; Chen, Y.; Zhou, H.; Liu, Y.; Wang, X.; Feng, Z. *JACS Au* **2021**, *1*, 2216–2223.

(10) McDonald, T. M. et al. *Nature* **2015**, *519*, 303–308.

(11) Tofoni, A.; Tavani, F.; Braglia, L.; Colombo, V.; Torelli, P.; D'Angelo, P. *Radiation Physics and Chemistry* **2023**, *213*, 111243.

(12) Zhao, S. et al. *Nature Energy* **2016**, *1*, 1–10.

(13) Wilson, K. R.; Schaller, R. D.; Co, D. T.; Saykally, R. J.; Rude, B. S.; Catalano, T.; Bozek, J. D. *The Journal of Chemical Physics* **2002**, *117*, 7738–7744.

(14) Ekimova, M.; Quevedo, W.; Faubel, M.; Wernet, P.; Nibbering, E. T. J. *Structural Dynamics* **2015**, *2*, 054301.

(15) Fuchs, O.; Maier, F.; Weinhardt, L.; Weigand, M.; Blum, M.; Zharnikov, M.; Denlinger, J.; Grunze, M.; Heske, C.; Umbach, E. *Nuclear Instruments and Methods in Physics Research Section A: Accelerators, Spectrometers, Detectors and Associated Equipment* **2008**, *585*, 172–177.

(16) Nagasaka, M.; Hatsui, T.; Horigome, T.; Hamamura, Y.; Kosugi, N. *Journal of Electron Spectroscopy and Related Phenomena* **2010**, *177*, 130–134.

(17) Hursán, D.; Janáky, C. *Chemical Communications* **2023**, *59*, 1395–1414.

(18) Shafaque, H. W.; Lee, J. K.; Krause, K.; Lee, C.; Fahy, K. F.; Shrestha, P.; Balakrishnan, M.; Bazylak, A. *Energy Conversion and Management* **2021**, *243*, 114302.

(19) Henke, B. L.; Gullikson, E. M.; Davis, J. C. X-Ray Interactions: Photoabsorption, Scattering, Transmission, and Reflection at E=50-30000 eV, Z=1-92, Atomic Data and Nuclear Data Tables Vol. 54 (no.2): 181-342, 1993.

(20) Cushing, S. K.; Porter, I. J.; de Roulet, B. R.; Lee, A.; Marsh, B. M.; Szoke, S.; Vaida, M. E.; Leone, S. R. *Science Advances* **2020**, *6*, eaay6650.

(21) Kim, Y.-J.; Mendes, J. L.; Michelsen, J. M.; Shin, H. J.; Lee, N.; Choi, Y. J.; Cushing, S. K. *Science Advances* **2024**, *10*, 4282.

(22) Henke, B. L.; Gullikson, E. M.; Davis, J. C. *Atomic Data and Nuclear Data Tables* **1993**, *54*, 181–342.

(23) Popmintchev, T. et al. *Science* **2012**, *336*, 1287–1291.

(24) Fu, Y.; Nishimura, K.; Shao, R.; Suda, A.; Midorikawa, K.; Lan, P.; Takahashi, E. J. *Communications Physics* **2020**, *3*, 1–10.

(25) Stein, G. J.; Keathley, P. D.; Krogen, P.; Liang, H.; Siqueira, J. P.; Chang, C.-L.; Lai, C.-J.; Hong, K.-H.; Laurent, G. M.; Kärtner, F. X. *Journal of Physics B: Atomic, Molecular and Optical Physics* **2016**, *49*, 155601.

(26) Sedlmair, J.; Gleber, S.-C.; Peth, C.; Mann, K.; Niemeyer, J.; Thieme, J. *Journal of Soils and Sediments* **2012**, *12*, 24–34.

(27) Fok, T.; Wachulak, P. W.; Janulewicz, K. A.; Węgrzyński, Ł.; Bartnik, A.; Szlachetko, J.; Zając, M.; Fiedorowicz, H. *Journal of Instrumentation* **2020**, *15*, C05026–C05026.

(28) Müller, M.; Schellhorn, M.; Mann, K. *Journal of Analytical Atomic Spectrometry* **2019**, *34*, 1779–1785.

(29) Holburg, J.; Müller, M.; Mann, K.; Wild, P.; Eusterhues, K.; Thieme, J. *Analytical Chemistry* **2022**, *94*, 3510–3516.

(30) Kühl, F.-C.; Müller, M.; Schellhorn, M.; Mann, K.; Wieneke, S.; Eusterhues, K. *Journal of Vacuum Science & Technology A: Vacuum, Surfaces, and Films* **2016**, *34*, 041302.

(31) Wachulak, P.; Duda, M.; Bartnik, A.; Węgrzyński, Ł.; Fok, T.; Fiedorowicz, H. *APL Photonics* **2019**, *4*, 030807.

(32) Węgrzyński, Ł.; Bartnik, A.; Wachulak, P.; Fok, T.; Fiedorowicz, H. *Physics of Plasmas* **2020**, *27*, 073102.

(33) Wachulak, P.; Fok, T.; Węgrzyński, Ł.; Bartnik, A.; Nyga, P.; Janulewicz, K.; Fiedorowicz, H. *Optics Express* **2021**, *29*, 20514.

(34) Ravel, B.; Newville, M. *Journal of Synchrotron Radiation* **2005**, *12*, 537–541.

(35) Wernet, Ph.; Nordlund, D.; Bergmann, U.; Cavalleri, M.; Odelius, M.; Ogasawara, H.; Näslund, L. Å.; Hirsch, T. K.; Ojamäe, L.; Glatzel, P.; Pettersson, L. G. M.; Nilsson, A. *Science* **2004**, *304*, 995–999.

(36) Pylkkänen, T.; Sakko, A.; Hakala, M.; Hämäläinen, K.; Monaco, G.; Huotari, S. *The Journal of Physical Chemistry B* **2011**, *115*, 14544–14550.

(37) Cappa, C. D.; Smith, J. D.; Wilson, K. R.; Messer, B. M.; Gilles, M. K.; Cohen, R. C.; Saykally, R. J. *The Journal of Physical Chemistry B* **2005**, *109*, 7046–7052.

(38) Näslund, L.-Å.; Cavalleri, M.; Ogasawara, H.; Nilsson, A.; Pettersson, L. G. M.; Wernet, P.; Edwards, D. C.; Sandström, M.; Myneni, S. *The Journal of Physical Chemistry A* **2003**, *107*, 6869–6876.

(39) Cavalleri, M.; Näslund, L.-Å.; Edwards, D. C.; Wernet, P.; Ogasawara, H.; Myneni, S.; Ojamäe, L.; Odelius, M.; Nilsson, A.; Pettersson, L. G. M. *The Journal of Chemical Physics* **2006**, *124*, 194508.

(40) Cappa, C. D.; Smith, J. D.; Messer, B. M.; Cohen, R. C.; Saykally, R. J. *The Journal of Physical Chemistry B* **2006**, *110*, 1166–1171.

(41) Wernet, Ph.; Gavrila, G.; Godehusen, K.; Weniger, C.; Nibbering, E. T. J.; Elsaesser, T.; Eberhardt, W. *Applied Physics A* **2008**, *92*, 511–516.

(42) Huse, N.; Wen, H.; Nordlund, D.; Szilagyi, E.; Daranciang, D.; Miller, T. A.; Nilsson, A.; Schoenlein, R. W.; Lindenberg, A. M. *Physical Chemistry Chemical Physics* **2009**, *11*, 3951–3957.

(43) Bergmann, U.; Nordlund, D.; Wernet, Ph.; Odelius, M.; Pettersson, L. G. M.; Nilsson, A. *Physical Review B* **2007**, *76*, 024202.

(44) Fuchs, O.; Zharnikov, M.; Weinhardt, L.; Blum, M.; Weigand, M.; Zubavichus, Y.; Bär, M.; Maier, F.; Denlinger, J. D.; Heske, C.; Grunze, M.; Umbach, E. *Physical Review Letters* **2008**, *100*, 027801.

(45) Myneni, S.; Luo, Y.; Näslund, L. Å.; Cavalleri, M.; Ojamäe, L.; Ogasawara, H.; Pelmenschikov, A.; Wernet, P.; Väterlein, P.; Heske, C.; Hussain, Z.; Pettersson, L. G. M.; Nilsson, A. *Journal of Physics: Condensed Matter* **2002**, *14*, L213.

(46) Cavalleri, M.; Ogasawara, H.; Pettersson, L. G. M.; Nilsson, A. *Chemical Physics Letters* **2002**, *364*, 363–370.

(47) Fransson, T.; Harada, Y.; Kosugi, N.; Besley, N. A.; Winter, B.; Rehr, J. J.; Pettersson, L. G. M.; Nilsson, A. *Chemical Reviews* **2016**, *116*, 7551–7569.

Chapter 4

TRANSIENT SOFT X-RAY ABSORPTION MEASUREMENTS OF TiO_2 WITH A NANOSECOND LASER-PRODUCED PLASMA SOURCE

4.1 Abstract

Using soft X-rays as probes for transient absorption measurements offers insight into the fundamental processes of photoelectrocatalysts following photoexcitation, from oxidation state changes, to charge transfer and even intermediate and product formation. This chapter describes the work done to develop UV-pump/soft-X-ray (SXR) probe spectroscopy using a ns laser-produced plasma (LPP) as an X-ray source in order to expand the capabilities of transient soft X-ray absorption to the table-top. The development and testing of the technique in this chapter was conducted on TiO_2 thin films, which have been previously reported to have lifetimes of the order of tens of nanoseconds. Although efforts to measure a transient signal with TiO_2 thin films were unsuccessful in this work, several potential improvements to the experimental setup are discussed. Specifically, to improve the sensitivity of the instrument, SXR emission from a Kr plasma should be used instead of Ar because it has a more broadband emission spectrum. Higher pump fluences could also be explored to increase the photoexcited carrier density. The spatial overlap of the pump and probe could also be improved with the use of an X-ray focusing optic. Additionally, spectral and temporal resolution could be improved using higher quality X-ray gratings and shorter pulse duration lasers, respectively.

4.2 Introduction

Understanding excited-state dynamics is critical to building a repository of knowledge that will become design principles for more efficient electrocatalysts. Theoretical simulations, such as density functional theory (DFT), can provide guidance in this pursuit; however, direct spectroscopic evidence is required to draw definite conclusions. Pump-probe, or time-resolved, spectroscopy has been imperative to elucidating carrier dynamics, charge transfer, and reaction intermediates in electrochemical systems [1–3]. Time-resolved spectroscopy utilizes two pulses of light, a pump, and a probe to measure the evolution of a material in response to a strong perturbation. The "pump" pulse excites a large enough fraction of the material

such that the relaxation of the material in this excited-state can be measured by the subsequent "probe" pulse as a function of time by adjusting the delay between the two pulses. Pump-probe transient absorption spectroscopy is one of the most widely used time-resolved spectroscopies and measures the absorption of a broad-band visible probe pulse following excitation by a pump pulse. With improvement of ultrafast lasers this technique has been useful for studying dynamics on timescales as short as attoseconds [4–6]. As they are applied to photoelectrochemical systems, most pump-probe transient absorption spectroscopies utilize visible or infrared (IR) probes that can access an ensemble of transitions between the valence and conduction bands, or structural modes, respectively [7–9]. While IR probes provide insight into structural modes, they cannot measure the electronic structure of a particular catalyst or provide insight into element-specific dynamics. Visible probes of valence states are sensitive to the surrounding chemical environment and often result in broad peaks of overlapping spectral features. Additionally, in electrochemical devices, dynamics such as charge transfer can be tuned by adding dopants to the catalyst, so an element-specific probe would be needed to elucidate their role in the observed changes in charge transfer.

Transient X-ray absorption spectroscopy (tr-XAS) is ideally suited for studying excited-state dynamics of electrocatalysts because it can access transitions from highly localized core orbitals. These core orbitals are not changed by the external environment, but more sensitive to the local electronic structure. Thus, X-rays are excellent element-specific probes of changes in the oxidation state, spin states, and charge carriers [10, 11].

Traditionally, transient absorption measurements that use X-rays (>200 ev) as probes have been conducted at XFELs. Similarly to *in-situ* X-ray measurements, time-resolved measurements with X-rays are much more complex and involved than the linear absorption techniques more commonly utilized at beamlines. This puts a natural bottleneck on the number of transient X-ray absorption measurements that are achievable within the electrochemical community. Table-top sources for pulsed X-ray beams thus offer an attractive alternative to user facilities and have the added benefit of broadband simultaneous emission. At most XAS beamlines at synchrotrons, the incoming X-ray beam is monochromated before interaction with the sample such that the measurement time for a given spectrum is limited by the time it takes to physically scan a given energy range. Laser-produced plasma (LPP) sources for soft and hard X-rays are commonly used for ground-state measurements

and have less frequently been explored for time-resolved measurements. Most time-resolved studies conducted with LPP sources have consisted of time-resolved X-ray diffraction [12–16], however, a few time-resolved XAS measurements have been conducted with LPP sources. Some examples of this work include the elucidation of trap states in organic molecules [17, 18]

Although the repetition rate of the Nd:YAG laser is orders of magnitude lower than that of common Ti:Sapph lasers routinely used to conduct ultrafast transient extreme ultraviolet studies using high harmonic generation (10-20 Hz compared to 1 kHz, respectively), smaller repetition rate in combination with electronic delays may prove advantageous for measuring longer timescale dynamics. For example, in electrochemical systems, oxide formation, particle corrosion, charge transfer, and diffusion occur on the nanosecond to millisecond to minute time scales [19–22].

In this study, a table-top ultraviolet-pump/soft-X-ray (SXR)-probe transient absorption spectrometer based on a LPP source is constructed and tested to measure the excited-state dynamics of TiO_2 thin films. Due to limitations of the experimental setup at the time these experiments were attempted, no transient signal was measured from TiO_2. Instrumental improvements are discussed to conduct successful time-resolved measurements in the future.

4.3 Experimental Section

The SXR source is based on a LPP, generated using an Nd:YAG laser (Spectra-Physics Quanta-Ray PRO, 1064 nm, 10 Hz repetition rate, 8 ns FWHM pulse duration, 800 mJ pulse energy) and a pulsed gas jet inside of a vacuum chamber. The spectrometer is largely the same as that in Chapter 2, with the exception of a few components. The time-resolved measurements conducted here were attempted using Ar gas with a backing pressure of 150 psi, using a pulsed gas jet with a 900 µs opening time, electronically delayed and triggered by a pulse generator inside the Nd:YAG oscillator. Any scattered 1064 nm light from the laser and out-of-band radiation from the plasma is filtered out using a 100 nm thick Al filter. The SXR beam passed through 100 µm slit, was dispersed by an aberration-corrected concave X-ray grating (Hitachi PN 001-0659, 2400 l/mm, 563.2 mm focal length) and measured with an in-vacuum electron-multiplying CCD (Raptor photonics EMCCD III-XV, 10 × 10 µm pixel size, 1024 × 1024 pixels). A second 100 nm Al filter on a translation arm is placed after the X-ray grating and before the EMCCD to block any scattered light by the pump beam. During operation of the gas jet, the plasma

generation chamber is held at 10^{-3} Torr and the rest of the setup remains between 10^{-5}-10^{-6} Torr.

The pump pulse is delivered by a separate Nd:YLF laser (Spectra-Physics, Explorer One, 10 ns FWHM pulse duration, 10 Hz repetition rate, 70 µJ pulse energy) whose fundamental 1047 nm beam is frequency tripled by third harmonic generation (THG) in crystals of lithium triborate (LBO) to give a 349 nm beam. The timing of the pump pulse is controlled by a digital delay/pulse generator (Stanford Research Systems, DG535), triggered by the same TTL output from the pulse generator in the Nd:YAG's oscillator that controls the gas jet timing. A schematic of the setup is shown in Figure 4.1.

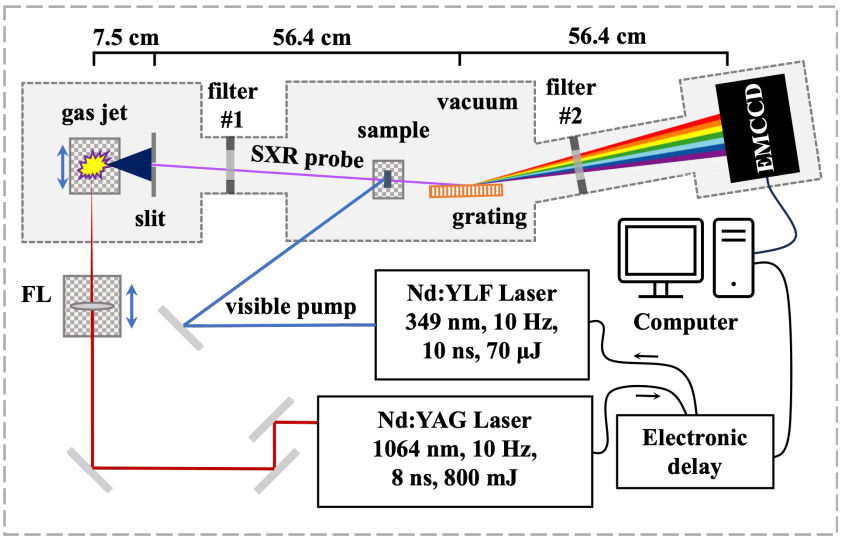

Figure 4.1: Schematic of the experimental setup to conduct pump-probe transient SXR absorption measurements using a LPP source. This setup utilizes an electronic delay line to alter the timing of the pump laser with respect to the SXR probe. The computer controls the timing of the pump pulse delay and acquisition by the EMCCD camera.

Self-referencing was used during the time-resolved measurements so that the differential absorption was calculated using Equation 4.1,

$$\Delta A = -\ln\left(\frac{I_{s,\,pump\,on}/I_{0,\,pump\,on}}{I_{s,\,pump\,off}/I_{0,\,pump\,off}}\right) \tag{4.1}$$

Where $I_{s,\,pump\,on}$ refers to the transmitted intensity of the SXRs that have passed through the sample, following photoexcitation by the pump, where $I_{s,\,pump\,off}$ refers to that where the pump pulse was not present. Similarly, $I_{0,\,pump\,on}$ refers to the

transmitted intensity of the SXRs through the reference after the pump pulse was delivered to the sample and $I_{0,\,pump\,on}$ refers to that where no pump was present.

The TiO_2 thin film sample was prepared by atomic layer deposition (ALD) on 50 nm thick diamond membranes with 2 mm diameter apertures. The thin film preparation method was the same as described in Appendix A, however, the number of cycles was increased to 1400 to deposit 70 nm of TiO_2 on the diamond membrane.

Temporal overlap was approximated using a photodiode sensitive to UV-IR light (Thorlabs, DET36A2, Si detector, 350-1100 nm, 14 ns rise time). The temporal overlap was conducted in atmosphere by placing the photodiode in the sample position and removing the metallic filter between the plasma chamber and the sample. The Nd:YAG was used to generate a plasma in atmosphere such that the visible light emitted from the plasma was used as a proxy for the SXR probe. The timing between the pump laser and the Nd:YAG was then varied so that approximate time zero could be determined. The results of the temporal overlap are given in Appendix C.

In the initial efforts to find a transient response of the sample, absorption spectra were acquired at >10 time delays. One time point was selected with a delay that was many milliseconds longer than the expected lifetime of the material. In this case, given the 10 Hz repetition rate of both the pump laser and the probe, this was selected as 50 ms. At this time point, the delay is so large that no response is expected to be measurable by the SXR probe, and the absorbance calculated here can be effectively considered steady state. The other time delays were selected within 1 ms of the time zero measured by the temporal overlap.

Spatial overlap was determined by first measuring the SXR beam's full width at half maximum (FWHM) and midpoint using knife edge positioning. X-ray intensity was recorded at various horizontal positions (x) of the edge of the razor blade as it moved into the beam path. The resulting intensity data were fit to a complementary error function ($I(x)$) as a function of the position of the razor blade. The function used to fit the intensity data is given in Equation 4.2:

$$I(x) = a \times erf\left(\frac{x-b}{c}\right) + d \tag{4.2}$$

The first derivative of this fit was used to calculate the FWHM to give the approximate size of the SXR beam in the horizontal dimension. The midpoint of the beam was

identified by finding the relative x position at the maximum y value of the first derivative. The results of this experiment are shown in Figure C.2.

Since the pump beam was not focused in these experiments, the pump beam dimensions were measured with a laser beam analyzer (BeamGage, Ophir, SP620U) to be 6.294×10^3 µm by 4.918×10^3 µm by the second moment, or D4σ, standard which defines the dimensions of a laser beam to be four times the standard deviation of the energy distribution along the two axes of the beam intensity profile. The pump beam was centered on the sample after positioning the sample stage to maximize X-ray transmission. With these specifications, the pump fluence was calculated to be 0.25 mJ/cm^2, which was used to calculate the average carrier density, ΔN, using Equation 4.3 [23].

$$\Delta N = \frac{F}{\hbar\omega d_s}\left(1 - e^{-\alpha d_s}\right) \tag{4.3}$$

where F is the pump fluence in J/cm^2, $\hbar$ is Plancks constant in J/Hz, ω is the central frequency of the pump laser in Hz, α is the absorption coefficient in cm^{-1}, and d_s is the sample thickness in cm. Using a sample thickness of 70 nm and an absorption coefficient of 2.52×10^4 cm^{-1} [24], the average carrier density was calculated to be 1×10^{19} cm^{-3}.

4.4 Results and Discussion

As mentioned, the time-resolved soft X-ray spectra of TiO_2 thin films, at the Ti $L_{2,3}$ edge did not show any transient signal in this work. In these measurements, a range of time delays were measured and compared to a temporal delay of 50 ms. The 50 ms time delay was chosen as a control, such that the pump arrived at the sample with ample time for the transient response to decay before the arrival of the probe. In the spectra collected in this work, no meaningful transient response was detected, as compared to the control. Previous reports measured the lifetimes of photoexcited TiO_2 on the scale of nanoseconds to tens of nanoseconds [25–27].

The lack of a measurable transient response can be explained by a number of possibilities. First, the X-ray grating used in this study has been shown to produce aberration in X-ray spectra, as shown in Figure C.3. For the spectra taken here, the FWHM of a Gaussian fit to the nitrogen emission line at 430.8 eV (λ = 2.878 nm) was 1.4 eV, corresponding to a spectral resolution of E/ΔE = 299. This resolution may be too low to resolve transient excited-state populations on the <1 eV scale.

Additionally, as mentioned in Chapter 2, the SXR emission spectra of an Ar plasma is dominated by characteristic line emission. Small variations in gas expansion can result in differences in electron temperature in the plasma, resulting in shot-to-shot variations that exacerbate the spectral variability of the different characteristic lines in the Ar plasma emission spectrum. The Kr emission spectrum, on the other hand, is dominated by broadband *bremsstrahlung* emission, making the fluctuations in plasma conditions less pronounced in the resulting absorption spectra. This is illustrated in Figure A.6, which compares the absorption spectrum of the N K-edge obtained with the Ar and Kr plasmas.

Temporal resolution could also be a limiting factor in these experiments, as the measured lifetime of photoexcited TiO_2 has been reported to be on the scale of nanoseconds to tens of nanoseconds [25–27]. Given the 10 ns pump pulses and the 8 ns probe pulses, the excited-state population would have decayed to <40% on the ns timescale, based on previous work using X-ray probes in time-resolved studies [25, 26]. However, optical transient absorption measurements have measured that recombination rates in anatase and rutile TiO_2 are on the order of ms [28]. Future studies could test the excited-state lifetimes of different crystal structures of TiO_2 (anatase or rutile).

Furthermore, the pump power for these measurements was calculated to excite 1×10^{19} cm^{-3} carriers, which is within the typical range of 10^{19}-10^{20} cm^{-3} necessary to detect a transient. However, other studies that investigated the lifetime of photoexcited TiO_2 thin film used higher pump fluences, in the range of tens of mJ/cm^2 [25, 26]. This, in addition to the fact that the probe beam interacted with a larger area of the sample than the pump, could have resulted in a population of excited atoms too small for the sensitivity of the instrument. Future time-resolved experiments could explore X-ray focusing optics, which have undergone significant technical improvement, and have been demonstrated to improve flux in for many LPP-based techniques [29–31].

4.5 Interpreting time-resolved X-ray spectra

The interpretation of the time-resolved X-ray spectra has been explored using theoretical models based on the Bethe-Salpeter equation (BSE). This method has been developed by modifications to the Obtaining Core Excitations using *Ab initio* and the NIST BSE solver (OCEAN) code [32–34]. In this method density functional theory (DFT) is used as a starting point to calculate the ground-state energies of a given

system using Quantum-ESPRESSO. In OCEAN calculations, there is an optional step to account for electron self-energies with Hedin's GW self-energy approximation. The GW approximation is a correction for ground-state energies derived from the one-electron Green's function and the screened Coulomb interaction (denoted G and W, respectively) [35]. Then, core-excitation spectra are calculated with BSE. This approach offers an advantage over time-dependent density functional theory (TDFT) because it includes an explicit treatment of particle-hole interactions [36].

Past methods to calculate excited-state XAS spectra have used a state filling technique in which electron and hole populations are calculated based on the energy of the pump beam and the available states based on a materials band structure [32–34]. Although this technique has shown good agreement with measured transient XUV spectra [32–34], it is an approximation of the occupied states and would not work as well for materials where many-body effects and more dispersive bands near the pump energy are present. More accurate modeling of excited-state carrier occupations has relied on the Boltzmann transport equation (BTE) [37], which includes material properties such as electronic structure, lattice dynamics, and electron–phonon collision in the calculation of excited-state occupations. This can be integrated into the existing method of using OCEAN to calculate excited-state X-ray spectra by using DFT to calculate the ground-state energies of a given system and then using the BTE to calculate excited-state populations at time points after photoexcitation. Together, these techniques could improve the interpretation of time-resolved XAS spectra, including that measured of TiO_2 thin films.

4.6 Conclusion

Time-resolved UV-pump/SXR-probe experiments were explored using a table-top nanosecond SXR spectrometer based on a LPP source. To validate the experimental setup, the lifetime of a TiO_2 thin film was investigated. In the experimental configuration presented here, no transient was detected; however, several contributing factors were explored and discussed. Specifically, the instrument's sensitivity was likely too low to detect small mOD changes induced by photoexcitation of the TiO_2 thin film. Sensitivity of the setup could be improved in further experiments by using SXR emission from a Kr plasma, larger pump fluences, and a shorter pulse duration driving laser. In addition to improving temporal resolution with a shorter SXR pulse, spectral resolution could be improved by using higher line density X-ray gratings, enabling detection of peak shifts <1 eV.

Given these improvements, future time-resolved studies using the LPP source presented here are feasible. Bringing time-resolved XAS capabilities to the table-top in the SXR regime would expand the reach of the technique beyond large-scale user facilities, enabling researchers to elucidate the fundamental dynamics that occur within molecular and material systems to govern device performance. Furthermore, extending this technique to the SXR regime using LPP spectrometers would complement the capabilities of HHG-based spectrometers, which are currently capable of routine transient extreme ultraviolet (XUV) measurements.

References

(1) Cushing, S. K.; Carneiro, L. M.; Zuerch, M.; Chang, H.-T.; Leone, S. R. *ECS Meeting Abstracts* **2017**, *MA2017-02*, 1876.

(2) Baran, T.; Fracchia, M.; Vertova, A.; Achilli, E.; Naldoni, A.; Malara, F.; Rossi, G.; Rondinini, S.; Ghigna, P.; Minguzzi, A.; D'Acapito, F. *Electrochimica Acta* **2016**, *207*, 16–21.

(3) Saes, M.; Bressler, C.; Abela, R.; Grolimund, D.; Johnson, S. L.; Heimann, P. A.; Chergui, M. *Physical Review Letters* **2003**, *90*, 047403.

(4) Cistaro, G.; Plaja, L.; Martín, F.; Picón, A. *Physical Review Research* **2021**, *3*, 013144.

(5) Ramasesha, K.; Leone, S. R.; Neumark, D. M. *Annual Review of Physical Chemistry* **2016**, *67*, 41–63.

(6) Beck, A. R.; Neumark, D. M.; Leone, S. R. *Chemical Physics Letters* **2015**, *624*, 119–130.

(7) Liu, S.; D'Amario, L.; Jiang, S.; Dau, H. *Current Opinion in Electrochemistry* **2022**, *35*, 101042.

(8) Liu, H.; Qi, Z.; Song, L. *The Journal of Physical Chemistry C* **2021**, *125*, 24289–24300.

(9) Wang, J.; Wang, K.; Wang, F.-B.; Xia, X.-H. *Nature Communications* **2014**, *5*, 5285.

(10) Als-Nielsen, J.; McMorrow, D., *Elements of Modern X-ray Physics*, 1st ed.; Wiley: 2011.

(11) Cushing, S. K.; Lee, A.; Porter, I. J.; Carneiro, L. M.; Chang, H.-T.; Zürch, M.; Leone, S. R. *The Journal of Physical Chemistry C* **2019**, *123*, 3343–3352.

(12) Quevedo, W.; Peth, C.; Busse, G.; Scholz, M.; Mann, K.; Techert, S. *International Journal of Molecular Sciences* **2009**, *10*, 4754–4771.

(13) Pudell, J.; Maznev, A. A.; Herzog, M.; Kronseder, M.; Back, C. H.; Malinowski, G.; von Reppert, A.; Bargheer, M. *Nature Communications* **2018**, *9*, 3335.

(14) Juvé, V.; Holtz, M.; Zamponi, F.; Woerner, M.; Elsaesser, T.; Borgschulte, A. *Physical Review Letters* **2013**, *111*, 217401.

(15) Sokolowski-Tinten, K.; Blome, C.; Blums, J.; Cavalleri, A.; Dietrich, C.; Tarasevitch, A.; Uschmann, I.; Förster, E.; Kammler, M.; Horn-von-Hoegen, M.; von der Linde, D. *Nature* **2003**, *422*, 287–289.

(16) Uschmann, I.; Kämpfer, T.; Zamponi, F.; Lübcke, A.; Zastrau, U.; Loetzsch, R.; Höfer, S.; Morak, A.; Förster, E. *Applied Physics A* **2009**, *96*, 91–98.

(17) Stiel, H.; Braenzel, J.; Jonas, A.; Gnewkow, R.; Glöggler, L. T.; Sommer, D.; Krist, T.; Erko, A.; Tümmler, J.; Mantouvalou, I. *International Journal of Molecular Sciences* **2021**, *22*, 13463.

(18) Jonas, A.; Dammer, K.; Stiel, H.; Kanngiesser, B.; Sánchez-de-Armas, R.; Mantouvalou, I. *Analytical Chemistry* **2020**, *92*, 15611–15615.

(19) Li, H.; Yu, P.; Lei, R.; Yang, F.; Wen, P.; Ma, X.; Zeng, G.; Guo, J.; Toma, F. M.; Qiu, Y.; Geyer, S. M.; Wang, X.; Cheng, T.; Drisdell, W. S. *Angewandte Chemie International Edition* **2021**, *60*, 24838–24843.

(20) Zhang, L.; Mohamed, H. H.; Dillert, R.; Bahnemann, D. *Journal of Photochemistry and Photobiology C: Photochemistry Reviews* **2012**, *13*, 263–276.

(21) Cho, I.; Zhao, L.; Mapley, J. I.; Shahshahan, S.; Wagner, P.; Gordon, K. C.; Innis, P. C.; Kimura, M.; Mori, S.; Mozer, A. J. *The Journal of Physical Chemistry C* **2020**, *124*, 9178–9190.

(22) Drisdell, W.; Lee, S. H.; Acosta, J. A.; Lee, D.; Larson, D.; Li, H.; Chen, J.; Blair, S.; Gallo, A.; Zheng, H.; Tassone, C.; Jaramillo, T. Structural Transformation and Degradation of Cu Nanocatalysts during Electrochemical CO2 Reduction Reaction `https://www.researchsquare.com/article/rs-3204416/v1` (accessed 08/20/2024), pre-published.

(23) Cushing, S. K.; Zürch, M.; Kraus, P. M.; Carneiro, L. M.; Lee, A.; Chang, H.-T.; Kaplan, C. J.; Leone, S. R. *Structural Dynamics* **2018**, *5*, 054302.

(24) Siefke, T.; Kroker, S.; Pfeiffer, K.; Puffky, O.; Dietrich, K.; Franta, D.; Ohlídal, I.; Szeghalmi, A.; Kley, E.-B.; Tünnermann, A. *Advanced Optical Materials* **2016**, *4*, 1780–1786.

(25) Rittmann-Frank, M. H.; Milne, C. J.; Rittmann, J.; Reinhard, M.; Penfold, T. J.; Chergui, M. *Angewandte Chemie International Edition* **2014**, *53*, 5858–5862.

(26) Park, S. H.; Katoch, A.; Chae, K. H.; Gautam, S.; Miedema, P.; Cho, S. W.; Kim, M.; Wang, R.-P.; Lazemi, M.; de Groot, F.; Kwon, S. *Nature Communications* **2022**, *13*, 2531.

(27) Qian, R.; Zong, H.; Schneider, J.; Zhou, G.; Zhao, T.; Li, Y.; Yang, J.; Bahnemann, D. W.; Pan, J. H. *Catalysis Today* **2019**, *335*, 78–90.

(28) Kafizas, A.; Wang, X.; Pendlebury, S. R.; Barnes, P.; Ling, M.; Sotelo-Vazquez, C.; Quesada-Cabrera, R.; Li, C.; Parkin, I. P.; Durrant, J. R. *The Journal of Physical Chemistry A* **2016**, *120*, 715–723.

(29) Mann, K.; Holburg, J.; Lange, S.; Müller, M.; Schäfer, B. In *Extreme Ultraviolet (EUV) Lithography X*, Extreme Ultraviolet (EUV) Lithography X, SPIE: 2019; Vol. 10957, pp 305–310.

(30) Wachulak, P. W.; Torrisi, A.; Bartnik, A.; Węgrzyński, Ł.; Fok, T.; Fiedorowicz, H. *Applied Physics B* **2017**, *123*, 25.

(31) Müller, M.; Mey, T.; Niemeyer, J.; Mann, K. *Optics Express* **2014**, *22*, 23489.

(32) Klein, I. M.; Liu, H.; Nimlos, D.; Krotz, A.; Cushing, S. K. *Journal of the American Chemical Society* **2022**, *144*, 12834–12841.

(33) Klein, I. M.; Krotz, A.; Lee, W.; Michelsen, J. M.; Cushing, S. K. *The Journal of Physical Chemistry C* **2023**, *127*, 1077–1086.

(34) Liu, H.; Michelsen, J. M.; Mendes, J. L.; Klein, I. M.; Bauers, S. R.; Evans, J. M.; Zakutayev, A.; Cushing, S. K. *The Journal of Physical Chemistry Letters* **2023**, *14*, 2106–2111.

(35) Vinson, J.; Rehr, J. J.; Kas, J. J.; Shirley, E. L. *Physical Review B* **2011**, *83*, 115106.

(36) Vinson, J. Bethe-Salpeter Equation Approach for Calculations of X-ray Spectra. Seattle, WA: University of Washington, 2012.

(37) Zhou, J.-J.; Park, J.; Lu, I.-T.; Maliyov, I.; Tong, X.; Bernardi, M. *Computer Physics Communications* **2021**, *264*, 107970.

Chapter 5

CONCLUSION AND FUTURE OUTLOOK

In the fields of carbon capture and conversion, X-ray absorption spectroscopy (XAS) has become key to understanding the underlying physics and chemistry that govern overall device performance. With their ability to access high-energy transitions from the core orbitals of the atom to the valence state, XAS measurements offer a powerful element-specific probe of local electronic structure, oxidation state, hybridization, and bonding. Soft X-rays (SXRs) offer a particularly valuable tool to the field of carbon capture and conversion because they can access the X-ray water window through which carbon- and nitrogen-based molecules, as well as many transition metals, can be measured in aqueous environments.

Access to absorbance measurements in this regime previously required access to large-scale user facilities such as synchrotrons and XFELs. These facilities have enabled numerous high-impact experiments; however, access is limited. Ultimately, this limits the reach of XAS techniques and makes more complex experiments nearly impossible for everyday users. Table-top instrumentation that can access the SXR energy range for absorption measurements offers the distinct advantages of accessibility, customizability, and economy. Additionally, the current moment is experiencing a flourishing of X-ray optics and detectors, in addition to plasma targets, making table-top techniques even more accessible [17, 24, 32, 50]. Laser-produced plasma (LPP) sources, particularly those based on gaseous targets, have been gaining adoption due to their ability to conduct high-quality synchrotron-like XAS measurements with successful applications in the study of organic samples [51], transition metal oxides [52], and polymers [53]. In addition, they have recently enabled more complex techniques, such as extended X-ray absorption spectroscopy (EXAFS) to measure bond lengths [54] and gas-phase reactions [55], as well as time resolved near edge X-ray absorption fine structure (NEXAFS) studies of photoinduced phase transitions [18] and transition metal complexes in liquid sample cells [56].

The work described in this thesis details the efforts to bring *in-situ* and time-resolved XAS to the table top using a soft X-ray source based on laser-produced plasma emission. This has included exploring the lower temporal limit of pulse duration for

X-ray emission in plasmas generated in gas, and the development of a UV-pump/SXR probe time-resolved technique to measure charge transfer in transition metal oxides. Improvements to the technique were discussed in detail, so that this experiment can be fully realized in the future. In an effort to bring *in-situ* measurements to the table-top, the first gas-phase and liquid-phase measurements were achieved with the LPP-based spectrometer built here, a first for liquid-phase soft X-ray absorption on the table top using a gaseous LPP.

In-situ and time-resolved XAS techniques have proven critical to understanding photodriven dynamics, liquid/solid and gas/solid interfaces, and catalyst performance, influencing the discovery-design pipeline of catalysts and materials used for carbon capture and conversion. Table-top X-ray instrumentation to increase the accessibility of XAS measurements will further achieve this goal of realizing eventual ubiquity of XAS measurements.

BIBLIOGRAPHY

(1) Zoric, M. R.; Basera, P.; Palmer, L. D.; Aitbekova, A.; Powers-Riggs, N.; Lim, H.; Hu, W.; Garcia-Esparza, A. T.; Sarker, H.; Abild-Pedersen, F.; Atwater, H. A.; Cushing, S. K.; Bajdich, M.; Cordones, A. A. *ACS Nano* **2024**, *18*, 19538–19548.

(2) Bokarev, S. I.; Khan, M.; Abdel-Latif, M. K.; Xiao, J.; Hilal, R.; Aziz, S. G.; Aziz, E. F.; Kühn, O. *The Journal of Physical Chemistry C* **2015**, *119*, 19192–19200.

(3) Lapteva, L. L.; Fedoseeva, Yu. V.; Shlyakhova, E. V.; Makarova, A. A.; Bulusheva, L. G.; Okotrub, A. V. *Journal of Materials Science* **2019**, *54*, 11168–11178.

(4) Swallow, J. E. N.; Fraser, M. W.; Kneusels, N.-J. H.; Charlton, J. F.; Sole, C. G.; Phelan, C. M. E.; Björklund, E.; Bencok, P.; Escudero, C.; Pérez-Dieste, V.; Grey, C. P.; Nicholls, R. J.; Weatherup, R. S. *Nature Communications* **2022**, *13*, 6070.

(5) Stöhr, J., *NEXAFS Spectroscopy*; Springer Science & Business Media: 2013; 415 pp.

(6) Lewenstein, M.; Balcou, Ph.; Ivanov, M. Yu.; L'Huillier, A.; Corkum, P. B. *Physical Review A* **1994**, *49*, 2117–2132.

(7) Rothhardt, J.; Hädrich, S.; Demmler, S.; Krebs, M.; Winters, D. F. A.; Kühl, T.; Stöhlker, T.; Limpert, J.; Tünnermann, A. *Physica Scripta* **2015**, *2015*, 014030.

(8) Zürch, M.; Chang, H.-T.; Borja, L. J.; Kraus, P. M.; Cushing, S. K.; Gandman, A.; Kaplan, C. J.; Oh, M. H.; Prell, J. S.; Prendergast, D.; Pemmaraju, C. D.; Neumark, D. M.; Leone, S. R. *Nature Communications* **2017**, *8*, 15734.

(9) Cushing, S. K.; Porter, I. J.; de Roulet, B. R.; Lee, A.; Marsh, B. M.; Szoke, S.; Vaida, M. E.; Leone, S. R. *Science Advances* **2020**, *6*, eaay6650.

(10) Liu, H.; Michelsen, J. M.; Mendes, J. L.; Klein, I. M.; Bauers, S. R.; Evans, J. M.; Zakutayev, A.; Cushing, S. K. *The Journal of Physical Chemistry Letters* **2023**, *14*, 2106–2111.

(11) Mantouvalou, I.; Jonas, A.; Witte, K.; Jung, R.; Stiel, H.; Kanngießer, B. In *X-Ray Lasers and Coherent X-ray Sources: Development and Applications*, X-Ray Lasers and Coherent X-ray Sources: Development and Applications, SPIE: 2017; Vol. 10243, pp 15–22.

(12) Peth, C.; Kalinin, A.; Barkusky, F.; Mann, K.; Toennies, J. P.; Rusin, L. Y. *Review of Scientific Instruments* **2007**, *78*, 103509.

(13) Hansson, B. A. M.; Hemberg, O.; Hertz, H. M.; Berglund, M.; Choi, H.-J.; Jacobsson, B.; Janin, E.; Mosesson, S.; Rymell, L.; Thoresen, J.; Wilner, M. *Review of Scientific Instruments* **2004**, *75*, 2122–2129.

(14) Vrba, P.; Vrbová, M.; Brůža, P.; Pánek, D.; Krejčí, F.; Kroupa, M.; Jakůbek, J. *Journal of Physics: Conference Series* **2012**, *370*, 012049.

(15) Bayer, A.; Barkusky, F.; Döring, Stefan; Großmann, P.; Mann, K. *X-Ray Optics and Instrumentation* **2010**, *2010*, 1–9.

(16) Müller, M.; Kühl, F.-C.; Großmann, P.; Vrba, P.; Mann, K. *Optics Express* **2013**, *21*, 12831.

(17) Holburg, J.; Müller, M.; Mann, K.; Wild, P.; Eusterhues, K.; Thieme, J. *Analytical Chemistry* **2022**, *94*, 3510–3516.

(18) Grossmann, P.; Rajkovic, I.; Moré, R.; Norpoth, J.; Techert, S.; Jooss, C.; Mann, K. *Review of Scientific Instruments* **2012**, *83*, 053110.

(19) Qian, R.; Zong, H.; Schneider, J.; Zhou, G.; Zhao, T.; Li, Y.; Yang, J.; Bahnemann, D. W.; Pan, J. H. *Catalysis Today* **2019**, *335*, 78–90.

(20) Carneiro, L. M.; Cushing, S. K.; Liu, C.; Su, Y.; Yang, P.; Alivisatos, A. P.; Leone, S. R. *Nature Materials* **2017**, *16*, 819–825.

(21) Zhang, L.; Mohamed, H. H.; Dillert, R.; Bahnemann, D. *Journal of Photochemistry and Photobiology C: Photochemistry Reviews* **2012**, *13*, 263–276.

(22) Fok, T.; Wachulak, P.; Węgrzyński, Ł.; Bartnik, A.; Nowak, M.; Nyga, P.; Kostecki, J.; Nasiłowska, B.; Skrzeczanowski, W.; Pietruszka, R.; Janulewicz, K.; Fiedorowicz, H. *Materials* **2021**, *14*, 7337.

(23) Wachulak, P.; Duda, M.; Bartnik, A.; Węgrzyński, Ł.; Fok, T.; Fiedorowicz, H. *APL Photonics* **2019**, *4*, 030807.

(24) Mann, K.; Holburg, J.; Lange, S.; Müller, M.; Schäfer, B. In *Extreme Ultraviolet (EUV) Lithography X*, Extreme Ultraviolet (EUV) Lithography X, SPIE: 2019; Vol. 10957, pp 305–310.

(25) Attwood, D., *Soft X-Rays and Extreme Ultraviolet Radiation: Principles and Applications*, 1st ed.; Cambridge University Press: 1999.

(26) *Strong Field Laser Physics*; Brabec, T., Ed.; Springer Series in Optical Sciences, Vol. 134; Springer New York: New York, NY, 2009.

(27) Keldysh, L. V. *SOVIET PHYSICS JETP* **1965**, *20*, 1307–1314.

(28) Colombant, D.; Tonon, G. F. *Journal of Applied Physics* **1973**, *44*, 3524–3537.

(29) Chen, F. F., *Introduction to Plasma Physics and Controlled Fusion*; Springer International Publishing: Cham, 2016.

(30) Rakowski, R.; Bartnik, A.; Fiedorowicz, H.; de Gaufridy de Dortan, F.; Jarocki, R.; Kostecki, J.; Mikołajczyk, J.; Ryć, L.; Szczurek, M.; Wachulak, P. *Applied Physics B* **2010**, *101*, 773–789.

(31) Fiedorowicz, H.; Bartnik, A.; Szczurek, M.; Daido, H.; Sakaya, N.; Kmetik, V.; Kato, Y.; Suzuki, M.; Matsumura, M.; Tajima, J.; Nakayama, T.; Wilhein, T. *Optics Communications* **1999**, *163*, 103–114.

(32) Holburg, J.; Müller, M.; Mann, K. *Optics Express* **2021**, *29*, 6620.

(33) Murnane, M. M.; Kapteyn, H. C.; Rosen, M. D.; Falcone, R. W. *Science* **1991**, *251*, 531–536.

(34) Als-Nielsen, J.; McMorrow, D., *Elements of Modern X-ray Physics*, 1st ed.; Wiley: 2011.

(35) Giulietti, D.; Gizzi, L. A. *La Rivista del Nuovo Cimento (1978-1999)* **1998**, *21*, 1–93.

(36) Hagena, O. F. *Surface Science* **1981**, *106*, 101–116.

(37) Ditmire, T.; Smith, R. A.; Marjoribanks, R. S.; Kulcsár, G.; Hutchinson, M. H. R. *Applied Physics Letters* **1997**, *71*, 166–168.

(38) Khosrofian, J. M.; Garetz, B. A. *Applied Optics* **1983**, *22*, 3406–3410.

(39) Kramida, A.; Ralchenko, Y. NIST Atomic Spectra Database, NIST Standard Reference Database 78, National Institute of Standards and Technology: 1999.

(40) Wachulak, P.; Duda, M.; Bartnik, A.; Sarzyński, A.; Węgrzyński, Ł.; Nowak, M.; Jancarek, A.; Fiedorowicz, H. *Optics Express* **2018**, *26*, 8260.

(41) Vrba, P.; Vrbova, M.; Zakharov, S. V.; Zakharov, V. S. *Physics of Plasmas* **2014**, *21*, 073301.

(42) Holburg, J.; Müller, M.; Mann, K.; Wieneke, S. *Journal of Vacuum Science & Technology A: Vacuum, Surfaces, and Films* **2019**, *37*, 031303.

(43) Bartnik, A. *Opto-Electronics Review* **2015**, *23*, 172–186.

(44) Bruijn, R. de; Bartnik, A.; Fledderus, H. F.; Fiedorowicz, H.; Hegeman, P.; Constantinescu, R. C.; Bijkerk, F. In *Emerging Lithographic Technologies IV*, Emerging Lithographic Technologies IV, SPIE: 2000; Vol. 3997, pp 157–161.

(45) Strocov, V. N.; Schmitt, T.; Flechsig, U.; Schmidt, T.; Imhof, A.; Chen, Q.; Raabe, J.; Betemps, R.; Zimoch, D.; Krempasky, J.; Wang, X.; Grioni, M.; Piazzalunga, A.; Patthey, L. *Journal of Synchrotron Radiation* **2010**, *17*, 631–643.

(46) Le Guyader, L. et al. *Journal of Synchrotron Radiation* **2023**, *30*, 284–300.

(47) Singh, R.; Gupta, M.; Phase, D. M.; Mukherjee, S. K. *Materials Research Express* **2019**, *6*, 116449.

(48) Peth, C.; Barkusky, F.; Mann, K. *Journal of Physics D: Applied Physics* **2008**, *41*, 105202.

(49) Fiedorowicz, H.; Bartnik, A.; Jarocki, R.; Rakowski, R.; Szczurek, M. *Applied Physics B* **2000**, *70*, 305–308.

(50) Wachulak, P.; Fok, T.; Węgrzyński, Ł.; Bartnik, A.; Nyga, P.; Janulewicz, K.; Fiedorowicz, H. *Optics Express* **2021**, *29*, 20514.

(51) Sedlmair, J.; Gleber, S.-C.; Peth, C.; Mann, K.; Niemeyer, J.; Thieme, J. *Journal of Soils and Sediments* **2012**, *12*, 24–34.

(52) Fok, T.; Wachulak, P. W.; Janulewicz, K. A.; Węgrzyński, Ł.; Bartnik, A.; Szlachetko, J.; Zając, M.; Fiedorowicz, H. *Journal of Instrumentation* **2020**, *15*, C05026–C05026.

(53) Müller, M.; Schellhorn, M.; Mann, K. *Journal of Analytical Atomic Spectrometry* **2019**, *34*, 1779–1785.

(54) Wachulak, P.; Fok, T.; Bartnik, A.; Janulewicz, K. A.; Fiedorowicz, H. *Applied Physics B* **2019**, *126*, 11.

(55) Kühl, F.-C.; Müller, M.; Schellhorn, M.; Mann, K.; Wieneke, S.; Eusterhues, K. *Journal of Vacuum Science & Technology A: Vacuum, Surfaces, and Films* **2016**, *34*, 041302.

(56) Gnewkow, R.; Stiel, H.; Jonas, A.; Schönfelder, S.; Probst, J.; Krist, T.; Kanngiesser, B.; Mantouvalou, I. *Optica* **2024**, *11*, 744–752.

(57) Henke, B. L.; Gullikson, E. M.; Davis, J. C. X-Ray Interactions: Photoabsorption, Scattering, Transmission, and Reflection at E=50-30000 eV, Z=1-92, Atomic Data and Nuclear Data Tables Vol. 54 (no.2): 181-342, 1993.

(58) Shari'ati, Y.; Vura-Weis, J. *Journal of Synchrotron Radiation* **2021**, *28*, 1850–1857.

(59) Henke, B. L.; Gullikson, E. M.; Davis, J. C. *Atomic Data and Nuclear Data Tables* **1993**, *54*, 181–342.

Appendix A

SUPPLEMENTARY INFORMATION FOR APPROACHING THE LOWER LIMIT OF PULSE DURATION FOR LASER-PRODUCED PLASMA SOURCES

A.1 Energy calibration of the LPP spectrometer

To perform the energy calibration for all spectra in this thesis, the emission lines originating from the N VI and Ar XI ions are used to create a calibration curve relating camera pixel and energy.

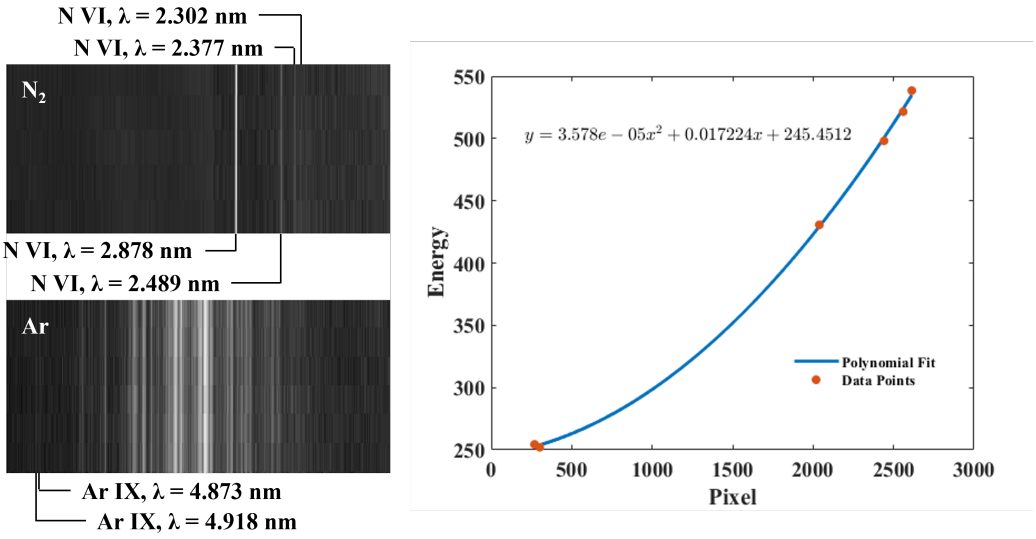

Figure A.1: Location of the emission lines from N VI and Ar XI ions, specified below, are used to calibrate the instrument and representative calibration curve relating pixel and energy. These lines were chosen because they are not obscured by other emission lines or bremmstrahlung radiation in the Ar and N_2 SXR emission spectra.

A.2 Thin film sample preparation methods

Several thin film preparation techniques were explored to meet the >1 μm path-length requirement for soft X-ray transmission measurements. Although atomic layer deposition (ALD) was used in the NEXAFS measurements given in Chapter 2, other methods were explored for a variety of sample types and conditions.

Method for preparation of TiO_2 thin films on diamond membranes by ALD

TiO_2 thin films were deposited on diamond membranes using a Fiji F200 ALD System. Each cycle consisted of the following sequence: a 100 ms pulse of tetrakis (dimethylamido) titanium (TDMAT), held at 75°C, followed by a 15 s waiting step to evacuate the remaining precursor, a 60 ms pulse of H_2O, held at room temperature, followed by an additional 15s waiting step. This was repeated for 800 cycles to yield a 40 nm thick film. To avoid breaking the diamond thin films in the high-vacuum environment of the instrument, they were loaded into the ALD resting on two quartz slides, so that both sides of the membrane experienced the same pressure. The quartz slides could then be used with other analytical techniques to confirm the film thickness. Thin films were deposited on the membrane side of the chip.

Method for preparation of nanoparticle films on diamond membranes by spin coating

Spin coating was explored as a technique to evenly deposit a thin film of nanoparticles on 50 diamond membranes. This procedure was developed for 50 nm anatase TiO_2 nanoparticles (β-TiO_2, MKnano, 98% Pure (hydrophilic), MKN-TiO_2-A050) but can be adapted for other nanoparticles. Most spin coaters use vacuum to secure the sample to the chuck during rotation. Since diamond membranes are very fragile and would break if attached directly to the chuck in this way, it was found that gel-pak sticky boxes (Ted Pella, NC9035618) work well as an intermediate during spin coater operation. The diamond membrane is placed in the middle of the gel pak, with the membrane side up and centered on the spin coater. 95 mg of the β-TiO_2 nanoparticles are suspended in 1 ml of distilled water with a concentration of 1.2 M and vortexed before each coat. 10 µL of this suspension is placed on the membrane side of the diamond chip and spun at 5000 rpm for 30 seconds with a 10-second acceleration time. After each coat, any residual water is evaporated using a heat gun ∼1 ft from the membrane for 10 seconds. This procedure is repeated 12 times to give a film with an average thickness of 75 nm throughout the measurement region (approximated from CXRO [57], see Figure A.2).

Method for preparation of free-standing polymer films

The following procedure is adapted from reference [58]. In an effort to make free-standing thin films ≤ 200 µm, suitable for conducting transmission SXR absorption measurements, polymer films were synthesized. These films served either as a matrix for molecular or nanoparticle samples or as a substrate for spin-coating

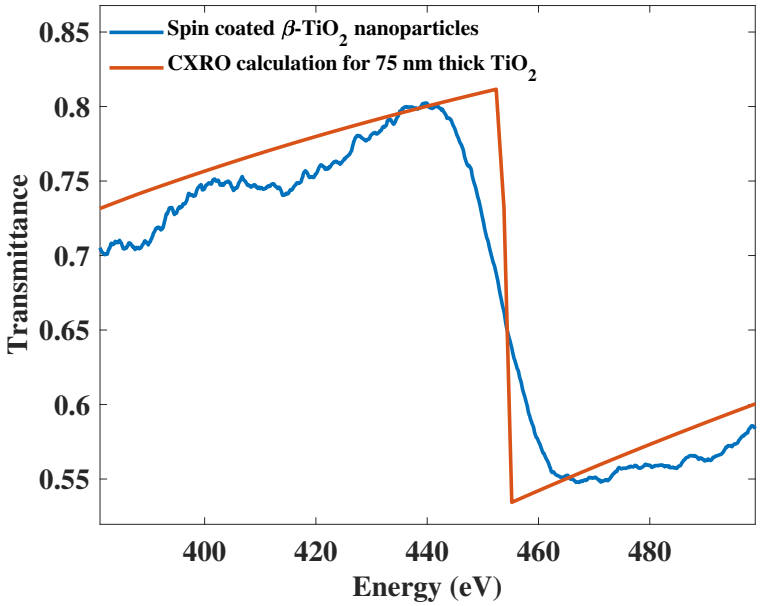

Figure A.2: Transmission of β-TiO_2 nanoparticle thin film deposited on a 50 nm thick diamond membrane by spin coating, measured with an Ar plasma and smoothed using a 0.1 smoothing factor. CXRO calculated transmission data for a 75 nm film of TiO_2 is also given to approximate the nanoparticle layer thickness [57].

a sample. The general procedure involves dissolving either polystyrene (PS) or polyvinyl chloride (PVC) in a solvent (with or without the molecule of interest), sonicating, filtering through a silica column, slip-coating onto a glass slide, and delaminating via water flotation or adhesive tape.

Preparation of Polymer Thin Films: Microscope slides were cleaned with isopropyl alcohol and dried with a heat gun prior to use. For PS films, 1.5 wt% PS was dissolved in dichloromethane. For PVC films, 1.5 wt% PVC was dissolved in a solvent mixture of 93.5% tetrahydrofuran (THF) and 5% cyclohexanone. Each solution was sonicated for 30–60 minutes until fully dissolved. Subsequent steps were performed in a fume hood to prevent contamination. The sonicated solution was filtered through a silica column, with the volume cycled through the column three times. If the polymer was to act as a matrix, the analyte was added at this stage and vortexed for 10 seconds.

Slip Coating: A 100 µL aliquot of the solution was dropped onto a clean microscope slide. For frosted slides, the unfrosted side was used to slip coat the polymer. Another slide was placed face down, with half of each slide overhanging. The top slide was pulled across the bottom slide to evenly spread the solution and avoid

bubble formation. Both slides were flipped polymer side-up and allowed to dry for 60s in the fume hood. The residual solvent was evaporated by exposing the slides to a heat gun for 10s.

Delamination: Films were delaminated using either water or adhesive tape. If an analyte was spin-coated onto the film, it was preferable to delaminate using adhesive tape, as water delamination could disrupt or dissolve the analyte layer. Various sample frame designs and aperture sizes (up to 10 mm) were tested and the films demonstrated good durability.

For *water delamination*, a razor blade was used to cut the film on the slide, leaving at least 2 mm of film around the edges of the intended aperture to allow attachment to the frame on each side. The cut section was slowly slid into water, initiating delamination from the microscope slide. The slide was then submerged until the film detached and floated on the surface of the water. The sample frame was then submerged beneath the floating polymer film, allowing lifting of the frame to secure the film from below.

For *adhesive delamination*, four strips of tape were overlapped to form a frame with a central aperture. An edge of the tape was lifted, suspending the polymer film within the adhesive frame.

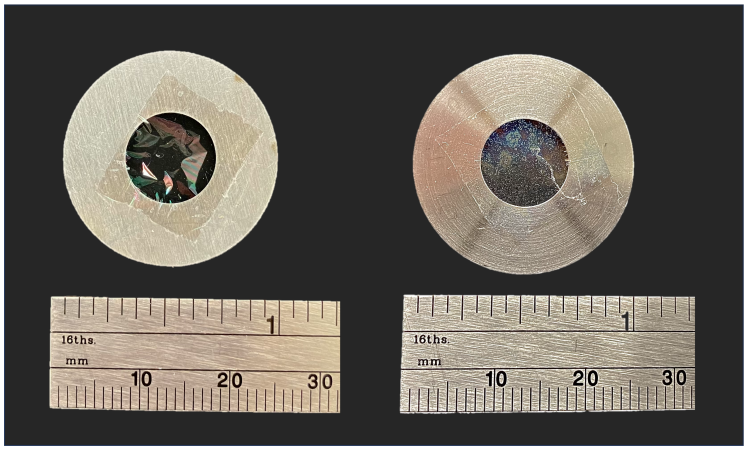

Figure A.3: PVC (left) and PS (right) polymer thin films delaminated by water flotation and deposited on stainless steel frames. Procedure for slip coating polymer thin films was adapted from ref [58].

A.3 Input energies and coupling efficiencies for ps and ns driving lasers

To measure the total energy absorbed by the plasma using the ns and ps lasers, the input energy was compared to the output energy with and without the pulsed gas jet firing (to compare the energy fraction absorbed by the plasma).

Input Energy (mJ)	**Absorbed Energy (mJ)**	**Absorption Fraction (%)**
67.76	59.61	87.98
64.40	56.46	87.67
62.10	54.22	87.30
59.16	51.35	86.80
57.22	49.45	86.42
53.77	46.15	85.82
50.23	41.69	82.99
46.28	37.81	81.70
42.83	34.38	80.27
38.79	30.51	78.68
35.56	27.09	76.18
30.82	22.40	72.68
27.14	18.86	69.51
23.09	15.16	65.66
19.60	11.64	59.41
16.10	8.05	50.00
13.61	6.00	44.07
10.00	3.19	31.98
7.27	1.21	16.67
4.78	0.17	3.61

Table A.1: Input energy, absorbed energy and absorbed energy percentage by the Ar plasma generated with the 23 ps laser.

Input Energy (mJ)	**Absorbed Energy (mJ)**	**Absorption Fraction (%)**
639.40	234.64	36.7
621.00	217.05	35.0
588.80	213.58	36.3
575.00	205.79	35.8
538.20	189.26	35.2
519.80	183.46	35.3
473.80	167.93	35.4
427.80	132.56	31.0
391.00	128.39	32.8
354.20	96.05	27.1
317.40	75.02	23.6
299.00	85.43	28.6
289.80	82.80	28.6
266.80	62.05	23.3
255.30	79.97	31.3
232.30	72.41	31.2
213.90	12.58	5.9
190.90	39.39	20.6
144.90	30.83	21.3

Table A.2: Input energy, absorbed energy and absorbed energy percentage by the Ar plasma generated with the 8 ns laser.

A.4 Gas jet optimization for soft X-ray flux

To maximize X-ray emission from the plasma generated using the ps laser source, a number of pulsed gas jet conditions were explored and are shown in Figure A.4.

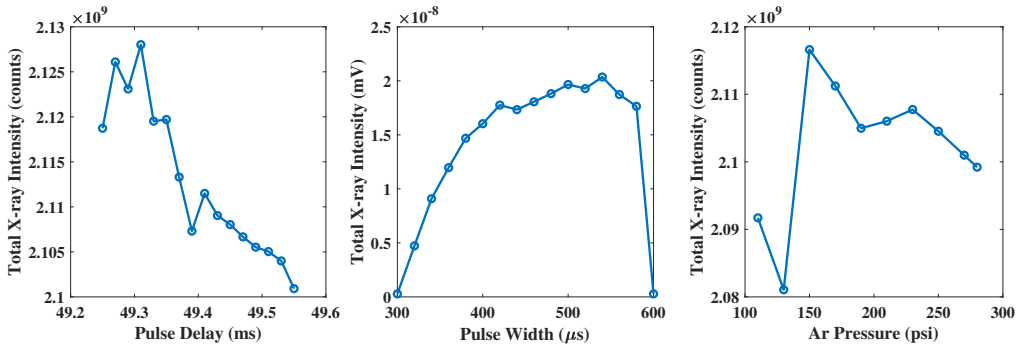

Figure A.4: Optimization of the X-ray emission by various gas jet conditions. The optimal pulse delay between the gas jet and the laser was determined by measuring total CCD counts from an Ar plasma (left). The width of the gas pulse was assessed using an X-ray photodiode placed after the Ar plasma and a 300 nm Al filter (center). The effect of varying the backing pressure of Ar gas on X-ray emission was evaluated by measuring total CCD counts (right).

A.5 Analysis of NEXAFS acquisition methods

To obtain high-quality NEXAFS spectra, the integration time and self-referencing method were explored at the Ti $L_{2,3}$- and O K-edges for the TiO_2 thin film in Figure A.5. The difference in the absorption data collected with the Kr and Ar plasmas is given in Figure A.6.

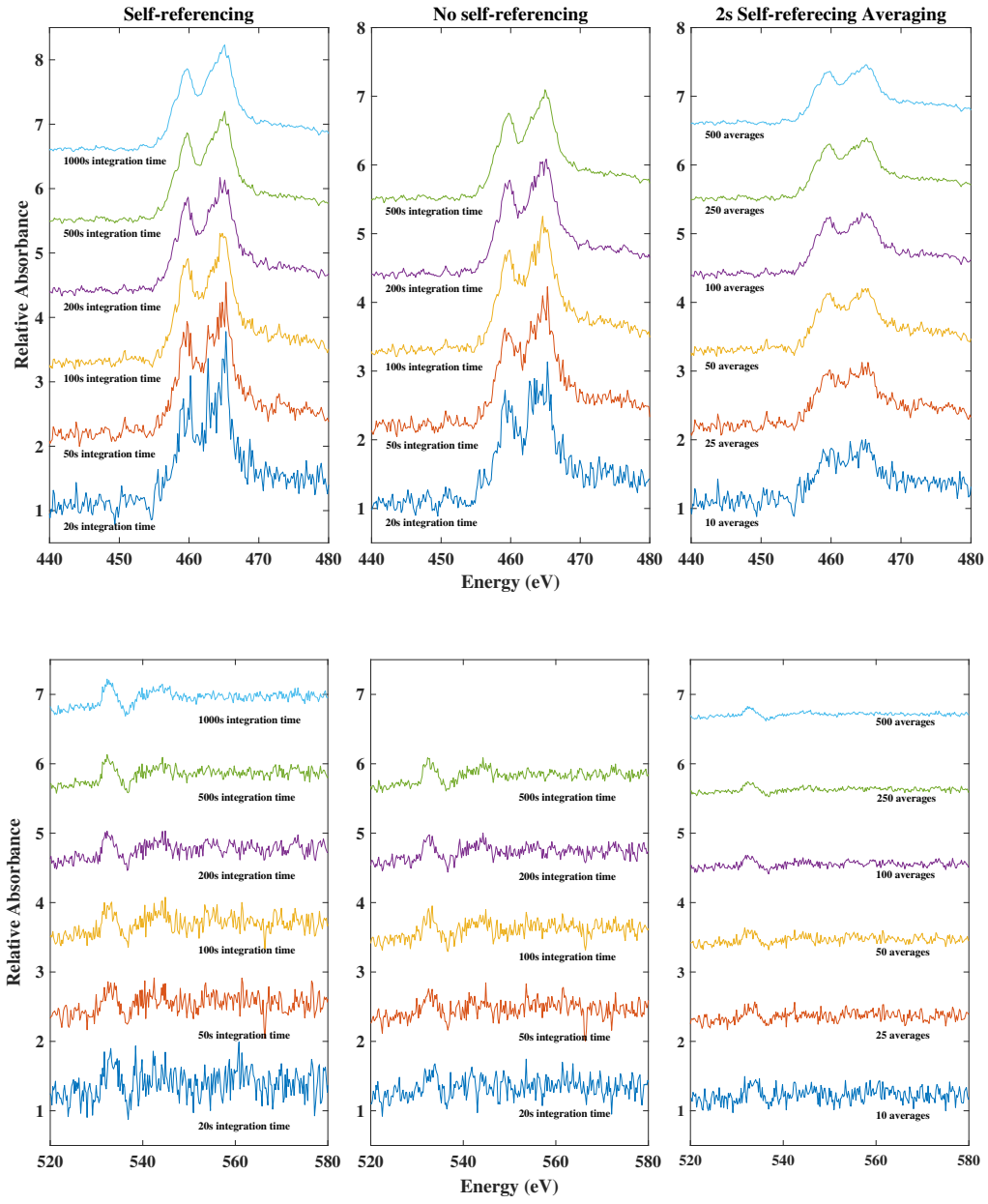

Figure A.5: Comparison of the different methods to process NEXAFS data using the raw data from the Ti $L_{2,3}$-edge (top) and O K-edge (bottom). The left plot compares various integration times using a self-referencing scheme (sample and reference spectra were taken simultaneously). The middle plot compares various integration times without the self-referencing scheme (sample and reference spectra were taken at different times). The relatively little difference in the edge quality underscores that the advantage of the self-referencing scheme is in its ability to minimize the deleterious effects of the decreasing flux due to gas jet nozzle damage. The plot on the right depicts the edge calculated by a self-referencing scheme with a 2 s integration time and averaging over 10 - 500 separate measurements.

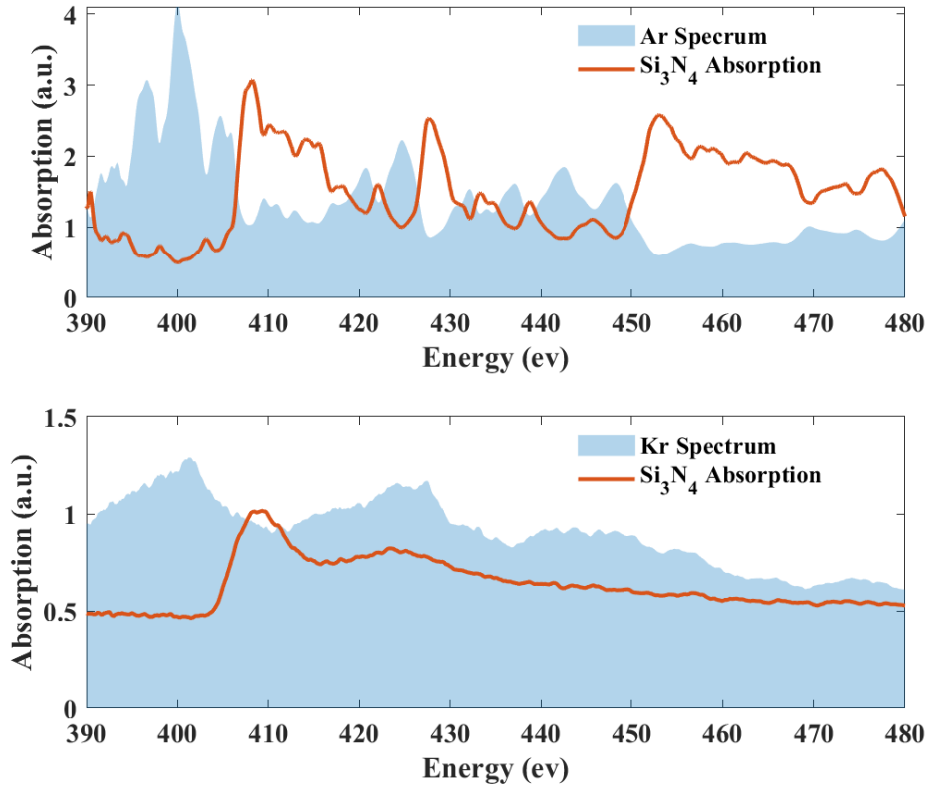

Figure A.6: Comparison of NEXAFS spectra acquired with Ar plasma emission (top) and Kr plasma emission (bottom). The emission spectra used to calculate the absorption edges here are scaled and shown in the background in blue for reference. It can be noted that the highly structured emission spectrum of Ar is dominated by characteristic line emission, making it difficult to fully resolve the N K-edge. By comparison, the Kr emission spectrum is more continuous, resulting in a cleaner edge. The Ar absorption spectrum taken with Ar was accumulated over 38 s and that taken with Kr was accumulated over 6.5 minutes. Both emission and absorption spectra from the Ar and Kr plasmas were smoothed with a LOWESS regression with a 0.004 span.

Appendix B

SUPPLEMENTARY INFORMATION FOR GAS AND LIQUID *IN-SITU* SOFT X-RAY ABSORPTION WITH A LASER-PRODUCED PLASMA SOURCE

B.1 Procedure for evacuating gas cell

The following procedure was developed to operate the *in-situ* cell in a vacuum environment. A diagram of the setup is shown in Figure B.1. During evacuation of the sample chamber, the valve to the roughing pump, V1, is slowly opened with both valves to the *in-situ* cell, V2 and V3, closed to minimize disturbance to the 50 nm thick Si_3N_4 windows. Once the pressure equilibrates to $\sim 10^{-2}$ Torr, V3 is opened with V2 remaining closed. At this point, the turbo pumps are turned on and the chamber will decrease to $\sim 10^{-6}$ Torr. Reference spectra or any other alignment may proceed at this time. To fill the *in-situ* cell with gas, V3 is closed and V2 is opened, exposing the inside of the cell to gas, while monitoring the pressure in the chamber for leaks. When the chamber is brought back to atmospheric pressure, the valves to the *in-situ* cell, V2 and V3 are closed before the other pumps are turned off. During this process, the cell can return to atmospheric pressure with the contents evacuated or under atmospheric pressure.

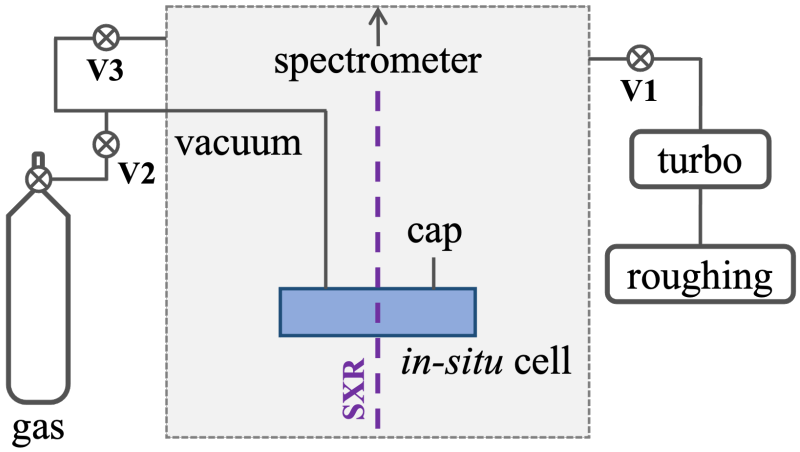

Figure B.1: Piping diagram of experimental setup for conducting gas-phase experiments using the *in-situ* cell.

B.2 Gas-phase X-ray transmission

The raw data of the measured X-ray transmission through the *in-situ* cell through CO_2 and air are given in Figure B.2.

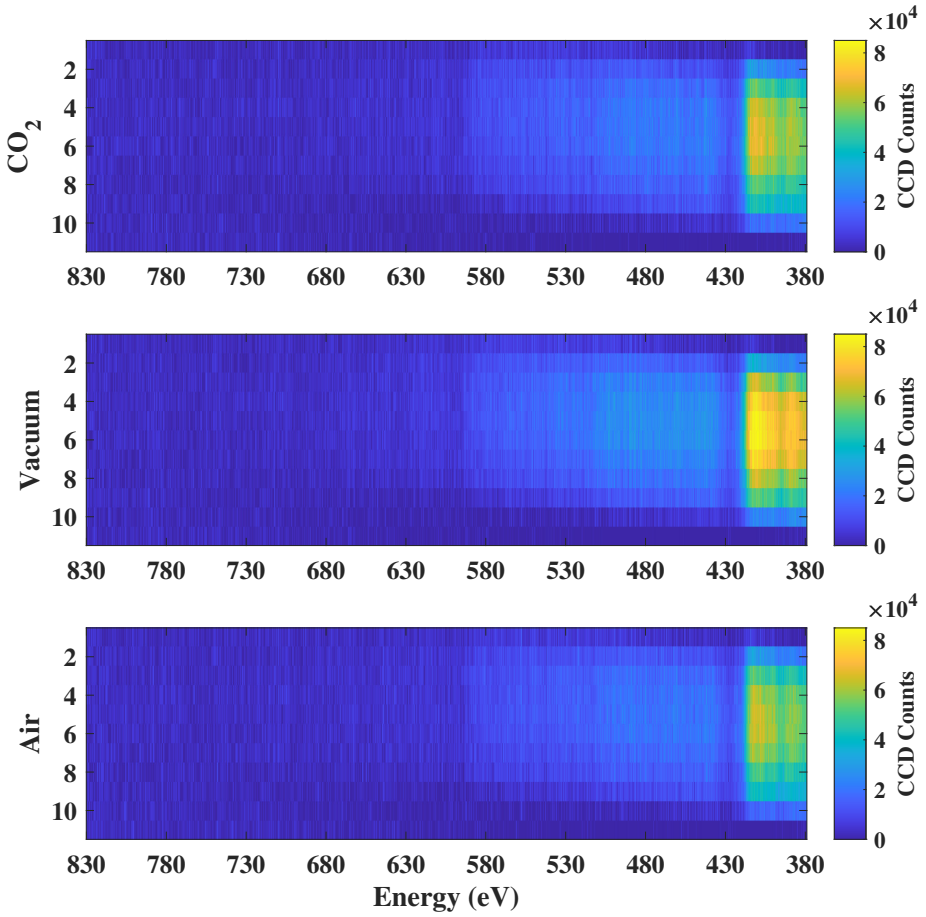

Figure B.2: Raw data of X-ray transmission through *in-situ* cell under CO_2 (top) vacuum (middle) and ambient air (bottom), measured for 50 minutes using a 100 µm slit and the X-ray emission from a Kr plasma.

B.3 Procedure for loading liquid cell

The liquid H_2O measurements presented here were performed using the *in-situ* cell in static operation (no liquid flow) so that the cell was loaded with water prior to installation in the vacuum chamber.

To start, the stainless steel frame was placed flat on a clean surface with the inner side facing up (similar to the orientation in Figure 3.2). One Si_3N_4 window was placed on top of the o-ring embedded in the cell so that the channel faced up and

pointed toward the two semicircles cut from the reservoir (again, see Figure 3.2). A ~10 µL drop of liquid was placed on top of the chip, which was then covered with the second Si_3N_4 window, with the channel facing down, and rotated to align with the channel of the bottom chip, pointing toward the two semicircles. Tweezers were used to ensure that the chips aligned and that the apertures of the windows were centered on the o-ring and the cell's aperture. The other half of the stainless steel cell body, with the o-ring attached, was placed on top, taking care not to shift the chips' position. The two holes in the tubing of the back half of the cell body were aligned with the semicircles of the front half. The four corner screws were tightened evenly to attach the two halves of the cell body. With the cap to one of the tubes open, a push pipette was used to push liquid into the other tube and through the cell until liquid emerged from the other tube. The cap was placed at that end of the tube, the pipette was removed, and the remaining tube was capped as well. Finally, the assembly was loaded into the vacuum chamber.

B.4 Water window soft X-ray transmission of in-vacuum liquid cell

When measured in vacuum, at $\sim 10^{-6}$ Torr, significant bulging is observed by the Si_3N_4 windows of the *in-situ* cell. X-ray emission is strongest on the edges of the Si_3N_4 windows, where the path length is smaller. Due to the large pressure difference between the cell and the surrounding vacuum, bulging is observed such that the middle of the windows show little to no transmission, as demonstrated in Figure B.3. The lack of transmission in the middle of the cell suggests that the bulging results in an increased depth of the water channel to >10 µm [59].

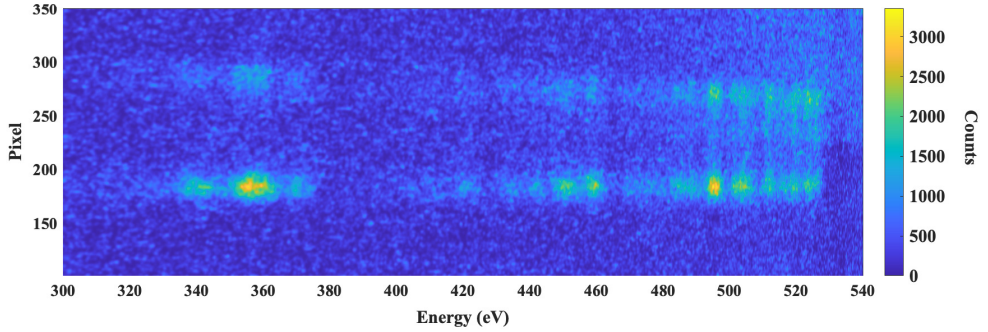

Figure B.3: X-ray transmission through the *in-situ* cell filled with distilled water, and mounted in a vacuum chamber held at $\sim 10^{-6}$ Torr. This image was captured by integrating for 8.3 minutes with X-ray emission from an Ar plasma to reduce the effects of stray light and scattered 1064 nm light from the laser. The 2D map was smoothed with a Gaussian filtering method with σ = 1.2.

To capture the complete transmission of the X-rays in the water window, SXR emission from a Kr plasma was used to measure liquid water in the *in-situ* cell, as shown in Figure B.4. Less bulging is observed; however, significant visible scatter from the Kr plasma could have prevented a more detailed image.

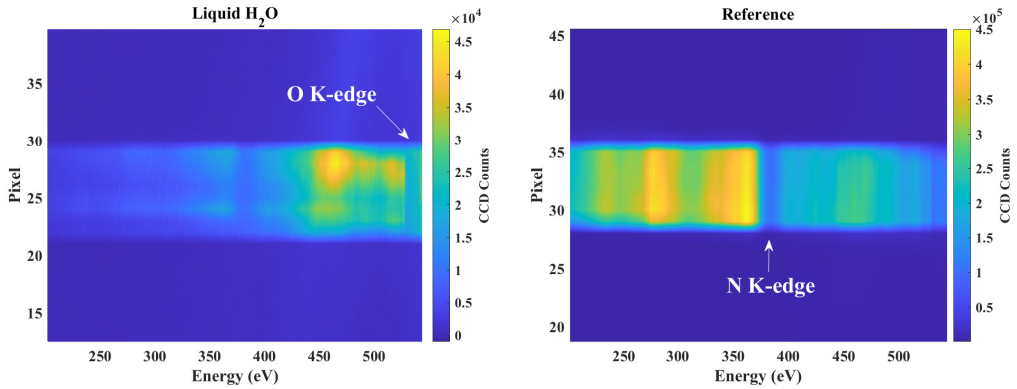

Figure B.4: Comparison of raw data from X-ray transmission through the *in-situ* cell filled with distilled water and that under vacuum. These images were captured by integrating for 50 minutes with X-ray emission from an Kr plasma, and not using a slit after the plasma. The brighter and larger Kr plasma results in significantly more visible scatter that makes it to the CCD. In these images, a mask was applied to reduce the effects of this scatter in the region that should be blocked by the *in-situ* cell, however visible scatter transmitted through the Si_3N_4 windows and liquid water likely affected the measurement of the O K-edge.

B.5 Development of an inline gas-phase cell

In addition to the micron scale *in-situ* cell presented above, a longer path-length inline cell was also developed for gas-phase transmission experiments. This cell is constructed using three stainless steel conflat flanges integrated directly into the vacuum chamber. It features input and output fittings, enabling operation in static mode or with continuous gas flow.

To facilitate evacuation during chamber pump-down and to acquire reference measurements, the cell is equipped with a bypass valve. This valve connects the interior of the cell to the main chamber, allowing the cell to be evacuated or held under vacuum for reference. The bypass valve is closed when gas is introduced, isolating the cell for measurements. In addition, the design supports air-sensitive sample analysis, as the cell can be assembled and sealed within a glovebox.

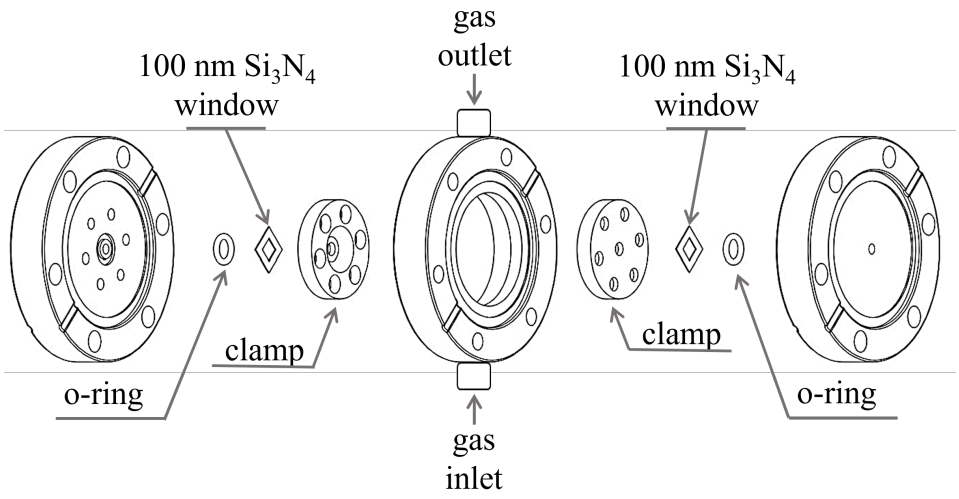

Figure B.5: In-line gas-phase *in-situ* cell for transmission soft X-ray (SXR) measurements. The cell consists of three 2.75-inch diameter conflat flanges (DN35CF) integrated into the vacuum chamber and beamline for transmission experiments. Both entrance and exit windows use custom clamps to compress Si_3N_4 membranes against CF flanges with o-rings, creating a vacuum-tight seal. Each flange has a 2 mm aperture, and the total path-length between the Si_3N_4 membranes is 2 cm.

Appendix C

SUPPLEMENTARY INFORMATION FOR TRANSIENT SOFT X-RAY ABSORPTION MEASUREMENTS OF TiO WITH A NANOSECOND LASER-PRODUCED PLASMA SOURCE

C.1 Temporal and Spatial overlap for the time-resolved SXR spectrometer

Temporal overlap was determined using a photodiode at the sample position and generating a plasma in ambient air. The timing of the pump pulse was then varied so that the photodiode traces between the pump pulse and the visible light emitted by the plasma (serving as the probe) could be captured to estimate time zero.

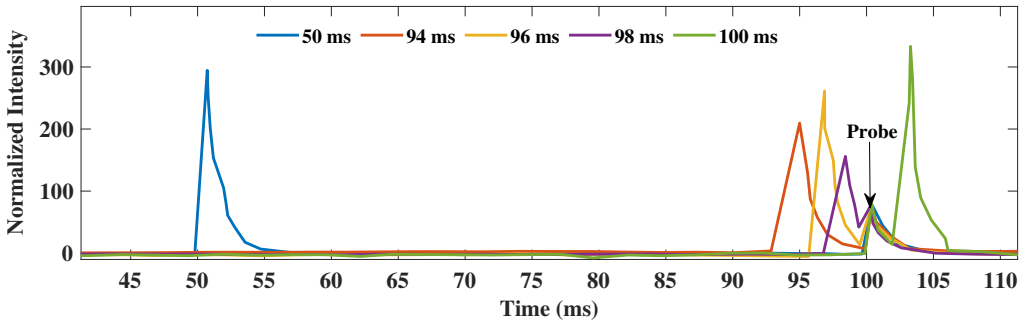

Figure C.1: Traces of the signal from the photodiode, placed at the sample position, to determine the relative temporal positioning of the SXR probe with respect to the UV pump, electronically triggered at various time delays.

Spatial overlap between the UV-pump and SXR-probe beam was achieved by determining the position and FWHM of the SXR probe using knife-edge scans.

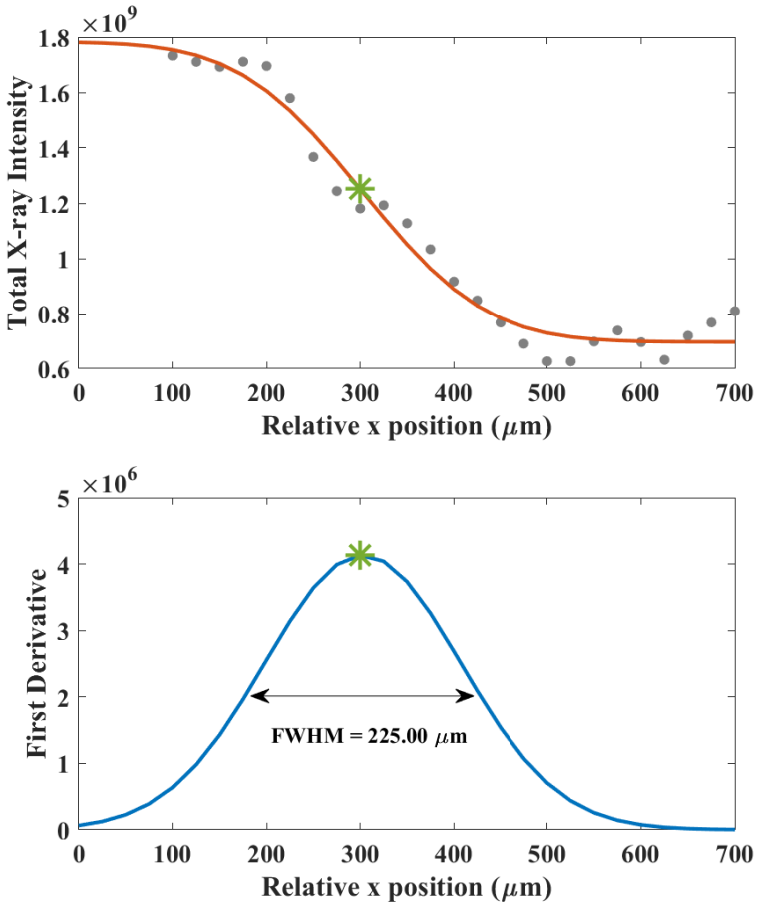

Figure C.2: Spatial positioning of the X-ray beam was determined by moving a knife edge horizontally into the beam path and measuring the decrease in flux as a function of position. The integrated intensity of X-ray spectra from an Ar plasma is shown in the gray scatter points, and was smoothed using LOWESS smoothing span 0.2. These data were fit to a complementary error function (red line) and the center of the X-ray beam was determined by setting the second derivative of this function to zero (green star). The first derivative of the error function is the spatial intensity of the SXR beam, plotted in blue. Full-width half-max of the X-ray beam was measured to be 225 μm.

C.2 Comparison of X-ray gratings with higher line density

The concave X-ray grating used in this work was compared with a concave grating with higher line density with the same focal length using the emission spectrum of N_2. Emission lines measured with the lower line density grating exhibited a broad spectral base that decreased the spectrometer's resolving power. For the two spectra given in Figure C.3, the lower line density grating gave a E/ΔE = 299, while that of the higher line density grating was 424, measured at λ = 2.878 nm (430.8 eV).

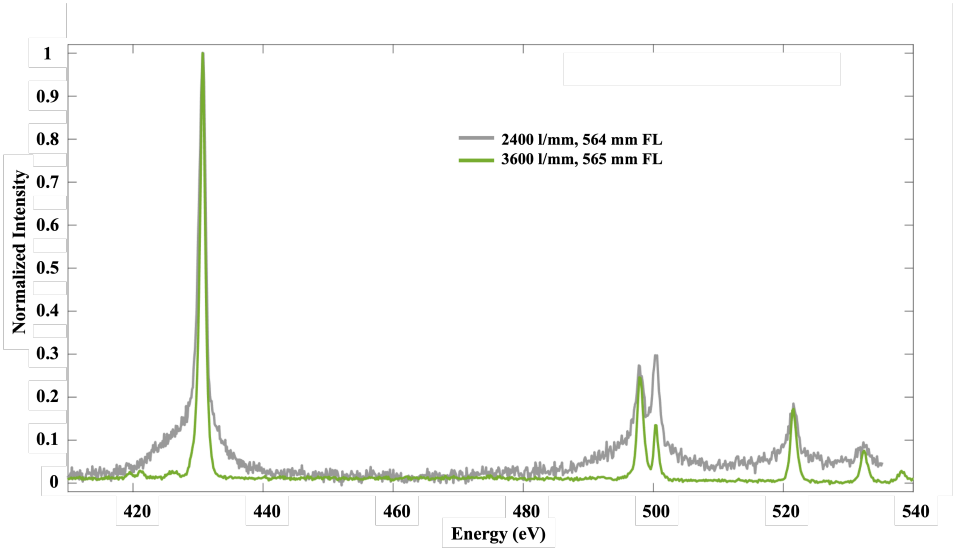

Figure C.3: Normalized N_2 emission spectra comparing aberration-corrected concave X-ray gratings with 3600 l/mm (Shimadzu PN L3600-1-6) and 2400 l/mm (Hitachi PN 001-0659) using a 50 µm slit. The N_2 emission spectrum taken with the 2400 l/mm grating was conducted using the ns pulsed laser and an in-vacuum electron multiplying CCD (Raptor photonics III-XV, 10 × 10 µm pixel size, 1024 × 1024 pixels). The spectrum taken with the 3600 l/mm grating was conducted using the ps pulsed laser and the same CCD used in Chapter 2 (Greateyes, GE 2048 512 BI UV1, 13.5 × 13.5 µm pixel size, 512 × 2048 pixels).